LBL-37438
UC-404

Lawrence Berkeley Laboratory
UNIVERSITY OF CALIFORNIA

Materials Sciences Division

Quasiparticle Energy Studies of Bulk Semiconductors, Surfaces and Nanotubes

X.F. Blase
(Ph.D. Thesis)

December 1994

Prepared for the U.S. Department of Energy under Contract Number DE-AC03-76SF00098

LBL-37438
UC-404

Quasiparticle Energy Studies of Bulk Semiconductors, Surfaces and Nanotubes

Xavier François Blase
Ph.D. Thesis

Department of Physics
University of California, Berkeley

and

Materials Sciences Division
Lawrence Berkeley Laboratory
University of California
Berkeley, CA 94720

December 1994

This work was supported in part by the Director, Office of Energy Research, Office of Basic Energy Sciences, Materials Sciences Division, of the U.S. Department of Energy under Contract No. DE-AC03-76SF00098, and by National Science Foundation Grant No. DMR-9120269.

LBL-37438
UC 404

Quasiparticle Energy Studies of Bulk Semiconductors, Surfaces and Nanotubes

by

Xavier François Blase

DEA (Ecole Normale Supérieure de Lyon et Université Claude Bernard, France)
1989

A dissertation submitted in partial satisfaction of the

requirements for the degree of

Doctor of Philosophy

in

Physics

in the

GRADUATE DIVISION

of the

UNIVERSITY of CALIFORNIA at BERKELEY

Committee in Charge:

Professor Steven G. Louie, Chair
Professor Peter Y. Yu
Professor Eugene E. Haller

1994

Abstract

Quasiparticle Energy Studies of Bulk Semiconductors, Surfaces and Nanotubes.

by

Xavier François Blase

Doctor of Philosophy in Physics

University of California at Berkeley

Professor Steven G. Louie, Chair

This dissertation focuses on the understanding of many-electron effects in bulk, surface, layered or nanostructure (e.g. nanotubes) semiconductors. The influence of many-body effects on the electronic excitation energies (quasiparticle band structure) of these materials is explored. The GW approximation, including local field effects, for the self-energy operator is used throughout this work to calculate quasiparticle energies. Specific studies include:

- A study of the newly discovered carbon nanotubes is carried out. Structural stability and band structures are calculated. A similar study is performed for boron-nitride (BN) nanotubes, leading to the prediction of their stability. For both systems, unexpected electronic features with important technological potentials are predicted. The filling of carbon nanotubes with metal atoms and the doping of BN nanotubes by carbon and other impurities is also studied.

- A study of the occupied surface states at the H/Si(111)-(1×1) surface is performed. We show that a quantitative understanding of the electronic structure requires a full quasiparticle calculation even for this simple chemisorption system.

- The core level shift of the Si $2p$ levels for atoms near the H/Si(111)-(1×1) surface is calculated. We show that a simple first order perturbation theory using pseudopotential and the local density approximation gives good results for the observed features in the photoemission spectra of the core electrons.

- A study of the quasiparticle energies of bulk hexagonal BN and those of an isolated BN sheet is done. The results provide a physical understanding of the quasiparticle band structure of BN nanotubes. A nearly-free electron state with a wavefunction in the inter-layer or vacuum region is shown to compose the bottom of the conduction bands.

- A novel mixed-space formalism for the calculation of the dynamical screening effects and electron self-energy operator in solids is presented. This approach provides an efficient algorithm to calculate quasiparticle energies for large systems.

A Valérie,

Contents

List of Figures

List of Tables

Acknowledgements

I would like first to express my sincere gratitude to my advisor, Professor Steven G. Louie, for his constant guidance, patience and support during all these years spent in Berkeley.

It is a pleasure to acknowledge the role of Professors Marvin L. Cohen, Y.R. Shen and Alex Zettl in Berkeley, Paul Dumas in Orsay, and Yves Petroff in Grenoble, as collaborators and mentors in some of the projects reported in this thesis. I am grateful to Professors Eugene Haller and Peter Y. Yu for their critical reading of this manuscript. Special thanks to my friends and collaborators in Berkeley: Angel Rubio, Yoshiyuki Miyamoto, Lorin Benedict, Antonio da Silva, Xuejun Zhu and Eric Shirley. Best memories and wishes to all members of the Condensed Matter Theory group.

I am indebted to Professors Guy Aubert and Gérard Martinez who, some few years ago, suggested to me that Berkeley could be a "good" place to live and study: they were right!

This work was supported by National Science Foundation Grant No. DMR-9120269 and by the Director, Office of Energy Research, Office of Basic Energy Sciences, Materials Sciences Division of the U. S. Department of Energy under Contract No. DE-AC03-76SF00098.

Chapter 1

Introduction and Overview

This dissertation is on the study of the structural and electronic properties of real materials using first-principles quantum mechanical methods. Two approaches are employed extensively: the density functional theory (DFT) [1] for ground-state properties and the quasiparticle self-energy approach [2] within the GW approximation [3] for electronic excitation properties. Calculations have been carried out to explain and predict the properties of several systems of significant current interest, including the newly discovered carbon and B-C-N composite nanotubes, semiconductor surfaces and layered materials, and wide band gap II-VI compounds. A novel approach for quasiparticle energy calculations is also developed.

In the past decade, considerable progress has been made in calculating the structural and electronic properties of materials within the local density approximation (LDA) [1] to DFT. More efficient nonlocal [4] and ultrasoft pseudopotentials [5] reduce considerably the effort of computations. New algorithms to iteratively diagonalize the Hamiltonian matrix [6] or to find directly the eigenvalues by efficient minimization techniques [7] have been developed and implemented, and systems with several hundreds of atoms can now be studied. Very recently, several N-linear methods have also been proposed [8, 9, 10, 11] in which the computing time scales linearly in the number of atoms N in the unit cell in the large N limit. Such improvements in the efficiency of state-of-the-art LDA calculations have allowed tremendous progress in the understanding of the ground-state properties of an ever expanding range of materials. The predictive power of *ab initio* calculations have been enhanced to such an extent that DFT-LDA are now being used in attempts to "design" new materials [12]. We present in Chapter 2 a study within LDA of the novel carbon and boron-nitride nanotubes. The metastability of carbon nanotubes is confirmed by our theory [13] and the existence of BN nanotubes is predicted [14]. In addition, unusual and possibly technologically important electronic features are shown to arise in these structures. In the case of carbon nanotubes, hybridization of the $\sigma^\star$ and $\pi^\star$ states of graphene is shown to be as important as band folding effects in determining the metallicity of small radius carbon nanotubes. For the BN nanotubes, we predict the lowest conduction state to be free-electron like with charge density localized inside the tube, leading to a remarkable constancy of the band gap independent of the tube size and helicity. Further, substitutional doping of BN nanotubes by carbon is studied. We show that carbon impurities substituting B atoms yield too deep a donor level to populate efficiently the bottom of the nanotubes conduction bands. Finally, we study the filling of carbon nanotubes by metallic atoms. We show that, for small radius nanotubes, microscopic processes such as interatomic charge transfer are responsible for the "intercalation within" of carbon nanotubes by metallic atoms.

Although ground-state properties such as structure, binding energies, and vibrational properties can be obtained within DFT, those associated with exciting electronically the system into a higher energy state are beyond the scope of a ground-state theory. As a consequence, the Kohn-Sham eigenvalues, used within DFT to determine the ground-state total energy of real-materials, are well-known to yield large errors when compared to experiment for fundamental quantities such as band gap, interface- and surface-state energies, or semiconductor band offsets. These problems are related to the approximate use of the Kohn-Sham eigenvalues for quasiparticle energies. In particular, they do not invalidate the band structure picture of solids, which have proven to be a very convenient and successful framework for understanding electronic excitations. This is exemplified in this thesis where we show that the photoemission spectra of real materials can be explained quantitatively and even predicted, provided that they are properly interpreted as transitions between quasiparticle states of the many-electron systems. These quasiparticles, which are the particle-like excitations of an interacting many-electron system, provide a bridge between a rigorous many-body theory and the very "practical" band structure picture. We note, however, that such an approach relies on the presence of "well resolved" peaks in the experimental spectra used to characterize the electronic states of the system of interest. Because a quasiparticle is defined and experimentally observed as a peak in the spectral density of the interacting system, it is of course required that these spectral peaks be well defined and do not overlap to form a featureless background. Equivalently, the lifetime of these particle-like excitations must be larger than the mean interaction time of the experimental probe with the crystal. This condition insures the "functionality" of the quasiparticle approach.

For a detailed exposition on the concept of quasiparticle, we list in the bibliography references for the Fermi liquid theory [15] which lays the formal framework for the present approach. In brief, the "many-body" approach incorporates the fact that bare electrons in solids are strongly interacting with each other via the Coulomb potential V_C. To deal with the complexity of the many-body problem, we assume, as a starting point, that the non-interacting electrons evolve "continuously" (when the Coulomb interaction is adiabatically switched on) into "identifiable" quasi-particles. By continuously, we mean that in the process of switching on the interaction, no phase transition occurs which radically changes the structure of the energy spectrum so that the one-to-one correspondence between the electrons and the quasiparticles is not broken (important counter-examples are the Wigner crystallization at low electronic density and the superconducting transition). These quasiparticles can then be roughly described as electrons surrounded by a polarization cloud or exchange-correlation hole. Therefore, the interaction of an electron with its surrounding can be recast as a self-energy for the quasiparticle.

To obtain now an expression for the self-energy operator, one notes that the screened interaction W in a solid is in general much weaker than the bare Coulomb potential. Consequently, an expansion of the self-energy operator in terms of W converges rapidly. Taking the first term of this expansion yields the so-called GW approximation [3] for the self-energy operator (with G being the electron propagator). It is this approximation which is used throughout this thesis. Further, following the pioneering work by Hybersten and Louie [2] who provided for the first time a practical method to calculate *ab initio* the quasiparticle energies of real materials in the GW approximation, this approach has been shown to yield for semiconductors bulk [2, 16, 17], surface [18, 19, 20, 21], interface [22] and superlattice [23] quasiparticle energies accurate to within 0.1 eV when compared to various spectroscopic experiments. The method has also recently been successfully applied to complex materials such as solid C_{60} [24].

As part of this thesis, we study using the self-energy approach [2] several materials of important theoretical and technological interests. We focus specifically on systems in which the structural and electronic properties depend on the interplay of physically very different electronic states. For example, the study of a surface system requires that the theoretical approach employed be able to treat with the same accuracy both extended bulk states and localized surface states. We present also the example of layered materials where layer states and inter-layer states coexist. Finally, II-VI compounds are materials in which the interaction of the core-like $3d$ states with the covalent s and p levels has a crucial influence on both the structural and electronic properties.

In Chapter 3, we present a study of the surface states of the H/Si(111)-(1×1) surface [25]. Because of both its simplicity and the availability of recent state-of-the-art high-resolution angle-resolved photoemission data, this system is an ideal prototype for studying many-body effects at a semiconductor surface. Comparison of the quasiparticle surface-state energies with those from LDA eigenvalues shows that the self-energy corrections are very large, typically two to three times larger than the corrections found in previous calculations on other semiconductor surface systems. For some of the surface states, their energy locations are extracted by the self-energy operator from the bulk continuum where they were incorrectly located within LDA. In addition, the calculated dispersion of theses surface states (which is found to be too large by ~ 1 eV within LDA) is brought to perfect agreement with experiment.

In Chapter 5, we study the quasiparticle band-structure of bulk hexagonal BN as well as that of an isolated BN sheet [26]. These systems are technologically important since bulk BN is an extremely hard material and possesses the widest band gap of all the III-V compounds. Also, theoretical calculations on an isolated BN sheet are used to provide informations for the analysis of the properties of the BN nanotubes. The self-energy correction opens the LDA band gap of hexagonal BN by as much as 1.7 eV. In the case of the isolated BN sheet, LDA and GW in fact do not yield the same conduction band ordering, leading to a different identification of the states which determine the band gap. This is related to an exceptionally large k-dependency of the self-energy of the various electronic states in this particular system. The importance of an interlayer state in determining the gap of bulk hexagonal BN is demonstrated. A corresponding "sheet" state, in the case of the isolated BN sheet, plays the same role in determining its band gap.

Although the reliability of the present self-energy approach to describe quasiparticle energies has been clearly demonstrated for *s*-*p* bonded materials, calculations within this formalism have been restricted to the study of systems with less than 100 atoms. The primary reason is that calculations with the self-energy approach require a significant increased complexity in the formalism as compared to DFT-LDA calculations. In particular, because dynamical and local-fields effects are crucial for accurately describing the screening in real materials [2], they are both taken into account in the present quasiparticle formalism. Therefore, the self-energy operator is non-local, energy-dependent and in general non-Hermitian. Its calculation is computationally much more demanding than simply solving the local and time-independent Kohn-Sham equation within LDA.

To improve on this situation, we propose in Chapter 6 a novel mixed-space formalism for the quasiparticle energy calculations within the GW approximation. This new approach is shown to be computationally more efficient than the existing reciprocal-space formalism [2], in particular for calculations on large size supercells, or supercells in which the vacuum region constitutes a large part of the unit-cell (molecules, clusters, surfaces, etc) or systems which exhibit significant electronic charge density inhomogeneities (transition metals, II-VI compounds, etc). Results for bulk Si and the H/Si(111)-(1×1) surface are presented. In addition, going beyond the generalized plasmon pole model generally used in previous quasiparticle calculations, we implement an explicit calculation of the frequency dependence of the dielectric matrix. This effort is motivated in part by our attempt to calculate the quasiparticle energies of the $3d$ levels in cubic ZnS. We show in this case (see Appendix A) that the use of the generalized plasmon pole model for the extension to finite frequencies of the static dielectric matrix may not be adequate. We note here that most of the equations on which the quasiparticle GW formalism is based will be presented in Chapter 6 (besides an introduction in section 3.2.2). Readers who are not familiar with the self-energy approach may want to read this chapter first.

To close this introductory chapter, we would like to note that sometimes it is not necessary to carry out heavy computational calculations to get "trends" and understanding of the behavior of materials and that under appropriate conditions simple model Hamiltonians can reproduce fairly well many properties of materials while providing, at the same time, a very simple picture of the basic driving mechanisms for the properties of interest. For example, in Chapter 4, a simple first-order perturbation theory gives excellent results for the the Si $2p$ core level shift at the H/Si(111)-(1x1) surface [27]. As another example, we show in Appendix A that a simple Hubbard Hamiltonian, based on parameters derived from *ab ini-*

tio total energy calculations, yields excellent results for the binding energies of the two-phonon bound states at the H/C(111)-(1×1) surface [28]. We note however that semi-empirical methods may sometimes fail ttoo describe new materials or new situations because the transferability of the parameters used in such approaches is never certain. This is exemplified in Chapter 2 where it is shown that tight-binding (TB) approaches, with parameters designed to reproduce the electronic properties of bulk hexagonal graphite and BN, fail to describe the novel electronic properties of nanotubes induced by the curvature and nanoscale size of these structures. Another example is given in Chapter 5 where a nearly-free-electron state is discovered which cannot be described by the usual localized basis sets used in TB. Of course (and this is a motivation for this work) the lack of transferability of a theoretical model (such as the uniform electron gas model for LDA) limits also the predictive abilities of *ab inito* methods. There is the usual temptation to try to overcome the problem by adding additional layers of complexity to the existing theories. It is definitely a very difficult task to maintain both a balance and a bridge between the more and more complex theories and the simple models, so that the physical understanding of the properties of real materials may benefit from both types of approaches.

Chapter 2

Structural and electronic properties of nanotubes

2.1 Introduction

Since the discovery of graphitic nanotubes [29] created in an arc discharge between two carbon rods, much experimental and theoretical efforts have focused on the synthesis and understanding of these novel quasi one-dimensional structures. Using iron [30] or cobalt [31] based catalysts, single- or multi-wall carbon nanotubes can be selectively synthesized. Tubes with diameter as small as 7 $\AA$ have been observed [30]. Carbon nanotubes, which are found capped after synthesis, can also be opened and filled with atoms, molecules or small clusters [32]. Further, based on similarities between carbon and BN-based materials, BN nanotubes have been investigated [14]. By heating of amorphous BN to 1100^{o}C, large turbostratic tubular BN structures have been obtained [33]. Recently, $B_xC_yN_z$ nanotubes have been observed [34] using composite carbon/BN anode rods under arc discharge. A quantitative determination of the chemical composition of these nanotubes suggests the presence of BC_3 and BC_2N nanotubes. The existence of these tubes have been previously predicted by theoretical calculations [35, 36].

In this chapter, we present a theoretical study of the structural and electronic properties of carbon and BN nanotubes. An *ab initio* pseudopotential approach is used in the framework of the local density approximation (LDA). In section 2.2, small single-wall carbon nanotubes are discussed. We show that carbon nanotubes, with diameter down to 5.5 $\AA$, are metastable. In particular, contrary to what have been recently suggested, their strain energy is not large enough that they would open into carbon strips. Further, the metallicity of these tubes is studied as a function of their size and chirality. In previous calculations [37, 38], classification of the carbon nanotubes as metals or semiconductors was determined on the basis of how the underlying graphite band structure is "folded" when one applies the tubes' azimuthal periodic boundary conditions. Although early work [37, 38, 39] has noted that hybridization of the graphitic σ,π,$\pi^\star$ and $\sigma^\star$ states should occur because of the curvature of the tubes, the importance of these effects was not fully appreciated. The tube states near the Fermi level were described as chiefly π and $\pi^\star$ states. Recently [30], nanotubes with very small radii were experimentally produced, with diameters as small as 7 $\AA$. We show here that sufficiently strong hybridization effects occur in such tubes which dramatically change the band structure proposed in these previous works.

In section 2.3, we present extensive LDA and quasiparticle calculations performed on boron nitride (BN) single-wall and multi-wall nanotubes. Strain energies are found to be smaller for BN nanotubes than for carbon nanotubes of the same radius, owing to a buckling effect which stabilizes the BN tubular structure. For tubes larger than 9.5 $\AA$ in diameter, the lowest conduction band is predicted to be free electron-like with electronic charge density localized inside the tube. For these tubes, this band is at constant energy above the valence band maximum. Consequently, in contrast to carbon nanotubes, single and multi-wall BN nanotubes have constant band gap, independent of their radius and helicity.

In section 2.4, we study the doping of bulk hexagonal BN by substitution of a boron atom by a carbon atom. We show that the carbon impurity yields a deep donor level located 0.5 eV below the bottom of the conduction band which is free electron-like. Finally, the metallic filling of carbon nanotubes is investigated in section 2.5.

2.2 Hybridization effects and metallicity in carbon nanotubes

We have carried out both *ab initio* pseudopotential local density functional

(LDA) calculations and Slater-Koster [40] tight-binding (TB) calculations. Following the notation of Ref. [38], we study the tubes (n,0), with n ranging from 6 to 9. As illustrated in Fig. 2.1(a), tube (n,0) corresponds to wrapping a section of a graphitic sheet in the indicated orientation with n hexagons around the tube circumference. The diameter of these tubes ranges from 4.78 $\AA$ for (6,0) to 7.20 $\AA$ for (9,0). The LDA electronic structure calculations were performed using a planewave basis set. We generated first a semilocal pseudopotential following the scheme of Troullier and Martins [41] and made it fully nonlocal according to the Kleinman and Bylander procedure [4]. The energy cut-off for the electronic wave-functions was set at $E_{cut}=$ 49 Ry leading to an 0.05 eV convergence of the band energies. The very large number of planewaves needed for this type of calculation (ranging from 13,500 for (6,0) to 19,000 for (9,0)) required the use of an efficient iterative diagonalization scheme [42]. The LDA calculations were carried out in a supercell geometry with a hexagonal array of tubes, with the closest distance between atoms on different tubes being 5.5 $\AA$. This permitted the neglect of tube-tube interactions. For the TB calculations, we used the first and second nearest neighbor parameters proposed in Ref. [43] for graphite.

Along the axes of the tubes, the length of the unit cell was set by assuming that the tube was generated simply by rolling a graphite sheet segment [37]. Using the Hellman-Feynman theorem, we found that the stresses imposed on each supercell were negligible in the axis direction. The most important structural change was the tendency of the tube to reduce its radius from that given by the above rolling. This effect was nonetheless small, ranging from 1.6 % reduction for (6,0) to nearly zero for (9,0). We found similar results within a tight-binding total energy minimization scheme [44]. The effect of this relaxation on the electronic band structure was negligible. We also relaxed the internal coordinates of the atoms using Hellman-Feynman forces. The forces were very small, and all the atoms remained equivalent within the unit cell.

Our results for the band gaps are given in Table 2.1, compared with those from previous TB work [37]. We find major differences between the results from LDA and the TB calculations. The most significant difference occurs for the tube (6,0) which has been previously predicted to be a small gap semiconductor [37]. We find in this work that, within LDA, tube (6,0) is a metal. In addition, we find that tubes (7,0) and (8,0) are semiconductors, consistent with previous calculations, but with a much smaller gap than those from TB based works. This discrepancy is mainly due to a singly degenerate state which is much lower in our LDA calculations than in the TB work. LDA is known to underestimate the value of the band gap of many materials, but the narrowing of the gap here is due primarily to curvature effects, as evidenced by the dependence on tube size.

In Fig. 2.2 we show the band structure and density of states (DOS) for the tube (6,0). The singly degenerate state mentioned above is labeled by (a). At Γ, this state is 0.83 eV below the doubly degenerate state that forms the top of the valence band in TB calculations. This band overlap makes the tube (6,0) a metal within LDA with a density of states at the Fermi level equal to $D(E_F) = 0.07$ states/eV-atom. For this tube, we also performed an independent LDA calculation using a semilocal pseudopotential and another diagonalization scheme as described in Ref. [24]. The two LDA band structures were in excellent agreement. We also checked that this state is insensitive to the small structural relaxation effects described above.

As we shall show, state (a) occurs in all (n,0) tubes for symmetry reasons, but its energy at Γ varies with n. For the tubes (7,0) and (8,0), state (a) does not close the gap but reduces significantly its value as compared to TB calculations. For these two tubes, the state (a) at Γ lies between the two doubly degenerate states that form the top of the valence and bottom of the conduction bands in TB calculations. This state reduces the TB gap by 1 eV for (7,0) and by 0.6 eV for (8,0). For the tube (9,0), the state (a) lies just above the TB LUMO state and therefore does not fall within the gap.

The discrepancy between TB and LDA calculations decreases as the radius of the tube increases. This is consistent with the notion that, in large tubes with small curvatures, one obtains a good description of the nanotube band structure by "folding" the graphite sheet band structure. However, this idea implicitly relies on the assumption that states around the gap or Fermi level are essentially π or $\pi^\star$ derived [38, 39]. This is not true for small tubes where the curvature is so strong that large hybridization effects occur. We show in Fig. 2.3 the charge density distribution for the state (a) at Γ for the tube (6,0). One can see that most of the wave-function is localized outside the tube. If this state is mostly π or $\pi^\star$ derived, it should have equal weight inside and outside the tube. Detailed analysis of the $\sigma^\star$-$\pi^\star$ hybridization in (n,0) tubes also indicates that this state should be mostly outside of the tubes for k-vectors near the tube's zone center. We show below that it is crucial to accurately describe the $\sigma^\star$ states and their interaction with the $\pi^\star$ complex before one is able to reproduce within TB the behavior of the state (a) in our LDA calculation.

To study the effects of hybridization on the state (a) of tube (6,0), we begin with a planar sheet of graphite with the unit cell described in Fig. 2.1(a). Because state (a) is singly degenerate, in the "band folding" language, it must be derived from the Γ-M line of the graphite sheet Brillouin zone (BZ), and must occur in all (n,0) tubes. As a result of the boundary conditions of the tube, M is folded onto Γ. We plot in Fig. 4(a) the corresponding TB bands along the Γ-X direction of the tube (see Ref. [37]). From the symmetry of the tube, singly degenerate states only mix with each other and not with states of higher degeneracy, so only these need be considered in the analysis of the behavior of state (a). The dashed lines are the singly degenerate bands coming from the folding of the $\pi^\star$ and $\sigma^\star$ graphite bands along the Γ-M line of the hexagonal graphite BZ (Fig. 2.1(b)) onto the Γ-X line of the tube BZ. Next we bend this graphite sheet along the AB direction while imposing the proper periodic boundary conditions in order to mimic a continuous transformation of the graphite sheet onto the (6,0) tube. This procedure distinguishes the zone folding effects from the curvature effects.

Fig. 2.4 illustrates the evolution of our TB band structure under this transformation for two of these "intermediate" structures. Their radii of curvature are between $R = \infty$ of planar graphite (Fig. 2.4(a)) and R =2.39 $\AA$ of tube (6,0) (Fig. 2.4(d)). For a curved sheet of graphite, the $\pi^\star$ and $\sigma^\star$ states mix and repel each other, resulting in a lowering in energy of the (originally) purely $\pi^\star$ states. It is the lower hybridized $\pi^\star$ band which gives rise to the singly degenerate state (a) near E_F in the LDA calculation. Therefore, within the TB Hamiltonian of Ref. [43], this state does exist, but it is not low enough in energy to make the tube metallic as found in the LDA calculation. We note also that, with a localized basis set limited to 2s and 2p orbitals, TB calculations are unable to describe large charge transfer asymmetrically away from the atoms. However, in our LDA calculations, we find the total potential to be locally symmetric inside and outside the tube so that the localization of the state (a) outside the tube must be mainly due to hybridization and not electrostatic effects. Similar studies have been made for tubes (7,0), (8,0), and (9,0), yielding similar results.

Some workers [45, 46] have recently suggested that tubes with radii smaller than $\sim$3 $\AA$ will not be stable. They argue that, for such tubes, the elastic strain energy per atom stored in the rolled sheet is larger than the dangling bond energy per atom for the flat graphitic strip obtained by "cutting" the tube along its cylindrical axis. In order to address this question for the tubes of our study, we carry out LDA total energy calculations for the (6,0) tube with radius 2.39 $\AA$ and the corresponding strip. We find that the tube is energetically more stable than the strip. This implies that the critical radius below which tube energy exceeds strip energy for the (n,0) tubes is less than the (6,0) tube radius. This result is in agreement with a force-field calculation [46] which predicts the critical radius to be $\sim$ 2 $\AA$, in contradiction with the semi-empirical calculation of Ref. [45] which predicts the critical radius to be ~ 3.85 Å. However, we stress that as long as the tube and strip energies are comparable, kinetic effects will still dominate the growth process. Thus, total energy comparisons may not be relevant to the question of tube stability.

In conclusion, large $\pi^\star$-$\sigma^\star$ hybridization effects can occur in small nanotubes which drastically change the electronic band structure from that obtained by simply "folding" the graphite sheet band structure. These effects are demonstrated in our study of tubes (6,0) to (9,0), some of which are comparable in size to the smallest tube experimentally observed thus far. Our results show that, for this class of tubes, hybridization effects change the energy and character of the lowest lying conduction band states with important consequences to the metallicity and transport properties of the tubes. An implication of this result is that hybridization effects could also play an important role in doped small nanotubes with metallic dopants either inside or on the tubes.

2.3 Stability and band gap constancy of BN nanotubes

In a recent paper [47], the existence of boron nitride (BN) nanotubes was proposed. It was suggested that these tubes may be stable and their electronic properties were studied within an empirical Tight-Binding (TB) approach. However, because of the lack of a total energy calculation scheme within TB for BN based materials, no evidence for the stability of BN nanotubes was given and the calculations were restricted to tubes with the "ideal" geometry given by rolling a single sheet of hexagonal BN into a tubular shape. In addition, as shown in the previous section, the large curvature of small tubes may induce strong hybridization effects which strongly modify the band structure given by a standard s-p Slater-Koster TB scheme.

We have carried out *ab initio* pseudopotential local density functional (LDA) calculations to study from first-principles the structural stability of this novel form of BN. Further, we have studied the electronic properties of BN nanotubes, both within LDA and within the more accurate quasiparticle approach. The electronic properties of multi-wall BN tubes are also investigated. The calculation of the quasiparticle energies is performed using the self-energy approach [2], based on the GW approximation [3]. Technical details for the quasiparticle calculations will be described in Chapter 5. Pseudopotentials and electron wavefunctions are expanded in a planewave basis. The energy cut-off for the electronic wavefunctions is set at E_{cut}= 45 Ry to converge both total energies and eigenvalues. Boron and nitrogen pseudopotentials are generated following the Kleinman and Bylander procedure [4]. The calculations are carried out in a supercell geometry with a hexagonal array of tubes. The closest distance between atoms on neighboring tubes is set at 5 $\AA$. Within this geometry, tube-tube interactions are negligible.

By minimizing both stress and Hellman-Feynman forces, we determine first the equilibrium geometry for (n,0) and (n,n) tubes with diameters ranging from 4 to 12 $\AA$ (index notations for the tubes refer to the convention of Ref. [37, 38] as defined for graphitic nanotubes). The main relaxation effect is a buckling of the boron-nitrogen bond, together with a small contraction of the bond length ($\sim 1\%$). In the minimum energy structure, all the boron atoms are arranged in one cylinder and all the nitrogen atoms in a larger concentric one. We plot in Fig. 2.5 the structure of a BN (8,0) tube corresponding to the calculated buckling.

Due to charge transfer from boron to nitrogen, the buckled tubular structure forms a dipolar shell. The distance between the inner "B-cylinder" and the outer "N-cylinder" is, at constant radius, mostly independent of tube helicity and decreases from 0.2 a.u. for the (4,4) tube to 0.1 a.u. for the (8,8) tube. As a result of this buckling, each boron atom is basically located on the plane formed by its three neighboring nitrogen atoms so that the sp^2 environment for the boron atom in the planar hexagonal structure is restored (at most, the $\widehat{NBN}$ angles differ from 120^0 by 0.2% for the smallest tube). This tendency for three-fold coordinated column III atoms to seek 120^o bond angle is extremely strong. For example, it explains the atomic relaxation of the (110) and (111)-2x2 surfaces of GaAs and other III-V compounds [48]. On the other hand, the $\widehat{BNB}$ angles approach the value of the bond angle of the s^2p^3 geometry. This is also consistent with previous calculations performed on small $B_{12}N_{12}$ clusters [49] where a similar buckling of the BN bond was observed for a monocyclic ring structure. Buckling and bond length reduction induce a contraction of the tube along its axial direction by a maximum of 2% for the smallest tube studied.

Energies per atom for the relaxed tubes are plotted in Fig. 2.6 as a function of the tube diameter. The zero of energy is taken to be the energy per atom of an isolated hexagonal BN sheet. On the same graph, the energy per carbon atom above the graphite sheet energy is represented. As for graphitic tubes, BN tube energies follow the classical $1/R^2$ strain law, where R is the average radius of each tube. However, for the same radius, the calculated strain energy of BN nanotubes is smaller than the strain energy of graphitic tubes. This is related mostly to the buckling effect which reduces significantly the occupied band energy in the case of the BN compounds. Therefore, it is energetically more favorable to fold a hexagonal BN sheet onto a nanotube geometry than to form a carbon nanotube from a graphite sheet. Based on the existence of carbon nanotubes, we predict that BN nanotubes are metastable structures.

We also address the question of stability of a small tube versus opening into a strip of hexagonal BN [45]. We performed total energy calculations for the strip corresponding to the small tube (6,0), allowing complete relaxation of the strip geometry. As shown on Fig. 2.6 (filled square), the strip is less stable than the corresponding tube. As for carbon nanotubes, BN nanotubes with a radius larger than 4 $\AA$ are stable with respect to a strip.

Because of its large ionicity, a hexagonal BN sheet is a large gap semiconductor in contrast to graphite which is semimetallic. Consequently, on the basis of a band folding analysis [38, 37], BN nanotubes are large gap semiconductors, with direct gap at Γ for (n,0) tubes and indirect gap for (n,n) tubes. However, strong hybridization effects can occur because of curvature of the tubes which may strongly modify the band structure given by the band folding analysis. As for carbon nanotubes, the present *ab initio* LDA calculations show that for small (n,0) tubes, a $\pi^\star$-$\sigma^\star$ hybridized state significantly reduces the gap predicted by the band folding analysis. Consistent with its carbon analog, this state is at the zone-center **k**-point Γ with wavefunction localized outside the tube. It corresponds to the hexagonal BN $\pi^\star$ state at K which is folded onto the tube Γ point when rolling the BN sheet onto a (n,0) tube. Once folded, this state lowers its energy by interacting with the $\sigma^\star$ state at Γ. However, the consequences of the energy lowering of this state are less important than that in the case of carbon nanotubes since (n,0) BN tubes remain large gap semiconductors with a LDA minimum band gap of 2.5 eV for the (6,0) tube. With decreasing tube curvature, the hybridization effects are less important. For (n,0) tubes such that $n > 12$ (which corresponds to a diameter larger than 9.5 $\mathring{A}$), the hybrid state does not play any role in determining the gap of the BN tubes.

For (n,n) tubes, the key feature is the bottom of the conduction band at Γ. For all (n,n) tubes studied, this state is, within LDA, located at around 4 eV above the top of the valence band, independent of tube radius. In addition, this state is uniquely characterized by a remarkable charge density distribution. As shown in Fig. 2.7 for the (6,6) tube, this state yields a nearly constant charge density filling the interior of the tube. Since in this region the tube potential is constant, this state has a nearly-free-like electron (NFE) behavior. The effective mass at Γ for this NFE band is calculated to be $m^* = 1 \pm 0.1\ m_e$ for all tubes, where m_e is the free electron mass.

In a band folding analysis, this NFE state corresponds to the bottom of the conduction band at Γ for hexagonal BN. This is shown in Fig. 2.8 where we compare the LDA band structure for the BN (4,4) tube to the LDA hexagonal BN band structure. In this calculation, the distance between two BN planes is set to the (4,4) tube diameter. We select directions in the hexagonal Brillouin zone (BZ) which, in a band-folding analysis, would yield the tube top of the valence and bottom of the conduction bands. As one can see, the bottom of the conduction band is very similar in both structures, with hardly any modification in position and shape around the center of the zone. For hexagonal BN, the charge density of the state at the bottom of the conduction band is located on the nitrogen atoms and in the interplanar region. This state is the analog of a $\sigma^\star$ state at Γ in graphite [50] and has been referred to as the interlayer state.

Since the NFE tubule state at Γ is the image of the interlayer state in the band-folding mapping, it exists in all tubes independently of their helicity. We note that the NFE-state is very constant in energy and does not hybridize with curvature: this is because its wavefunction does not overlap with those of other states which are mostly localized on the tube wall. This explains that, even for the smaller tubes, the LDA band gap is stabilized at around 4 eV, except for the few (n,0) tubes with n $\leq$ 12. Even for these tubes, for which the $\pi^\star$-$\sigma^\star$ hybrid state forms the bottom of the conduction band, the NFE-state is, within LDA, localized at 4 eV above the top of the valence band. We have studied also the band structure of two concentric tubes (in the case of carbon, most graphitic "needles" are formed of concentric tubes). We select the (4,4) and (9,9) tubes. The difference between their radii is comparable to the Van der Waals equilibrium distance between two layers in bulk hexagonal BN. Tube-tube interaction hardly modifies the energy and wavefunction of the innermost tube NFE state, which remains the bottom of the conduction band at 4 eV above the top of the valence band. We predict therefore that for all BN tubes (except the (n,0) tubes with n $\leq$ 12) the band gap is stabilized around 4 eV (LDA value) and the bottom of the conduction band is a NFE-like state.

Since a band-folding analysis correctly describes the band structure of most BN tubes, we perform a more accurate description of the electronic properties of these tubes by studying within the quasiparticle formalism the electronic band structure of hexagonal boron-nitride compounds. This study is reported in details in Chapter 5 and we give here a "preview" of the results which are used to understand the properties of BN nanotubes. Several structures are studied which are composed of periodically repeated layers of hexagonal BN sheets, with an interlayer distance varying from d= 5.5 $\mathring{A}$ (diameter of the (4,4) tube) to d= 13.5 $\mathring{A}$. By including layer-layer interactions, we investigate the effects of the overlap of orbitals inside small tubes and of tube-tube interactions in multi-wall structures. For $d = 13.5\mathring{A}$, two neighboring layers do not interact. Therefore, the corresponding band structure can be used to obtain the band structure of large diameter BN tubes. For all these layered structures, the quasiparticle band gap is indirect between the top of the valence band at M and the bottom of the conduction band at Γ. The calculated band gap is very stable around 5.5 eV for all inter-layer distances d. This is in excellent agreement with the experimental value of 5.8 eV for bulk hexagonal boron-nitride [51]. Therefore, the quasiparticle calculation confirms the physical picture given by the LDA approach: single-wall and multi-wall BN nanotubes are nearly constant gap materials with a band gap around 5.5 eV (quasiparticle value). In addition, the lowest occupied state is a NFE-like state with charge density localized inside the tube.

As discussed above, for bulk BN, the interlayer state has a maximum and nearly uniform charge density in the vacuum region between BN layers. For $d = 13.5\mathring{A}$, the "interlayer state" does not overlap with the one of a neighboring layer. However, it remains localized in the vacuum region with a maximum charge density at ~ 2 $\mathring{A}$ away from the corresponding BN plane. Consequently, for very large tubes, we expect the charge density for the NFE-state at Γ to be localized in a region at about 2 $\mathring{A}$ away from the interior of the tube wall and to remain NFE-like. We remark that the interlayer state described here does not exist in a usual TB calculation based on a minimal ($3s$,$3p_x$,$3p_y$,$3p_z$) basis. Therefore, even in the limit of large nanotubes, for which hybridization effects are negligible, a simple TB picture would not describe correctly the nature of the BN tube gaps. This is contrary to the case of carbon nanotubes where TB and LDA results agree for large tubes. In the case of graphite, the interlayer state within LDA is 2 eV above the bottom of the conduction band so that this NFE state is at higher energy in the conduction bands and does not play any role in the metallicity and doping properties of the carbon nanotubes.

In conclusion, we find that the wrapping of the planar hexagonal structure onto a tube geometry is slightly more favorable for BN tubes than carbon nanotubes. This is mostly related to a buckling effect which stabilizes the BN tubular structure. The BN nanotubes are predicted to be wide gap semiconductors with a value of $\sim$ 5.5 eV, independently of their radius and helicity. This insensitivity of the BN tube band gap to variations in radius, helicity and coaxial arrangement, may be of crucial importance for technological applications because samples containing many different sizes and structures, single-wall or multi-walls tubes, could be grown with predictable electronic properties [52]. This constant gap value is related to the bottom of the conduction band state, which has a nearly-free-electron-like behavior with charge density localized inside the tube. We expect this property to have important technological implications particularly in the case of n-type doping (we study in the next section the possibility of doping BN nanotubes by substitution of an nitrogen atom by a carbon atom). The origin of the NFE state will be discussed in more details in Chapter 5.

2.4 Carbon doping of BN nanotubes

The present study is motivated by a recent experimental attempt to synthesize $B_xC_yN_z$ nanotubes using an arc-discharge technique between mixed graphite-BN electrodes [34]. The nanotubes observed were identified as being BC_2N and BC_3 nanotubes. This synthesis confirmed the early theoretical prediction [53] that such compounds could be metastable. However, no pure BN nanotubes were observed. This indicates that C is very likely to form bonds with B and N and carbon appears to be an obvious candidate for substitutional doping of BN nanotubes. (We suggest the possible use of tungsten instead of carbon in the electrodes in order to synthesize pure BN nanotubes. The introduction of a thin carbon vapor in the reaction chamber would then lead to a carbon doping of the BN nanotubes).

In the previous section, we concluded that a good description of the band structure of BN nanotubes could be obtained through band folding analysis of the band structure of the related "gedanken" BN(d) structures. Therefore, doping properties of BN nanotubes and BN(d) structures should be similar. The doping of BN(d=5) by substitution of a boron atom by a carbon atom is studied here. The 5 $\AA$ separation between two neighboring BN layers is comparable to the diameter of the BN(6,0) tube. In each BN plane, we substitute a boron atom by a carbon atom and put the carbon impurity in the center of a 3×3 and a 5×5 supercell. With such a geometry, two carbon atoms are located, respectively, at 13.05 $\AA$ and 21.75 $\AA$ away from each other. The calculations are carried out with a cut-off of $E_{cut} = 36$ Ry in the planewave expansion of the eigenstates. This corresponds to an average of 16,000 planewaves in the case of the 5×5 supercell, and an iterative diagonalization technique is used to calculate the lowest desired eigenvalues.

We first minimize the total energy of the system by simultaneously moving the atoms in the direction of the Hellman-Feynman forces and reducing the stress on the unit cell. Because the C-N bond length is different from the 1.45 $\AA$ B-N bond length in hexagonal BN (in BC_2N, the C-N bond length has been calculated to be 1.35 $\AA$ [53]), the nitrogen atoms around the carbon impurity relax from their original position. At equilibrium, we find that the C-N bond length is equal to 1.42 $\AA$. The relaxation of other atoms is negligible. In the case of the 3×3 supercell, we find a similar relaxation with a 45 Ry cut-off. The relaxation energy is equal to 0.19 eV per carbon impurity.

We perform LDA band-structure calculations for both the 3×3 and 5×5 supercells in their equilibrium geometry. The band structure for the 3×3 supercell is plotted in Fig. 2.9. The donor level is easily identifiable as the nearly non-dispersive band (solid line) below the bottom of the conduction band of the corresponding undoped BN system (the non-zero dispersion is an artifact of the finite size of the 3×3 unit cell). The donor binding energy at Γ is calculated to be 0.537 eV for the 3×3 cell and 0.516 eV for the 5×5 cell. The good agreement between these two values indicates a good convergency of the present calculation with respect to supercell size. We plot in Fig. 2.10 the total charge density difference between the C-doped and the undoped BN systems in the 3×3 geometry. As expected, the charge excess is localized on the carbon atoms and hardly overlaps from one supercell to another.

In conclusion, we find that the substitution of B by C in hexagonal BN yields a deep defect level with a binding energy of ~ 0.5 eV. Therefore, carbon does not constitute a donor for doping BN and, at room temperature, very few carriers will populate the NFE state which lies at the bottom of the conduction bands of hexagonal BN. From a band-folding analysis, the same conclusion holds for BN nanotubes.

2.5 Filling of carbon nanotubes with metallic atoms

Several recent experimental and theoretical studies have shown evidence that carbon nanotubes can be filled, or "intercalated" within, by atoms, molecules, or small clusters. Specific examples include the filling of nanotubes by lead oxides [54], HF molecules [55], superconducting TaC single crystals [56], and liquid metals such as sulfur, selenium or rubidium [57]. However, the mechanisms and the conditions for filling are not understood and seem to differ significantly from one case to another. For example, in Ref. [56], carbon nanotubes have been shown to grow "around" the TaC clusters, while all other examples deal with filling of tubes which are already formed. Among these latter examples, a distinction can be made between cases where the filling is made on previously opened nanotubes [55, 57] and cases where the opening and the filling are concomitent [54]. On more general grounds, it is clear that the filling of carbon nanotubes will be very sensitively depending on factors such as the relative size of the nanotubes and the filling structure, the phase in which these structures can be found at the arc-temperature, the binding energy, viscosity, surface tension of this phase, and also the static or induced polarizability of the tubes and filling materials in the presence of each other. The very wide interest in the filling of nanotubes is of course motivated by the large range of possible applications that can be thought of for such filled nanotubes. In particular, in light of our results in the previous sections, the doping of carbon or BN nanotubes to populate the bottom of the nanotube conduction bands would be of great interest. The conductivity of these 1-dimensional materials will also be of great fundamental and practical interest. The superconducting transition temperature of TaC encapsulated in carbon nanotubes [56] have been measured to be 10.0 K. It is suggested that in such a system, both superconducting electrons and mediating phonons come from the TaC crystal alone, and the carbon nanotubes are just used as "cages" to enforce 1-dimensionality. This role of cage was also suggested in Ref. [54] in another context. The carbon nanotubes were thought of as molds for the fabrication of nanoscale metallic wires. Protection of chemical or biological functions can also be suggested as a use for the nanotubes in the "cage mode". Finally, many interesting phenomena can arise from the interaction between the nanotube and its filling. By analogy with alkali-doped fullerites (fullerides), it is of course interesting to consider filling candidates which will add conduction carriers while the tube "provides" the phonons (or vice-versa) in a possible superconducting phase. Further, as shown below, a chain of alkali atoms filling in the tubes would lose one electron per atom to the carbon tube, forming a conducting tube enclosing a 1D ionic chain.

We have carried out a study of the stability and electronic properties of metal-filled small radius nanotubes. We focus on potassium as a prototypical intercalant. We show that potassium does "intercalate" inside small radius carbon nanotubes. This is consistent with the fact that potassium atoms easily intercalates graphite

[58]. We perform *ab initio* pseudopotential LDA calculations using the same carbon pseudopotential as in section 2.2. The pseudopotential for K is generated in the ground state configuration of the atom using the scheme by Troullier and Martins [41]. An energy cut-off of 36 Ry is used in the expansion of the eigenstates in a plane-wave basis. As in the previous section, an hexagonal two-dimensional array of tubes is used, with a closest distance of 5.5 $\mathring{A}$ between atoms on neighboring tubes. We then intercalate one potassium atom per unit cell along the axis of the tube. This corresponds to 1 K atom per 4n C atom in the case of (n,0) nanotubes studied here. The geometry of a single K-doped (7,0) carbon tube is represented in Fig. 2.11. We note that the K-K distance in a free K linear chain is calculated to be 7.72 a.u. within LDA. In the geometry used here to study the intercalation of carbon nanotubes, the K atoms are located 8.22 a.u. apart from each other along the axis of the tube. We note, however, that the "bulk modulus" of the linear chain is very small (we calculate it to be 0.073 eV/a.u.) and the difference in energy for the chain with K atoms located 8.22 a.u. apart, as compared to 7.72 a.u., is only 0.011 eV per K atom.

Furthermore, we study the possibility for a Peierls transition to induce a dimerization of the K chain. Starting from a linear chain with two atoms per unit cell (that is the unit cell length is now 15.44 a.u.), we dimerize the two atoms in the unit cell without changing the unit cell length. In order to sample carefully the band gap opening at the Fermi level, we increase the k-point sampling to 150 points in the irreducible part of the BZ. We find that for dimerization corresponding to a bond length contraction larger than Δa=0.08 a.u, the linear chain is more stable by at least 0.04 meV/atom. Smaller Δa contractions have not been studied. This means that if a Peierls transition would occur, its effect will be insignificant and will be destroyed at temperature larger than 0.46 K.

Table 2.2 gives the calculated heat of formation of K-intercalated carbon nanotubes. The reference of energy for the heat of formation is the energy of the isolated tube plus the energy of a K atom in the crystal bcc phase. We note that the binding energy of K in the crystal phase, as compared to the isolated atom in its ground-state configuration, is 0.94 eV/atom [59]. Therefore, the intercalation energy gain for a K atom coming from the gas phase will be larger than the value reported in Table 2.2 by roughly 0.94 eV/atom. We study the evolution of the binding energy for the intercalation of potassium atom as a function of nanotube radius. For too small a radius, the potassium atom does not want to go inside. This can be simply understood in terms of the atomic radius of both potassium and carbon atoms as compared to the tube radius. These values are reported in Table 2.3. One can see that in the case of the smallest (6,0) tube, the sum of the potassium plus carbon atomic radii exceeds significantly the (6,0) tube radius (2.39 $\AA$). Therefore, for such a small tube, the repulsion energy due to the overlap of the potassium and carbon valence charges is too strong and the potassium atoms cannot "fit" inside. For larger tubes, this restriction is less severe and potassium does fit inside the tubes. We note that in graphite K-intercalated compounds, the graphite plane-plane distance has been measured to be equal to 5.35 $\AA$. This corresponds roughly to the diameter of the (7,0) tube. This is consistent with our finding that the largest intercalation energy for the filling of carbon nanotubes by K atoms is obtained for the (7,0) tube.

To trace the origin of the stabilization observed, we plot in Fig. 2.12(a) the band structure of the (7,0) tube alone as compared to (in Fig. 2.12(b)) the band structure of the (7,0) tube with potassium inside. In Fig. 2.12(a), NFE labels the nearly-free electron band analog to the NFE band described in the previous section for the BN tubes. We note that in the case of carbon tubes, this band is at higher energy as compared to the BN tubes case and does not play any role in determining the metallicity of the carbon nanotubes. Further, with introduction of the K atoms inside the tube, the potassium 4s band hybridizes with the NFE tube state of the undoped tube. Indeed, both states are singly degenerate and have a charge density localized along the axis of the tube. The resulting two hybrid bands are labeled (α)

and (β) in Fig. 2.12(b) and their corresponding charge density at Γ is plotted in Fig. 2.13. From the calculations, it is clear that the introduction of the potassium atom inside the tube hardly modifies the band structure of the occupied states. We reach the same conclusion for the intercalation of the smaller (6,0) tube by K. This can be understood by looking at the LDA energy levels of the isolated atoms as reported in Table 2.3. One can see that the valence 4s energy level of potassium is significantly higher in energy than both the $2s$ and $2p$ energy level of carbon. For the conduction bands, the main effect is the interaction of the K $4s$ level with the NFE band. This is not surprising since the charge density of both states strongly overlap along the axis of the tube. Further, since the potassium $4s$ band lies above the Fermi level in Fig. 2.12(b), the $4s$ electron of potassium would gained energy by being transferred to the nanotube states. The shift up of the Fermi level from Fig. 2.12(a) to Fig. 2.12(b) indeed corresponds to roughly one electron. Such a charge transfer is illustrated in Fig. 2.14(a) where we plot, in a plane perpendicular to the tube and going through a potassium atom, the total charge density corresponding to the states between the Fermi level of Fig. 2.12(a) and the one of Fig. 2.12(b). Because no hybridization occurs (the introduction of the potassium chain induces mainly a rigid shift of the nanotube band structure), we conclude that the interaction between the chain and the tube is mainly electrostatic.

The heat of formation can then be explained in a simple classical picture as the internal energy of a tubular capacitor composed of the linear potassium chain (the anode) and the carbon tube (the cathode). For larger tubes, this interaction energy decreases because both the charge transfer is smaller and the distance between the two "plates" of the capacitor increases. Since the atomic ionization energy decreases for alkali atoms with increasing mass, we expect even larger binding energy for Rb and Cs in carbon tubes of appropriate radius. We plot also in Fig. 2.15(b) the charge transfer for an K atom localized outside the tube at a distance comparable to the tube radius. The same kind of electrostatic effects as described above is expected to "glue" the K atoms on the outside of the graphite tubes. Accurate total energy calculations are difficult in this case because of a strong dipole-dipole interaction between unit cells. We note however that atoms attracted to the outside of the tubes can be easily "washed" away from the tube wall, while atoms inside the tube are protected against any mechanical or chemical agent active in the environment.

Preliminary calculations have been performed for the intercalation of lead inside carbon nanotubes. We find a very large positive formation energy of 4.5 eV/Pb for intercalation inside a (6,0) tube. Therefore, Pb will not intercalate inside the carbon nanotubes. Since Pb has a smaller atomic radius than K, the argument given above for non-intercalation of K inside a (6,0) tube does not hold for Pb. The ratio of the atomic radius of Pb to the (6,0) tube radius is equivalent to the ratio of K to the (9,0) tube. This suggests that Pb is much less likely to intercalate nanotubes as K does and that the interaction of Pb with the carbon wall is different in nature from the electrostatic interaction found in the case of K. We plot in Fig. 2.15, the Pb-intercalated (6,0) tube band-structure (Fig. 2.15(b)) as compared to the non-intercalated (6,0) tube band structure (Fig. 2.15(a)). The comparison of the two band-structures shows significant hybridization effects between the Pb-chain energy levels and the tube bands. In particular, the 6s Pb-chain band (indexed by (α)) induces significant changes in the tube band structure down to -6 eV below the Fermi level. In the conduction bands, the most important effect is the hybridization between the p_z Pb-chain state ($\hat{z}$ being the tube axis direction) (labeled γ and γ') and the $\pi^\star$-$\sigma^\star$ states described in section 2.2 (labeled β and β'). This can be understood by noting that, in Table 2.3, the atomic levels of Pb, contrary to K, are very close in energy to the C 2s and 2p energy levels. This hybridization, which does not give rise to charge transfer, reduces significantly the electrostatic energy gained by transferring electrons from the metallic chain to the carbon nanotubes. Therefore, the picture given above for the case of K of a charge transfer with electrostatic interaction breaks down for Pb. However, further calculations, including a study of intercalation of Pb with tubes larger than the (6,0) tube, are necessary to gain more insight into the physics of Pb-intercalated tubes.

We note that, in Ref. [57], pure metals in the liquid phase were found to be drawn inside carbon nanotubes only if their surface tension is smaller than a cut-off value between 100 and 200 mN/m. These experimental findings were explained in terms of classical arguments which relates the wetting properties, and in particular the liquid-solid contact angle, to the values of the surface tension at the solid-vapor and solid-liquid interface. Since the surface tension of liquid K is roughly 390 mN/m, it should not intercalate inside nanotubes. However, the tubes synthesized in Ref. [57] were of the order of 10 nm wide in diameter. This is much larger than the tubes we study in this section. As pointed out by the authors of Ref. [57], the classical and macroscopic arguments they used are expected to break down for very small size nanotubes. This is confirmed by the present work where charge transfer and hybridization effects at the atomic level are shown to be responsible for the filling properties of small size carbon nanotubes by metallic atoms.

2.6 Conclusion

In this chapter, some fundamental structural and electronic properties of carbon and BN nanotubes were studied. We showed that important and unexpected properties arise from the nanometer size scale and reduced dimensionality of these new compounds. However, many interesting questions and problems remain unanswered. A important issue is the understanding of the growth mechanism responsible for the synthesis of nanotubes. Are the tubes growing capped or uncapped? Do they grow from an end in contact with the electrode or from a free end ? What is the influence of the electric field in the arc ? The answers to these questions will certainly improve our ability in the making of nanotubes, so that a better control over the size, helicity or filling of the tubes may be achieved during the synthesis process. Another important direction is the study of the electronic excitations in nanotubes which is important for the application of their optical and transport properties. Such an area is yet to be explored in any details both theoretically and experimentally. Experimentally, as mentioned above, the difficulty comes from being able to synthesize and isolate tubes with well defined radius and helicity. For example, the large variety of transport responses, which are expected from single carbon nanotubes with varying radius and helicity, have been recently shown to be averaged out in experiments performed on pellets of nanotubes (the response is then similar to that of plain polycrystalline graphite pellets [60]). From the theoretical point of view, the large size of the supercells used in the previous section to study the nanotubes is such that it is not practicable to calculate their electronic excitations using more accurate *ab initio* many-body formalisms. Even more difficult would be the calculation of the polarizability of an open-ended nanotubes, because this would require the construction of a supercell which extend also in the direction of the tube axis. This kind of study is nevertheless crucial for the understanding of the growth mechanism of nanotubes.

To overcome this problem, we present and test in Chapter 6 a novel approach for the calculation of the dynamical RPA dielectric response. This approach, based on a mixed-space implementation of the linear response theory, is particularly efficient in the case of large supercells which contain a significant amount of vacuum space. Nanotubes are ideal candidates for the use of such an approach. Applications of this novel formalism to quasiparticle calculations will be also discussed in Chapter 6.

There are many other issues remaining to be explored:

- because of the strength of the C-C or B-N bonds, we can expect very interesting plastic properties for these "nanometer fibers".
- the chiral structures of some nanotubes suggest that chiral currents may be possible on such tubes. This would lead to a net induced magnetic field along the tube axis, and tubes would then be nanoscale solenoids. Preliminary results show that BC_2N

nanotubes may be candidate to support such chiral currents [61].
- the study of the capillarity action of nanotubes should tell us if such "nanometric straws" can be used to "pump" selected compounds at the atomic or molecular level. Direct applications to the extraction and protection of atoms and molecules can be suggested.
- a recent experimental study [62] showed that carbon nanotubes have a significantly larger orientationally averaged magnetic susceptibility than any other forms of carbons. A theoretical study for the understanding of such a phenomenon would be of great interest.
- because interaction between concentric tubes in multi-wall nanotubes is small (Van der Waals interactions), one expects some concentric tubes to be incommensurate to each other. In such a case, what becomes of the band structure picture when the periodicity is broken along the axis of the tubes ? This is reminiscent of quasi-crystals, and we expect localized states to appear which may modify significantly the transport properties of the concentric nanotubes as compared to single-wall nanotubes.

This short list is of course not exhaustive. We can expect many more novel phenomena to arise from this new class of materials, which will challenge the imagination of the materials community.

Table 2.1: Band gap (in eV) of selected carbon tubes. All gaps given are direct and at the Γ-point. For the metallic case, the overlap of the bands is given as a negative gap.

tube	Tight Binding	Present calculations	
	Ref. [37]	TB	LDA
(6,0)	~ 0.2	0.05	metal (- 0.63)
(7,0)	~ 1	1.04	0.09
(8,0)	1.22	1.19	0.62
(9,0)	0.04	0.07	0.17

Table 2.2: Diameter ($\AA$) and binding energy (eV/K atom) for K-intercalated (n,0) carbon tubes. The heat of formation is defined as the energy of the K-intercalated tube (in the geometry described in the text) minus the energy of the tube alone and the energy of a K atom in the BCC crystal structure.

tube	diameter ($\AA$)	binding energy (eV)
(6,0)	4.78	0.001
(7,0)	5.56	1.12
(8,0)	6.34	1.07
(9,0)	7.13	0.30

Table 2.3: Selected radii and atomic energy levels for C, K and Pb calculated in the ground state configuration from LDA calculations. For Pb, semi-relativistic energies are provided. Energies are in eV and radii in Å. The atomic radii are given for the element in the crystal environment (the crystal type is indicated in parenthesis). For K, the ionic radii is given for the isolated ion.

	C		K		Pb	
atomic radius	(diamond)	0.77	(bcc)	2.26	(fcc)	1.75
ionic radius			(K^+)	1.33		
crystal E_b				0.94		2.04
atomic levels (LDA)	(2s)	-13.63	(4s)	-2.42	(6s)	-12.20
	(2p)	-5.41	(4p)	-0.84	(6p)	-4.81

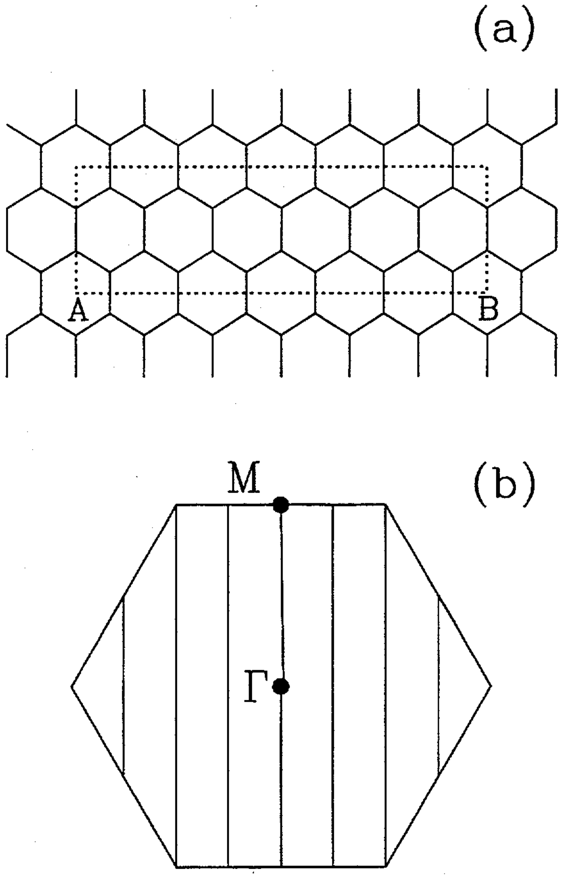

Figure 2.1: (a) Unit cell of the (6,0) carbon tube mapped onto the graphite sheet. For the tube, point A is rolled onto point B. (b) Brillouin zone of the graphite sheet. The vertical lines mark the set of allowed k vectors for the tube.

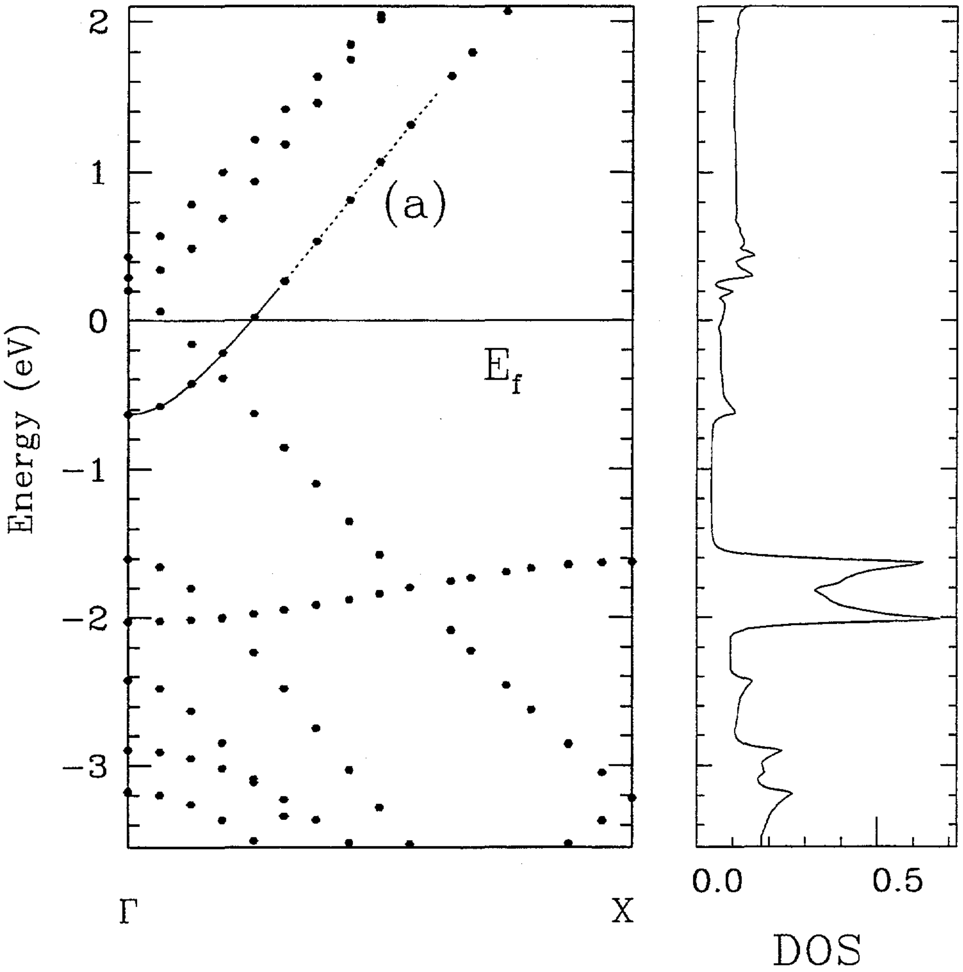

Figure 2.2: Band structure and density of states (states/eV-atom) for the (6,0) carbon tube. The energies are in eV and the zero is at the Fermi level. We trace the $\sigma^\star$-$\pi^\star$ hybridized band (a) around the center of the Brillouin zone as a guide to the eye.

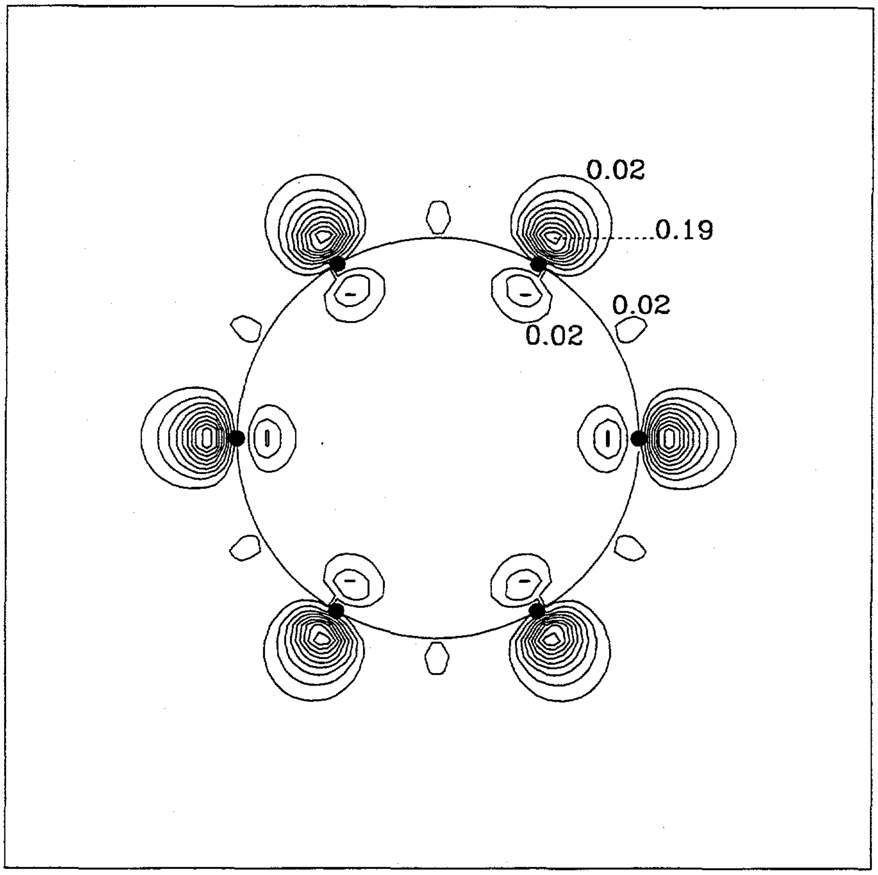

Figure 2.3: Contour plot of the charge density for $\sigma^\star$-$\pi^\star$ hybrid state (a) at Γ for (6,0) carbon tube. The contours are in a plane perpendicular to the axis of the tube which contains six carbon atoms. The numbers quoted are in units of e/[a.u.]^3. The circle represents a cross section of the cylinder on which the atoms lie.

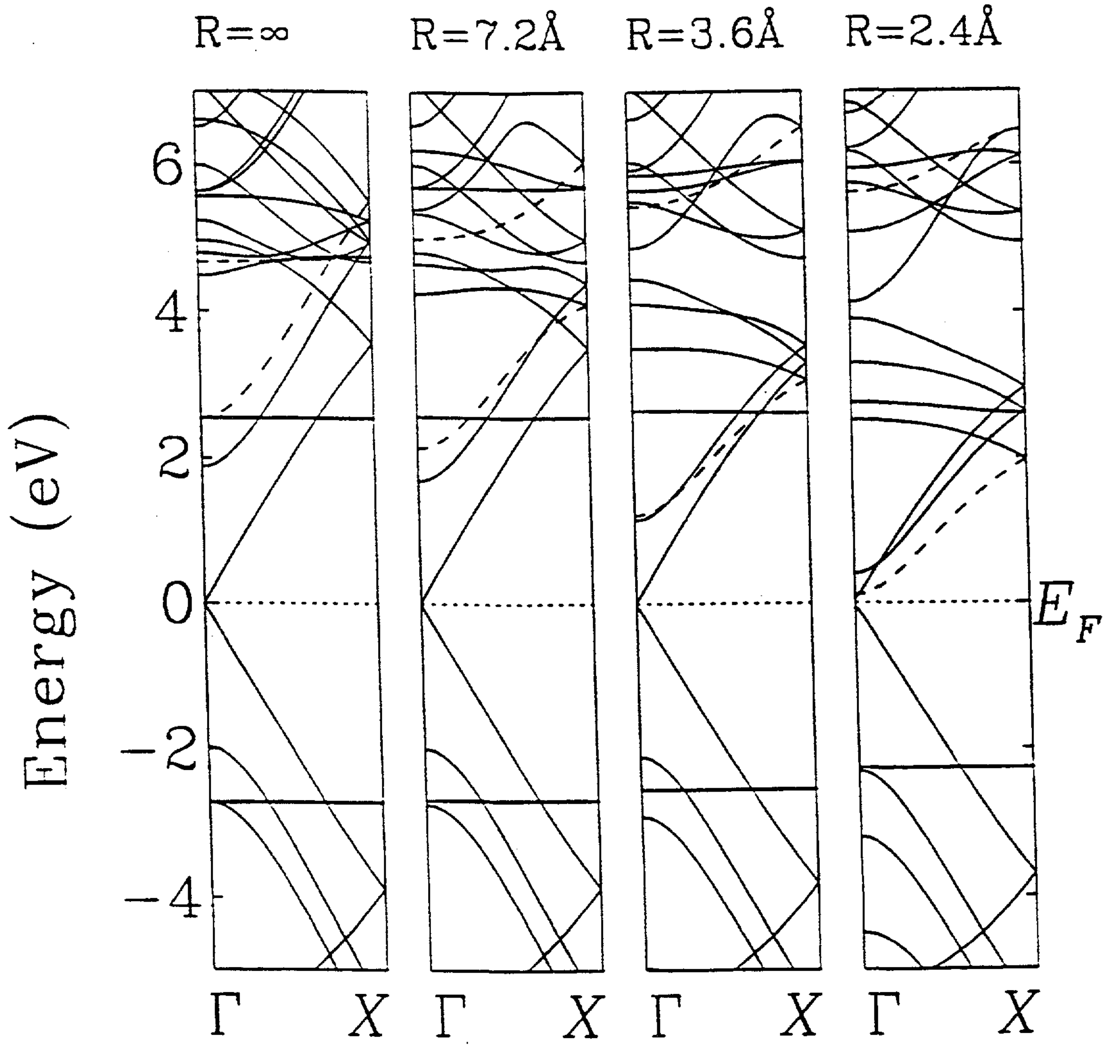

Figure 2.4: Evolution of the graphite TB bands near the Fermi level for the (6,0) geometry under increasing curvature. Energies are in eV and the zero is set at the Fermi level. The dashed curves mix strongly with each other due to curvature. In an LDA calculation, the lower one would span the gap. The radii of curvature are indicated.

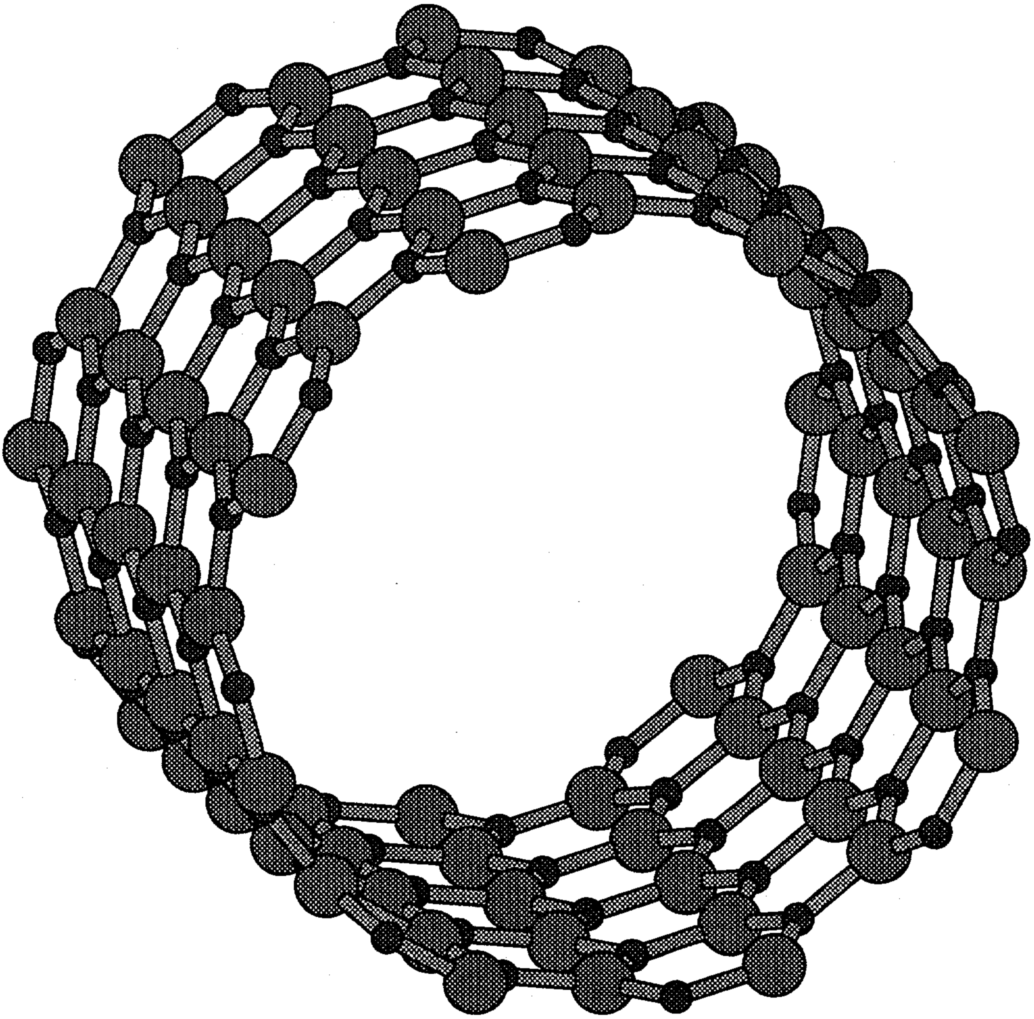

Figure 2.5: Buckled BN (8,0) tube. The larger atoms are the N atoms and the smaller one the B atoms. The B-N bond length is set to 1.34 Å.

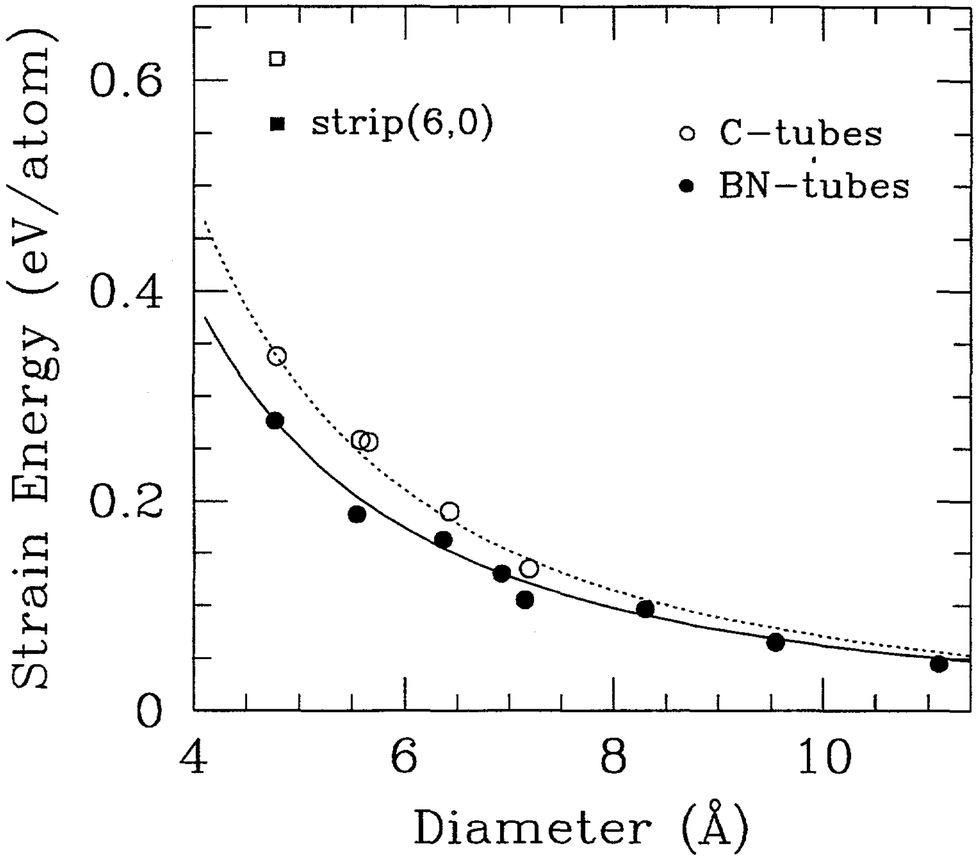

Figure 2.6: Total energy of nanotubes in eV/atom as a function of tube diameter (in Å). The black circles represent the BN nanotube energies above the energy of an isolated hexagonal BN sheet. The opened circles represent the graphite nanotubes energies above the energy per atom of an isolated graphite sheet. The solid and dashed lines are guides to the eye. The energy of the strips corresponding to the (6,0) BN and carbon tubes are given respectively by the filled and empty square.

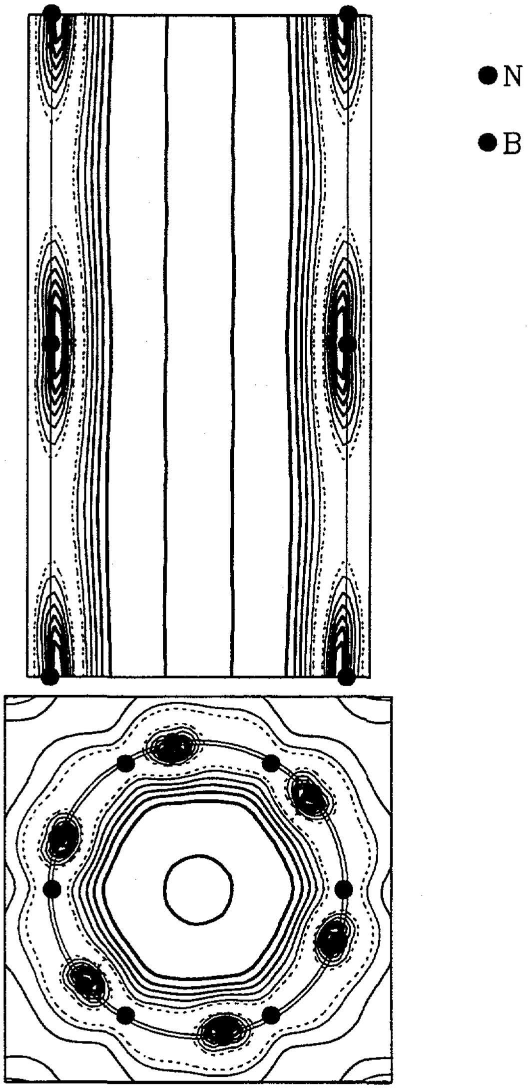

Figure 2.7: Contour plot of the charge density corresponding to the bottom of the conduction band state at Γ for the (6,6) BN nanotube. a) Plot in a plane containing the axis of the tube and N atoms. N atoms are indicated by empty circles. b) Plot in a plane perpendicular to the tube axis containing B and N atoms. B atoms are represented by filled circles. The minimum contour line (dashed line) corresponds to 0.04 e/[a.u.]^3 and the maximum to 0.026 e/[a.u.]^3 (thicker black line). We draw the two concentric B- and N-cylinders to stress the buckling relaxation. The parabolic dispersion of the NFE state can be described through the band-folding picture (see text).

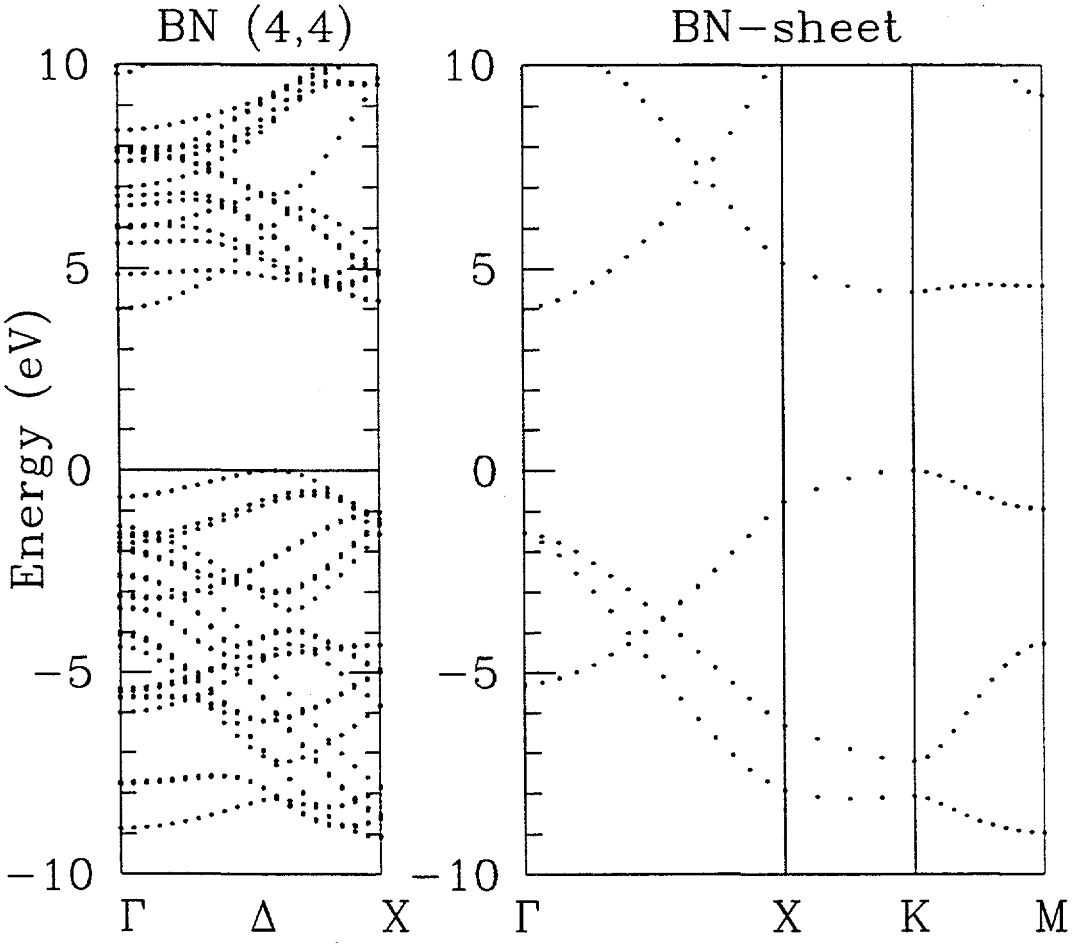

Figure 2.8: Band structure of the BN (4,4) tube compared to hexagonal BN band structure plotted along high-symmetry directions of the 2D hexagonal Brillouin zone. X is between Γ and K with $\Gamma X = 3/4\,\Gamma K$. Energies are in eV and the zero of energy is at the top of the valence band for both structures.

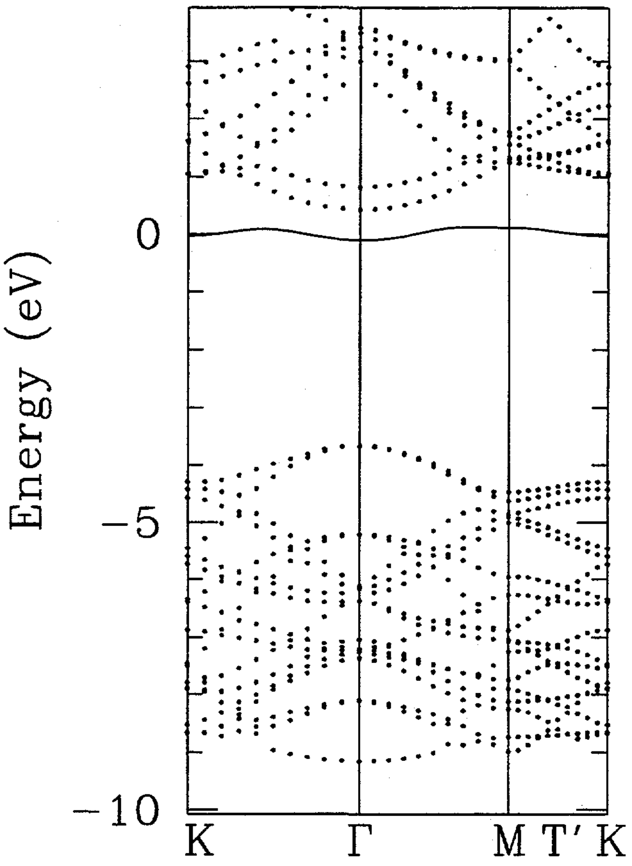

Figure 2.9: Band structure for the hexagonal BN-C doped system in the 3×3 supercell geometry. Energy bands are plotted along high-symmetry directions of the 2D hexagonal Brillouin zone. The solid line indicates the donor level. Energies are in eV. The zero of energy is set to the Fermi level.

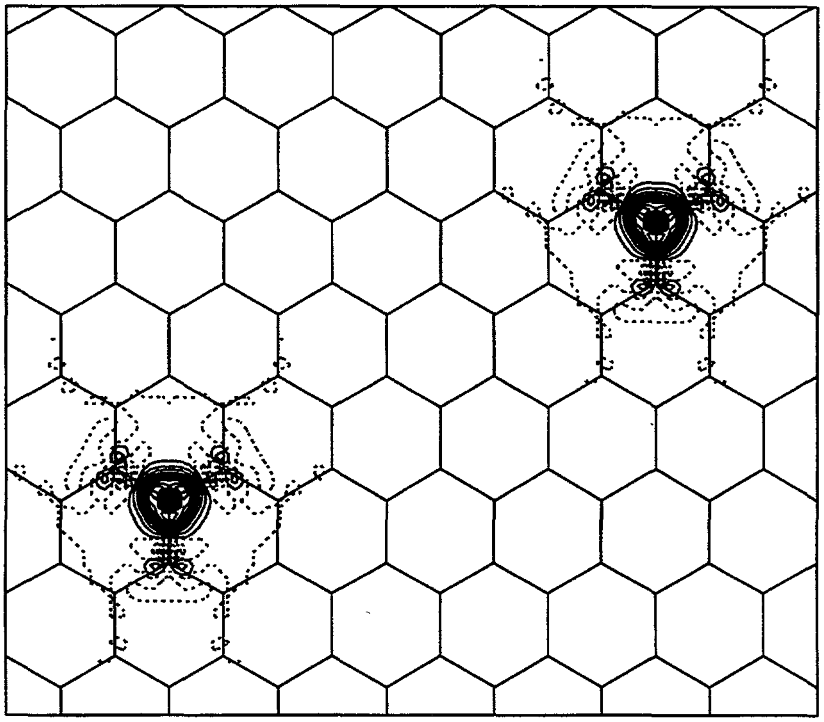

Figure 2.10: In-plane charge density for the C-doped BN sheet minus the charge density of the undoped sheet in the the 3x3 supercell geometry. The full line contours indicate an excess of charge and the dotted line contours a deficit of charge. Two carbon atoms are represented. 20 contours are plotted with constant density increment between the minimum and maximum value of the differential charge.

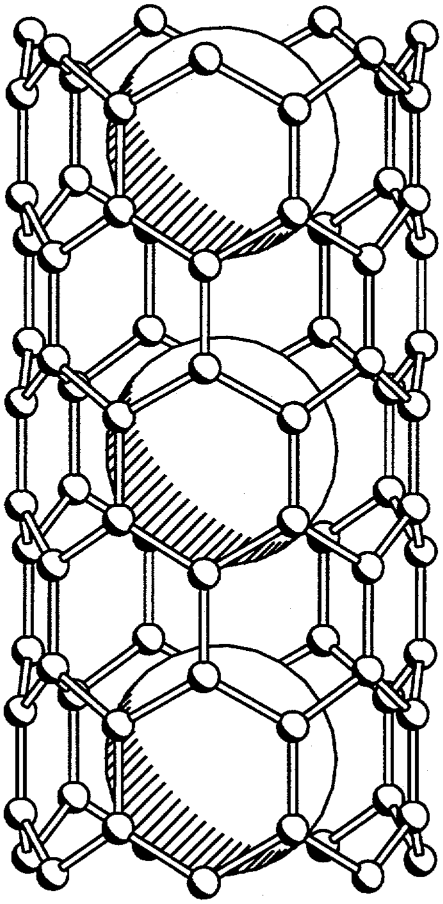

Figure 2.11: Atoms and bonds representation of an K-intercalated (7,0) carbon nanotube. The diameter of the tube is 5.56 Å, the C-C bond length 1.43 Å and the radius of the K atoms as been set to roughly the atomic radius. 3 unit cells are represented.

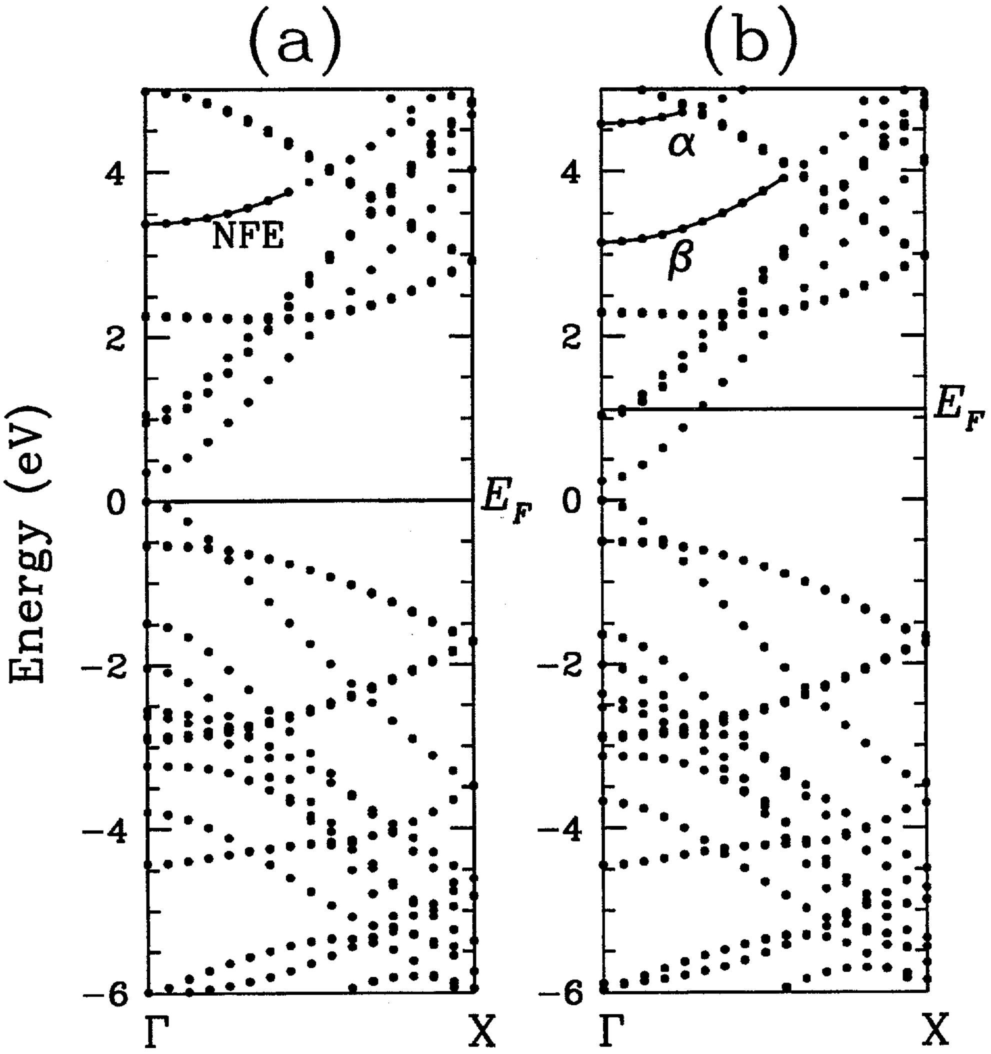

Figure 2.12: Band structure for (a) pure (7,0) carbon nanotube and (b) K-intercalated (7,0) carbon nanotube. Energies are in eV. The reference of energy is taken to be the top of the valence band for the undoped tube. NFE labels the nearly-free electron band of the undoped tube while α and β label the two bands resulting from the hybridization of the undoped tube NFE band with the $4s$ K-chain band.

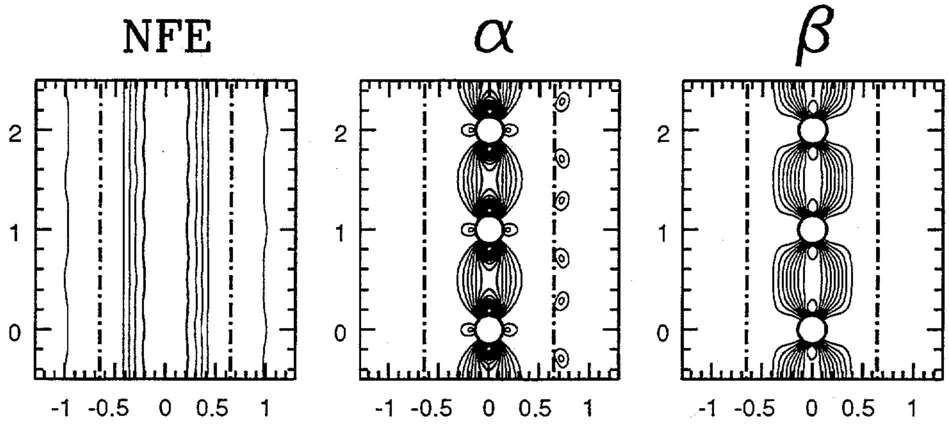

Figure 2.13: Contour plot of the charge density associated with the NFE state and the NFE-K_{4s} hybrid states α and β at Γ for the K-doped carbon (7,0) tube.

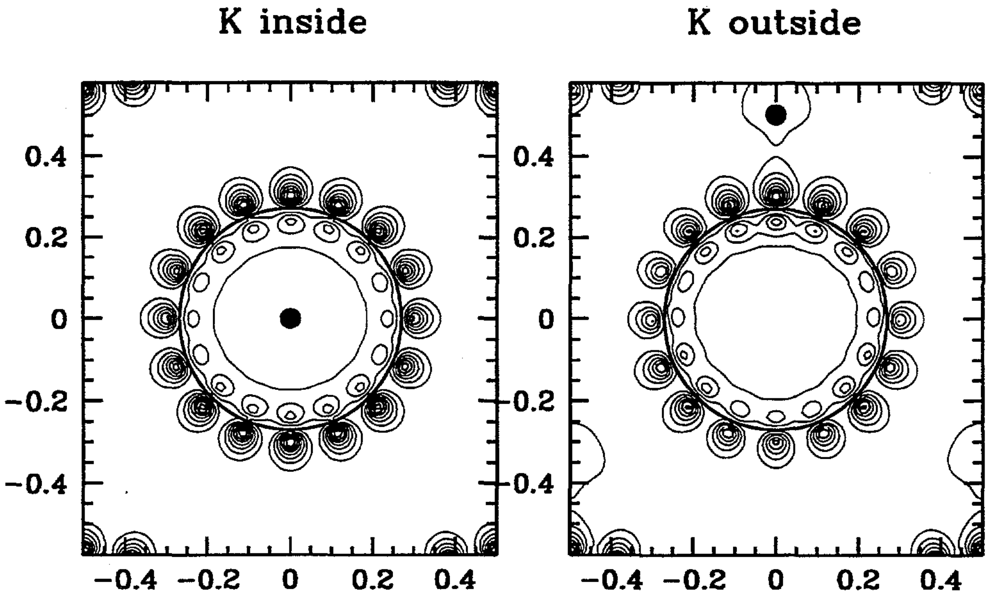

Figure 2.14: (a) Projection on a plane perpendicular to the tube axis of the charge density associated with all states with energy between the zero of energy and the Fermi level of the band-structure for the K-intercalated (8,0) carbon nanotube as represented in Fig. 2.12. (b) Same plot, but with the K atoms outside the tube and distant from the tube wall by the tube radius. The lengths indicated on the framing boxes are in unit of 22.61 a.u.

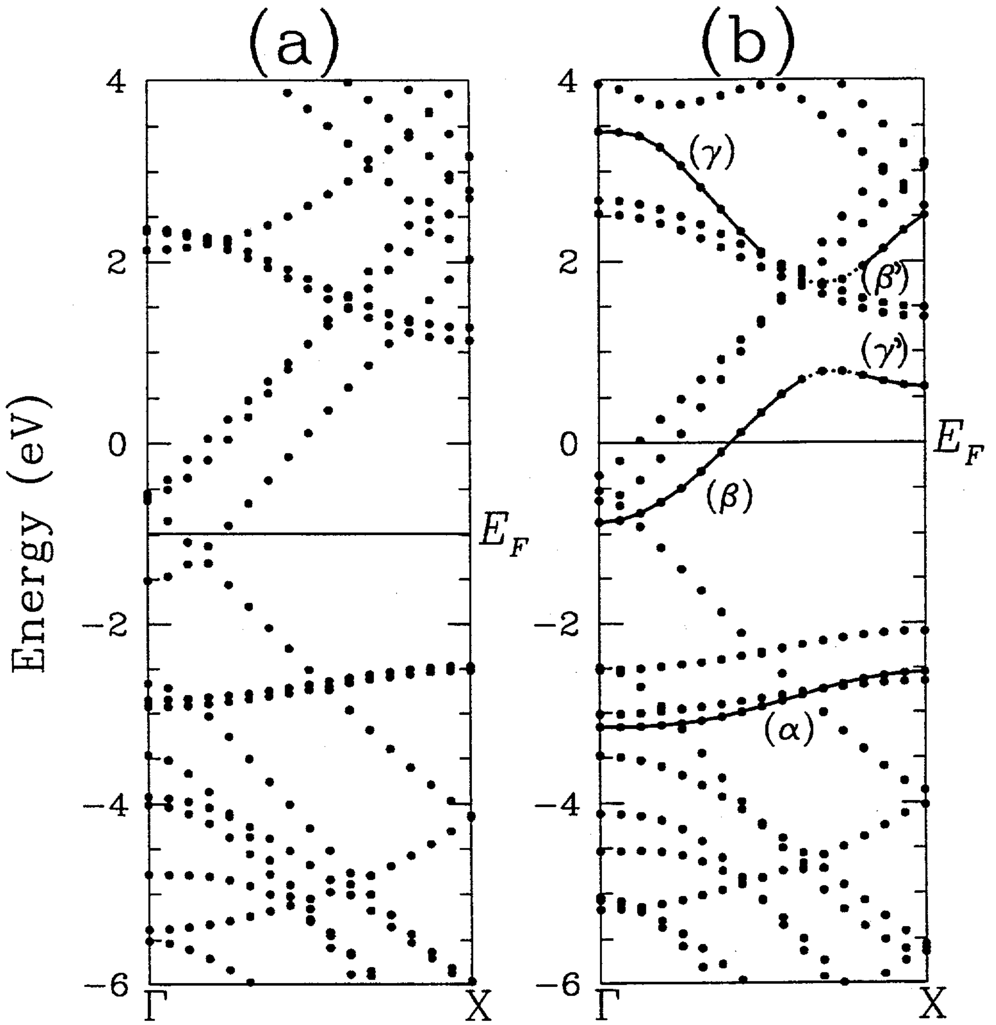

Figure 2.15: LDA band-structure for (a) an isolated (6,0) carbon tube and (b) a Pb-intercalated (6,0) tube. The label α indicates the Pb-chain 6s band. The labels β-β' and γ-γ' indicate respectively the the σ^*-π^* hybrid tube band and the Pb-chain $6p_z$ band which have hybridized in the Pb-intercalated tube. Energies are in eV.

Chapter 3

Self-Energy Effects on the Surface States of H-Si(111)-(1×1)

3.1 Introduction

Recently, the development of a new wet chemical treatment [63, 64] has allowed the preparation of very flat, highly stable and nearly defect free hydrogen-terminated Si(111) surfaces. The quality of these surfaces is characterized by the exceptionally small linewidth of electronic and vibrational states in photoemission [65] and vibrational [63, 64, 66] spectroscopy experiments. This has generated much renewed interest in this system since measurements can now unravel very fine structures in the spectroscopic data with very little inhomogeneity or impurity broadening.

The present work is motivated by a recent high resolution angle resolved photoemission spectroscopy (ARPES) experiment performed on such an "ideal" H-Si(111)1×1 surface [67]. The spectra were obtained using the French-Swiss beam line (SU3) at SuperACO in LURE [68]. The quality of the surface, combined with a state-of-the-art instrumental resolution (25 meV for valence states), yields surface states in the ARPES data with a typical linewitdh of 300 meV, much smaller than those measured with samples from other preparation methods such as by adsorbing atomic hydrogen on freshly cleaved Si(111) surfaces [69] or those of the ideally H-terminated Si(111)1×1 surfaces obtained by removal of an indium adalayer by atomic hydrogen [70].

In this chapter, we address mainly the issue of the surface states located in the Si valence bands. Surface states in the conduction bands have also been previously studied experimentally and theoretically [71] but these states are weak resonances.

Surface states in the valence bands of the H/Si(111) surface have been examined in several previous calculations [71, 72, 73, 74]. Although the character of these states is qualitatively understood, discrepancies in their energy locations as large as 1 eV were found between theory and experiment. This is because the previous studies were either semi-empirical [72, 73, 74] in nature or were based on the local density approximation [71] which does not provide an accurate description of the quasiparticle energies measured in the photoemission process.

In order to make a direct comparison with the experimental data, we have performed a first-principles calculation of the quasiparticle surface state energies. The computation of the quasiparticle energies is achieved using the self-energy method [2] which has been referenced and discussed in Chapter 1.

The remainder of this chapter is organized as follows: in section 3.2, we discuss the theoretical methods employed in this study. The *ab initio* pseudopotential method employing a plane wave basis set in a supercell slab geometry was used to determine the surface structure and vibrational properties of the Si-H stretching mode. The bulk and surface state energies were calculated using the first-principles quasiparticle approach. In section 3.3, the theoretical results are presented and compared with data from spectroscopic measurements. Finally, a summary and conclusions are given in section 3.4.

3.2 Theoretical methods

3.2.1 LDA *ab initio* pseudopotential total energy calculations

The LDA calculations were carried out using *ab initio* pseudopotentials. For Si, we use the Hamann, Schlüter and Chiang pseudopotential scheme [75]. For hydrogen, the pseudopotential is obtained using a modified Kerker scheme [76] based on the inversion of the exact hydrogenic Schrödinger equation. This scheme provides a very smooth pseudopotential for hydrogen with excellent transferability. The

Ceperley-Alder exchange and correlation potential [77] was used. The potentials and eigenstates are expanded in a planewave basis. The calculations were carried out using a cut-off of $E_{cut} = 16$ Ry in the planewave expansion of the wavefunctions. This cut-off corresponds to an average of 2200 planewaves in the basis set for the surface calculation described below. We exploited an iterative diagonalization technique [6] to calculate the desired lowest eigenstates. A 4×4×1 grid in the Monk-Pack scheme [78] was used to generate 10 special k-points in the irreducible part of the two - dimensional surface Brillouin zone (SBZ).

In each supercell, we have a 12 layer Si slab terminated by hydrogen saturating the dangling bond on each side. With this geometry, our slab retains inversion symmetry. The vacuum between adjacent slabs was chosen to be 12 a.u. This vacuum region is large enough as confirmed by the absence of dispersion for the slab band structure in the direction normal to the surface and by the flatness of the total potential in the middle of the vacuum region. We checked also the convergence in the thickness of the slab: the overlap through the slab for the surface states located on two hydrogen atoms on the opposite side induces a splitting of the surface state energies which is at most 0.1 eV. The surface state energies given below are taken to be simple algebraic average of the energy of the split levels.

For the specific study of the Si-H stretching mode, we increased the energy cut-off up to $E_{cut} = 20$ Ry: going from 16 Ry to 20 Ry reduces the fundamental frequency by 8 %.

3.2.2 First-principles quasiparticle approach to electron excitation energies

The computation of the quasiparticle energies is achieved using a self-energy approach. In this formalism, the Schrödinger-like equation solved to obtain the one-particle excitation energies E_{qp} is given by:

$$[\hat{T} + V_{ext}(\mathbf{r}) + V_H(\mathbf{r})]\Psi^{qp}(\mathbf{r}) + \int d^3\mathbf{r}\ \Sigma(\mathbf{r},\mathbf{r}';E^{qp})\Psi^{qp}(\mathbf{r}') = E^{qp}\Psi^{qp}(\mathbf{r}), \tag{3.1}$$

where $\hat{T}$ is the kinetic energy operator, V_{ext} the external potential, and V_H a mean-field electron-electron interaction potential (the Hartree potential in this case.) The self-energy operator Σ includes the effects of exchange and correlation: it is non-local, energy-dependent and non-hermitian in general.

In the GW approximation [2, 3] used in this calculation, Σ is taken to be the first order term in an expansion in successive powers of the screened interaction W:

$$\Sigma(\mathbf{r},\mathbf{r}';E^{qp}) = i\int \frac{dE'}{2\pi} e^{-i\delta E'}\, G(\mathbf{r},\mathbf{r}';E-E')W(\mathbf{r},\mathbf{r}';E'), \tag{3.2}$$

where G is the dressed one-particle Green's function. Our approach [2] is to make the best possible approximation for G and W. As shown in previous GW calculations in semiconductors, the LDA wavefunctions accurately describe the quasiparticle wavefunctions in semiconductors so that we may write:

$$G(E) = \sum_{n\mathbf{k}} \frac{|n\mathbf{k}><n\mathbf{k}|}{E-E_{n\mathbf{k}}-i\eta}, \tag{3.3}$$

with $|n\mathbf{k}>$ the LDA eigenfunctions and $E_{n\mathbf{k}}$ the self-consistent quasiparticle energies (η is a negative infinitesimal for energies above the Fermi energy and a positive infinitesimal below).

The screened Coulomb interaction $W = V * \epsilon^{-1}$ is calculated in Fourier space using the Hybertsen-Louie scheme [2, 79]. V is the bare Coulomb potential and ϵ^{-1} the inverse dynamical dielectric matrix. In calculating ϵ^{-1}, the static polarizability χ^0 is evaluated in the Adler-Wiser formulation [80, 81] within the Random Phase Approximation (RPA):

$$\chi^0_{\mathbf{G}\mathbf{G}'}(\mathbf{q}) = \frac{4}{\Omega}\sum_{c,v,\mathbf{k}} \frac{<v,\mathbf{k}|e^{-i(\mathbf{q}+\mathbf{G})\cdot\mathbf{r}}|c,\mathbf{k}+\mathbf{q}><c,\mathbf{k}+\mathbf{q}|e^{i(\mathbf{q}+\mathbf{G}')\cdot\mathbf{r}'}|v,\mathbf{k}>}{\epsilon_{v,\mathbf{k}}-\epsilon_{c,\mathbf{k}+\mathbf{q}}+i\delta}. \tag{3.4}$$

The above equation has been explicitely written for a system with an energy gap between occupied and unoccupied states. Local field effects are taken into account so that the polarizability matrix is non-diagonal in reciprocal space. This is the most time consuming part of our scheme. The dielectric function $\epsilon_{G,G'}(\mathbf{q})$ is then calculated within RPA:

$$\epsilon_{\mathbf{GG'}}(\mathbf{q}) = \delta_{\mathbf{GG'}} - \frac{4\pi e^2}{|\mathbf{q}+\mathbf{G}|^2}\, \chi^0_{\mathbf{GG'}}(\mathbf{q}) \ , \tag{3.5}$$

and the inverse dielectric function is obtained through inversion of Eq. 3.5. Special care must be taken for the head ($\mathbf{G}, \mathbf{G'}$=0) and wings ($\mathbf{G}$=0 and $\mathbf{G'} \neq 0$, or vice-versa) of $\chi^0_{\mathbf{GG'}}(\mathbf{q})$ when $\mathbf{q} \to 0$ and the applicability of Eq. 3.5 relies on the knowledge of the coefficients for the q^2 dependence of the head and q dependence of the wings in the long wavelength limit. Such leading coefficients can be obtained from $\mathbf{k} \cdot \mathbf{p}$ perturbation theory, yielding in particular:

$$< v, \mathbf{k}|e^{-i\mathbf{q}\cdot\mathbf{r}}|c, \mathbf{k}+\mathbf{q} >= \frac{< v, \mathbf{k}| - 2i\mathbf{q}\cdot\nabla_{\mathbf{r}} + [V_{NL}, i\mathbf{q}\cdot\mathbf{r}]|c, \mathbf{k} >}{\epsilon_{v,\mathbf{k}} - \epsilon_{c,\mathbf{k}}} \ , \tag{3.6}$$

where V_{NL} is the non-local part of the ionic pseudopotential. This step is one of the bottle-neck of the calculation, scaling as N^6 for the calculation of the head, where N is the number of planewaves used to expand the wavefunctions. We will see in Chapter 6 that such a N^6 calculation can be avoided in a mixed-space formalism. Once the static inverse dielectric matrix $\epsilon^{-1}(\mathbf{q}, \omega = 0)$ is obtained, we extend ϵ^{-1} to finite frequencies using a generalized plasmon pole model [79] which yields a different pole at $\tilde{\omega}_{\mathbf{G},\mathbf{G'}}(\mathbf{q})$ for each element $\epsilon^{-1}_{\mathbf{G},\mathbf{G'}}(\mathbf{q};\omega)$ of the inverse dielectric matrix. The strength and position of each pole are uniquely determined by imposing that $\epsilon^{-1}_{\mathbf{G},\mathbf{G'}}(\mathbf{q};\omega)$ satisfies both the Kramers-Kronig relations:

$$Re\epsilon^{-1}_{\mathbf{G},\mathbf{G'}}(\mathbf{q};\omega = 0) = \delta_{GG'} + \frac{2}{\pi}\, P \int_0^\infty d\omega\, \frac{1}{\omega}\, Im\epsilon^{-1}_{\mathbf{G},\mathbf{G'}}(\mathbf{q};\omega) \ , \tag{3.7}$$

and the generalized f-sum rule:

$$\int_0^\infty d\omega\, \omega\, Im\, \epsilon^{-1}_{GG'}(\mathbf{q},\omega) \ = -\frac{\pi}{2}\, \omega_p^2\, \frac{(\mathbf{q}+\mathbf{G})\cdot(\mathbf{q}+\mathbf{G'})}{|\mathbf{q}+\mathbf{G}|^2}\, \frac{\rho(\mathbf{G}-\mathbf{G'})}{\rho(\mathbf{0})} \ , \tag{3.8}$$

where $\omega_p = ne^2/mc$ is the classical plasmon frequency.

The quasiparticle excitation energies are then calculated using first order perturbation theory:

$$E_{n\mathbf{k}}^{qp} = E_{n\mathbf{k}}^{LDA} + < n\mathbf{k}|\Sigma(E_{n\mathbf{k}}^{qp}) - V^{LDA}|n\mathbf{k} > . \tag{3.9}$$

The validity of Eq. 3.9 is based on that the LDA and quasiparticle wavefunctions are, in general, in excellent agreement [2]. Thus, one needs only to calculate the diagonal elements of the difference Hamiltonian $\Sigma(E_{n\mathbf{k}}^{qp}) - V^{LDA}$.

In the calculation, the static polarizability $\chi^0(\mathbf{q}, \omega = 0)$ was evaluated using 10 special $\mathbf{q}$-points in the irreducible part of the SBZ. The $\chi^0_{\mathbf{GG}'}$ matrix elements were calculated for $|\mathbf{q} + \mathbf{G}| < 3.0$ a.u. which yields dielectric matrices of average size of 950×950 for each special $\mathbf{q}$-point. This is sufficient to describe the local field effects in the dielectric screening in the present case. We also included transitions up to 350 conduction bands for each $\mathbf{k}$-point.

The calculation of the self-energy matrix elements [2] requires smaller cut-off: we used $|\mathbf{q} + \mathbf{G}| < 2.8$ a.u. to converge the bare exchange energies and $|\mathbf{q} + \mathbf{G}| < 2.1$ a.u. for the dynamical part of Σ. Over 350 bands in the summation over conduction states were used for the Coulomb-hole term [2]. With these cut-offs, the self-energies are found to converge to within 0.1 eV.

3.3 Results and analysis

3.3.1 Structure and H/Si stretching mode

By total energy minimization within LDA, we find that the Si-H bond length for the unreconstructed surface is 2.87 a.u, in good agreement with previous calculations (2.80 a.u. [71] and 2.90 a.u. [82]). For the silicon substrate, we start with the experimental bulk silicon lattice constant. The first layer is found to be slightly relaxed inward by 0.075 a.u. while relaxation of deeper layers is negligible. The inward relaxation of the first layer is 0.03 a.u. larger than the value calculated in Ref. [82]: difference in the number of layers, width of the vacuum space and k-point sampling may account for this discrepancy which has only a very small effect on the total energy. The position of the surface states and the parameters of the Si-H stretching vibrational mode are insensitive to such a small variation in the first layer relaxation. We give in Fig. 3.1 a schematic representation of the H/Si(111)-(1×1) surface with the calculated LDA equilibrium bond lengths given in $\mathring{A}$.

The stretching vibrational mode of the Si-H bond was investigated using the frozen-phonon method of Ref. [83]. We find that the hydrogen moves in a potential well (see Fig. 3.2) which can be well described using the following fourth order polynomial expression:

$$V(z) = V_0 + 0.543z^2 - 0.781z^3 + 0.771z^4, \tag{3.10}$$

where the energies are in Ry and z is the deviation from equilibrium of the Si-H bond length in Ångstrom. With this potential, we find a harmonic frequency of $\hbar\Omega_0$= 251.2 meV (2025.0 cm^{-1}) and the difference between the overtone frequency and twice $\hbar\Omega_0$ to be -2Γ= 4.1 meV (33.4 cm^{-1}) in excellent agreement with the theoretical value in Ref. [82] in the case when no coupling with the wagging modes is considered. As described in Ref. [82], these values can be successfully used as parameters to describe phonon-phonon interactions through a negative-U Hubbard type Hamiltonian which yields an excellent value for the binding energy of the two-phonon bound state recently observed in this system.

3.3.2 Surface-state energies

The results of the LDA and quasiparticle surface-state band structure calculations are presented in Fig. 3.3 . In the background is the continuum of Si bulk quasiparticle states projected along the (111) direction onto the SBZ. For each $\overline{k}$

parallel to the surface (along $\overline{\Gamma}$-$\overline{K}$-$\overline{M}$-$\overline{\Gamma}$), we projected the energy levels of the quasiparticle bulk states of 100 regularly spaced **k**-points of the bulk fcc Brillouin zone. This presentation of the projected quasiparticle band structure, in contrast to a uniform shading of the bulk continuum, allows the detection of lines of high density of bulk states in the continuum . They are in excellent agreement with the ARPES data [67] and are valuable in identifying bulk peaks as compared to surface related peaks in spectroscopic data. These bulk states are calculated in the framework of our first-principle quasiparticle approach using the usual diamond-structure unit cell of bulk silicon. Most importantly for the study of surface states, the calculated pockets in the projected bulk band structure are in excellent agreement with experiment.

LDA results

In Fig. 3.3, the LDA surface state eigenvalues are given by the solid lines while the experimental values are given by the black squares. Well-defined surface states exist in each local gap (or pocket) of the projected bulk band structure near $\overline{K}$ and $\overline{M}$. These states have wavefunctions which are highly localized at the surface (Fig. 3.4(a),(c),(d)). The states (a) at $\overline{K}$ (Fig. 3.4(a)) and (a') at $\overline{M}$ (Fig. 3.4(d)) are the results of the hybridization of the Si $3p_z$ orbital with the H 1s orbital, while interactions of the Si 3s and the H 1s orbitals are responsible for the low lying surface states (b) at -7.85 eV at $\overline{K}$. The enhancement of the **k**-resolved local density of states (LDOS) on the first H layer at the calculated surface state energies as compared to the bulk density of states (DOS) at $\overline{K}$ and $\overline{M}$ (Fig. 3.5(b),(c)) further illustrates the localized character of these states. The state (a') at $\overline{K}$ is found in the LDA calculations to be within the bulk continuum but of a different symmetry than the surrounding bulk states. The corresponding wavefunction (see Fig. 3.4(b)) is very delocalized as compared to the state (a') at $\overline{M}$. However, an analysis of the symmetry of this state clearly shows that this state is hydrogen induced and is the continuation of the *bona fide* surface band (a') along $\overline{K}$ to $\overline{M}$.

An angular decomposition of the wavefunction around the hydrogen atom and the first layer silicon atom showed distinctly a different character for this state from that of surrounding bulk states: the states (a') at $\overline{M}$ and $\overline{K}$ have the same character at the surface.

To examine whether the larger delocalization of the surface state (a') at $\overline{K}$ is the result of being incorrectly positioned within LDA, we performed a Slater-Koster [40] tight-binding (TB) calculation on our 12 Si-layer slab using Pandey's nearest and second nearest neighbors parameters [73]. (The TB results do not yield a surface resonance for the surface state (a') at $\overline{K}$.) We compared first our tight-binding surface state energies with Pandey's results for a 36 Si-layer slab. The results are quoted in Table 3.1. The energies of the surface states as given by the two TB calculations differ by less than 0.11 eV (which also confirms that our slab is thick enough). Consistent with Pandey's findings, our tight-binding calculation locates the state (a') at $\overline{K}$ well within the small pocket of the projected bulk continuum. Moreover, in agreement with our LDA calculations, the wavefunction at $\overline{K}$ is much less localized than that at $\overline{M}$: only 35 % of the wavefunction is localized on the two outermost layers at $\overline{K}$ as compared to 69 % at $\overline{M}$. This shows that, because of symmetry, the state (a') hardly resonates with the nearby bulk states at $\overline{K}$ and that the corresponding delocalization of the wavefunction is rather insensitive to its position in energy as compared to the bulk continuum edge. This will be of some importance in our self-energy calculation which assumes that the LDA and quasiparticle wavefunctions are in good agreement.

The LDOS at $\overline{\Gamma}$ is given in Fig. 3.5(a) : the features in the LDOS for the center of the slab from -7 eV to -2 eV illustrate the finite size effects related to the slab geometry but the enhancement of some of these structures in the H layer LDOS indicates that surface resonances exist in this energy range as reported in previous calculations [71, 73, 74].

The LDA energies of the surface states at $\overline{K}$ and $\overline{M}$ are also reported in Table

3.1. As compared to experiment, LDA underbinds the occupied surface states. This is consistent with previous calculations [84] for other surfaces, but the effect is significantly larger in the present case. This is related to the very localized 1s hydrogen orbital forming the surface states in the present system: Fig. 3.4 shows that the wavefunctions of the bonding surface states are not centered in the middle of the H-Si bond but fall into the deep well created by the hydrogen nucleus. The discrepancy in the energy position between LDA and experiment for the state (a') at $\overline{M}$ and the state (b) at $\overline{K}$ is larger by a factor 2 to 3 as compared to that for surface states at the As-Si(111) surface [19]. This difference between the two systems can be partially understood by examining the atomic calculations. Fig. 3.6 shows the error in the LDA eigenvalue energy for the highest occupied state as compared to the experimental ionization energy. It is well known that the discrepancy is very large for all atoms [85]. This error, resulting from using LDA exchange-correlation potential as an approximation to the self-energy operator, is therefore large. In the case of surface state energies, we are interested in their relative position to bulk states. Thus the energy differences between substrate and adsorbate levels are important. The cancellation of error is much more favorable in the As-Si system than the H-Si system. These differences are quoted in Table 3.2. One can see that the discrepancy is worse for the energy difference H(1s)-Si(3s): this is relevant for the state (c) at $\overline{K}$.

In addition to not yielding the correct position of surface states relative to bulk states, LDA in the present case does not give the correct dispersion for the surface states. For example, for the surface band (a') between $\overline{M}$ and $\overline{K}$, while the experimental data do no show any dispersion, the LDA calculation gives a dispersion of 0.42 eV.

Quasiparticle results

Because spectroscopic measurements can be understood in terms of excitations between quasiparticle states of an interacting electron system, our quasiparticle self-energy approach yields results in much better agreement with photoemission data than LDA. In the present case, very large self-energy corrections to the position of the LDA surface states are found: the self-energy corrections for the state (a') at $\overline{M}$ and the state (b) at $\overline{K}$ are 2 to 3 times larger than those for the surface states at the As-Si(111) surface [19]. This can be understood from the important non-local and dynamical effects induced by the high degree of localization of the surface states in the H/Si system. For selected k-points of the surface Brillouin zone, our calculated quasiparticle energy levels are given in Fig. 3.3 by the open circles. The specific energy levels for the quasiparticle surface states at $\overline{K}$ and $\overline{M}$ are quoted in Table 3.1. The agreement between our quasiparticle theory and the recent ARPES experiment is excellent: the discrepancy is at most 0.17 eV for the higher binding energy surface state at $\overline{K}$. This is much smaller than the 0.79 eV discrepancy for this state as calculated within LDA.

As a consequence of the improvement in the overall position of the surface states, the self-energy approach yields also an impressive improvement in the dispersion of all the surface states. This again may be understood from the sensitivity of the self-energy operator to the localization of the surface states. We compare in Fig. 3.7 the exchange-correlation energies for different states of the band (a') between $\overline{K}$ and $\overline{M}$ as given by different approximations. The bare Fock exchange, the LDA and the GW exchange-correlation operators have very different k-dependent behavior. Recall that the surface state (a') is more localized at $\overline{M}$ than at $\overline{K}$. The LDA exchange-correlation operator is much less sensitive to localization than the self-energy operator Σ and thus underestimates by 0.3 eV the dispersion of the exchange-correlation energy for the band (a') between $\overline{K}$ and $\overline{M}$. As expected, the bare exchange operator, which neglects screening effects, overestimates the dispersion. In contrast to both the LDA and bare exchange approximation, the self-energy approach yields a dispersion which is in almost perfect agreement with ARPES data.

The self-energy operator is also more sensitive to wavefunction character as a consequence of its non-locality. The state (a') at $\overline{K}$, which differs from surrounding bulk states by its strong hydrogenic character at the surface H site, is successfully extracted from the bulk continuum by the self-energy approach. It is important to note that even in the tight-binding calculation which locates the surface state (a') at $\overline{K}$ well within a pocket, the wavefunction at $\overline{K}$ is still much less localized than at $\overline{M}$. This shows that the wavefunction (a') at $\overline{K}$ does not change when extracted from the bulk continuum and the use of the LDA wavefunction to describe the quasiparticle wavefunction for this state is valid.

The small discrepancy between theory and experiment for the surface states at higher binding energy near $\overline{K}$ could be due to several effects. First, because the static part of the dielectric function is calculated exactly within the RPA, we expect the generalized plasmon pole model used to extend the dielectric function to finite frequency to be more accurate in the low energy range. Therefore, the self-energy of the smaller binding energy states are the most accurate within our scheme. Second, we neglect the influence of finite lifetime effects on the position of the quasiparticle energies. Since states closer to the gap edges have a larger lifetime, we expect these effects to be more important for states at higher binding energy. We emphasize that these discrepancies are small: the discrepancy is within the combined uncertainties of GW theory and experiment.

3.4 Conclusion

We calculated within the GW approximation the quasiparticle energies for occupied surface states of the H-Si(111)1×1 surface. This approach yields quasiparticle energies in excellent agreement with a recent high-resolution angle resolved photoemission spectroscopy performed on the "ideally" prepared surface. The ability of our first-principles quasiparticle approach to describe the dynamical and non-local effects in this highly anisotropic system, exhibiting very localized states on the Si-H bond, has been exemplified. Our LDA calculations also confirm that LDA combined with a slab model can accurately describes the ground-state properties of such surfaces and that the LDA wavefunctions are an excellent starting point for quasiparticle calculations in the Hybertsen-Louie formulation within the GW approximation.

Table 3.1: Energies of surface states at $\overline{K}$ and $\overline{M}$ (in eV with zero at the top of the valence band) for the H/Si(111)-(1×1) surface.

k-point	Tight Binding	Present calculations			Exp.
	(Ref. [73])	TB	LDA	GW	(Ref. [67])
$\overline{K}$	-3.88	-3.82	-3.22	-3.82	-3.80
	-5.02	-4.94	-4.29	-4.76	-4.78
	-8.83	-8.94	-7.85	-8.47	-8.64
$\overline{M}$	-4.94	-4.86	-3.87	-4.63	-4.76

Table 3.2: Energy difference between selected LDA atomic levels for Si, As and H as compared to experiment. The energies are given in eV.

	H(1s)-Si(3p)	As(4p)-Si(3p)	H(1s)-Si(3s)	As(4p)-Si(3s)
LDA	-2.17	-1.2	4.48	5.46
Exp.	-5.45[a]	-1.6[a]	-0.14[a]	3.65[b]

Upper indices (a) and (b) refer to Ref. [86] and Ref. [87].

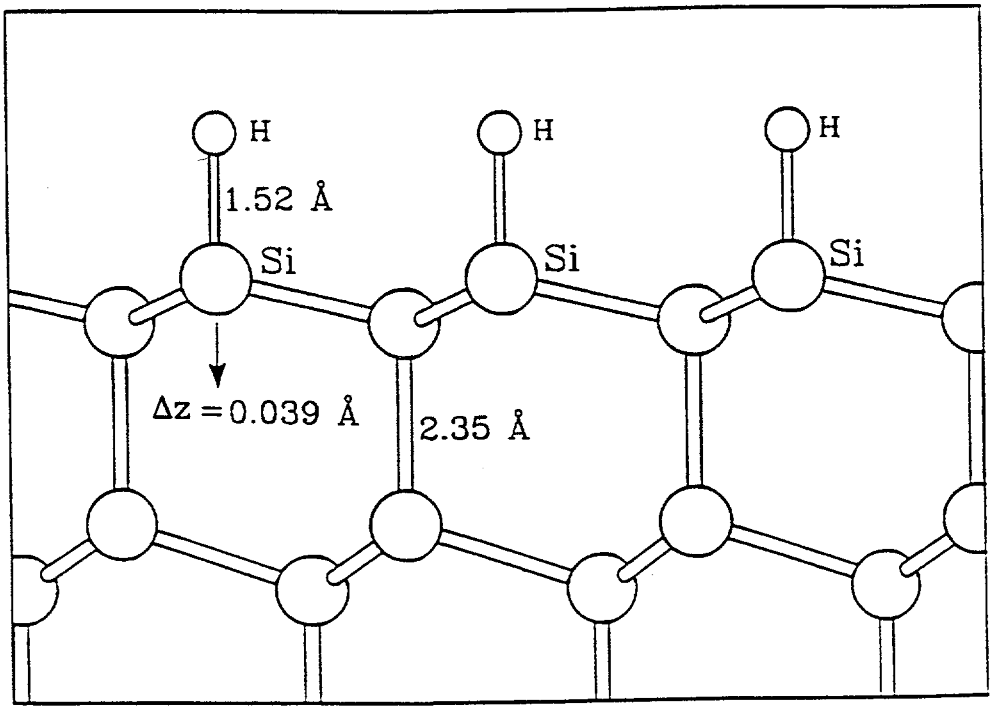

Figure 3.1: Schematic view of the H/Si(111)-(1×1) surface. The equilibrium distances as calculates within LDA are given in Å. Δz indicates the magnitude of the inward relaxation of the first Si layer.

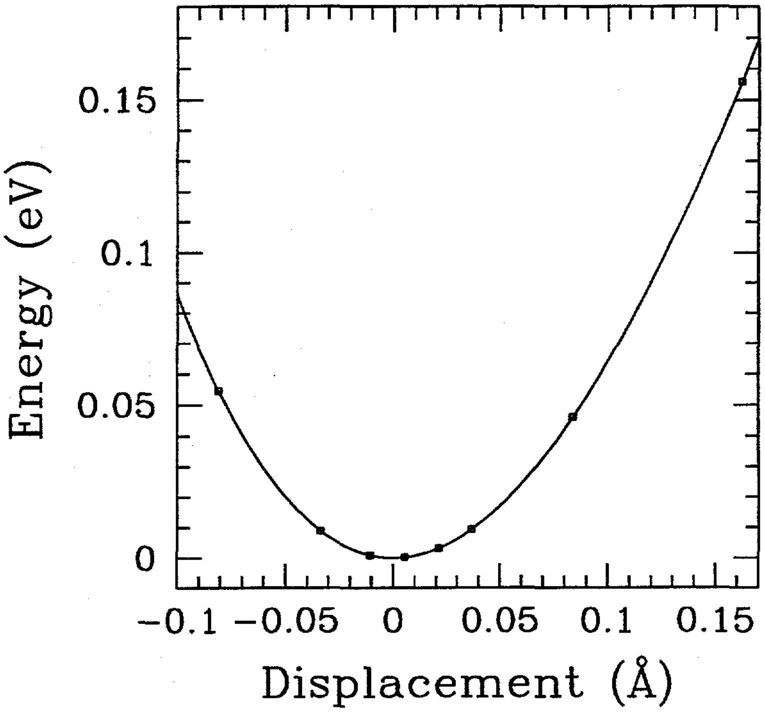

Figure 3.2: Calculated potential well of H-Si bond as a function of the displacement from equilibrium bond length. The open squares are the calculated points and the solid line is a fourth order polynomial least-square fit.

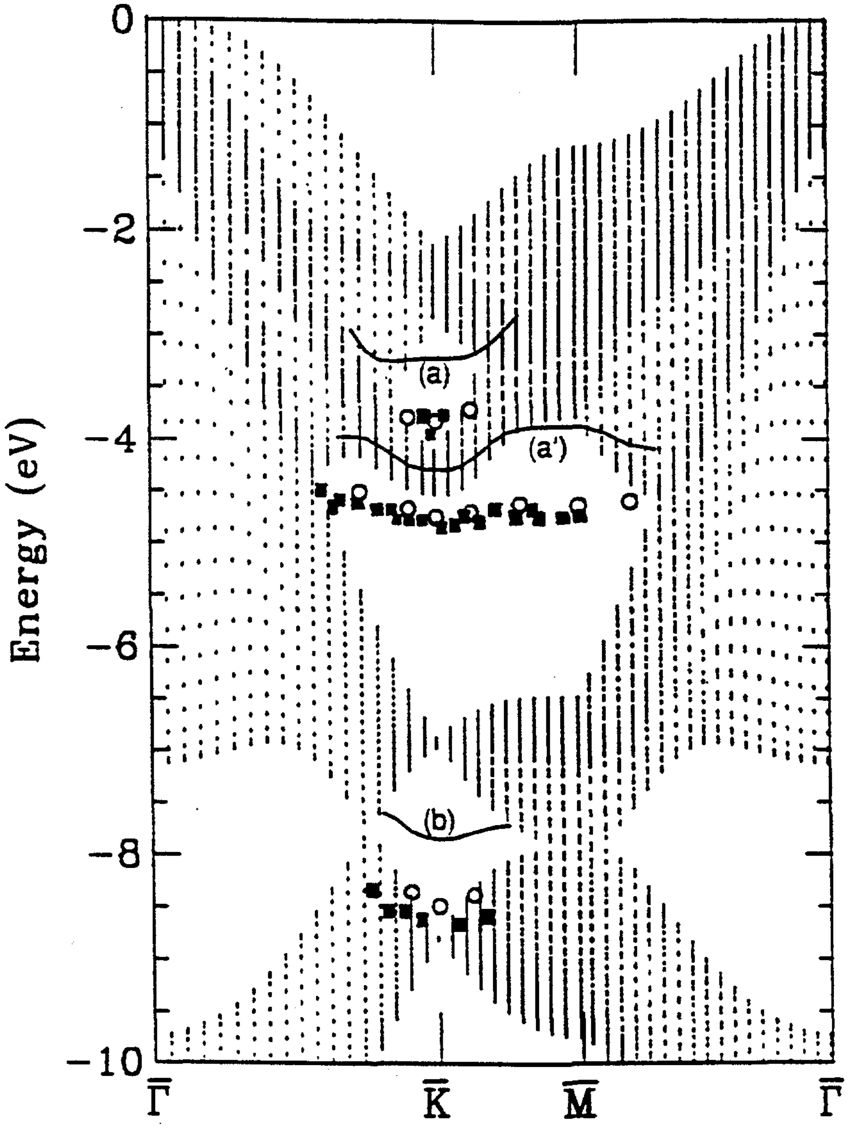

Figure 3.3: Surface state bands calculated within LDA (full lines) and GW (open circles). The black squares represent the experimental data. In the background is the projected Si bulk GW band structure. The zero of the energy scale is at the top of the valence band.

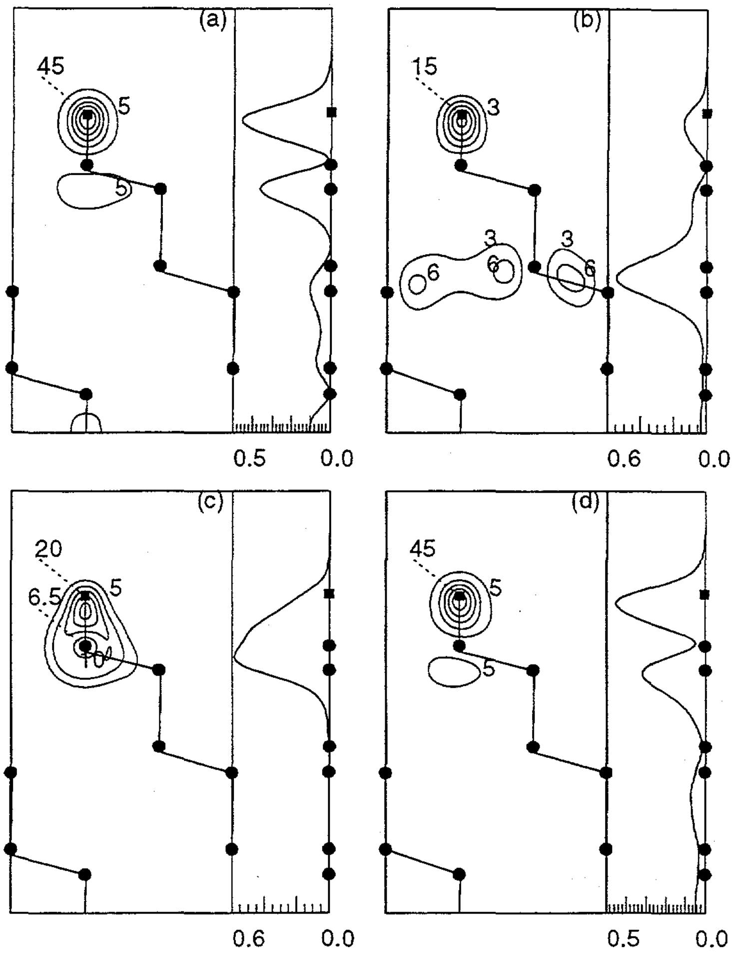

Figure 3.4: Contour plot in the [110] plane of selected surface-state wavefunctions and corresponding xy-averaged charge density plotted along the surface normal direction z. The values which label the contours correspond to $(2\pi)^3|\psi|^2$ where ψ is the corresponding wavefunction normalized such that $\int_{\Omega_c} dV\ |\psi|^2 = 1$, with Ω_c the unit cell volume. The xy-average charge density is normalized to unity within one unit cell. (a), (b), (c) and (d) correspond respectively to the LDA calculated states at -3.22 eV, -4.29 eV, -7.85 eV at $\overline{K}$ and the state at -3.87 eV at $\overline{M}$. The wavefunctions are plotted from the middle of the slab to the middle of the vacuum. The dots represent the silicon atoms contained in the [110] plane and the squares represent the hydrogen atoms. The dashed lines point to the charge density on the hydrogen or silicon atom.

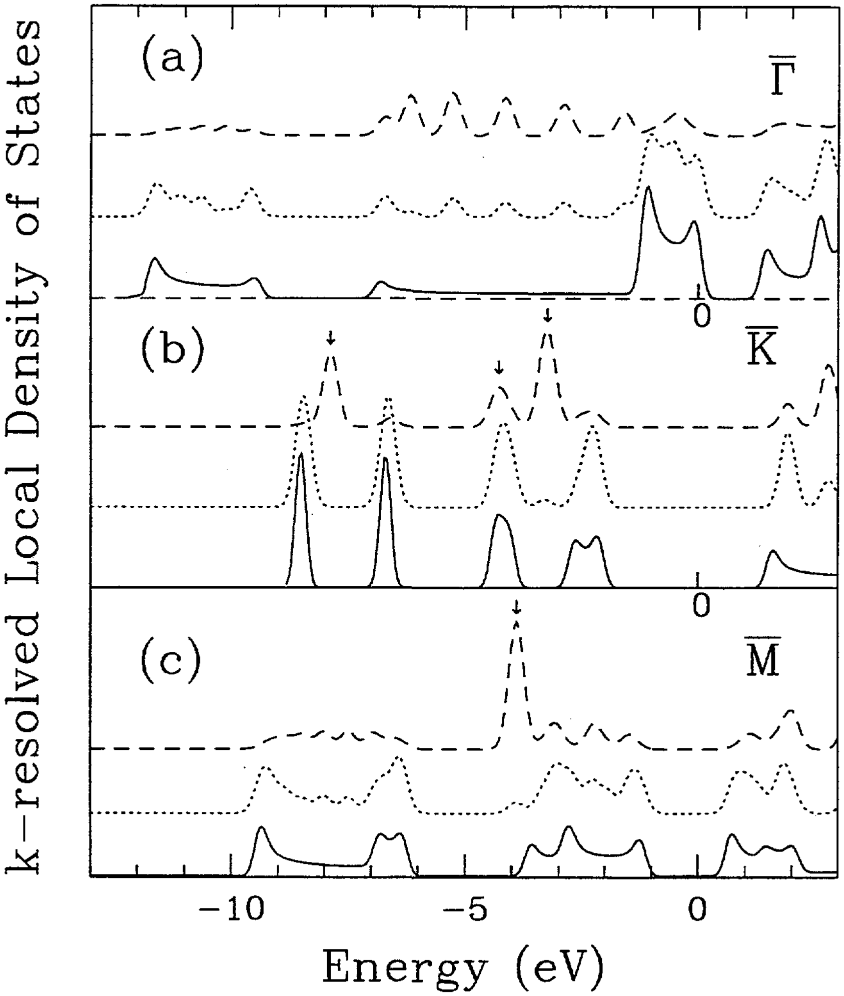

Figure 3.5: k-resolved LDOS for selected $\bar{k}$-points as calculated in the LDA. The solid line correspond to the bulk DOS. The upper long-dash line corresponds to the H-layer LDOS and the middle short- dash line to the "center of the slab" LDOS (innermost 4 Si layers included). The arrows indicate the position of the surface states as given by the LDA eigenvalues.

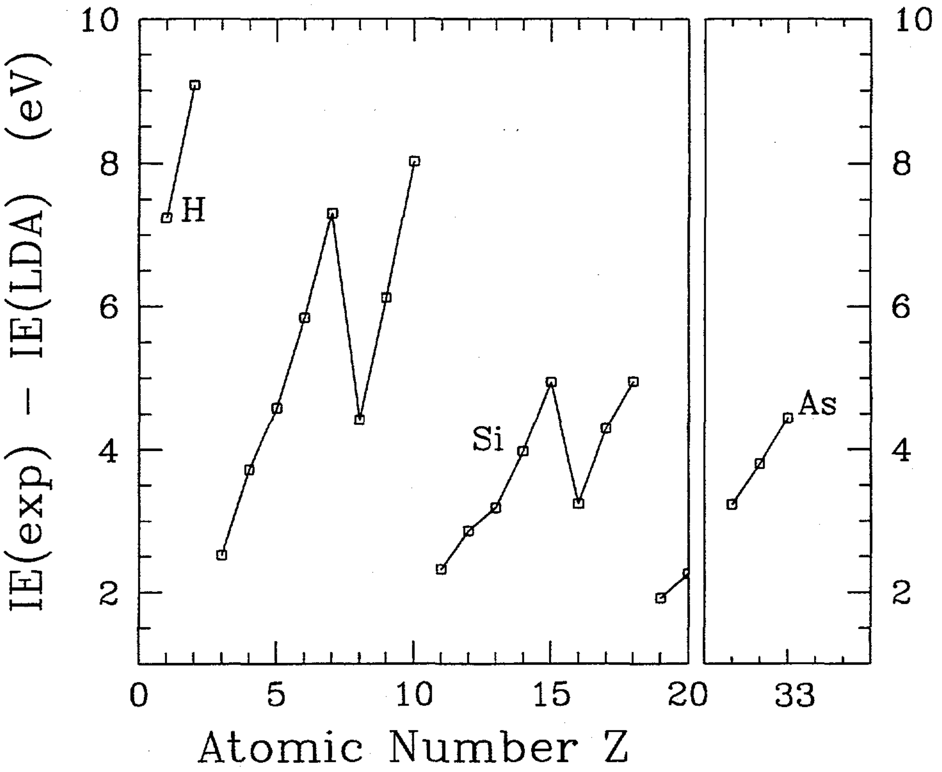

Figure 3.6: Difference between the LDA highest occupied state eigenvalue and the experimental ionization energy (in eV) for selected elements of the Periodic Table.

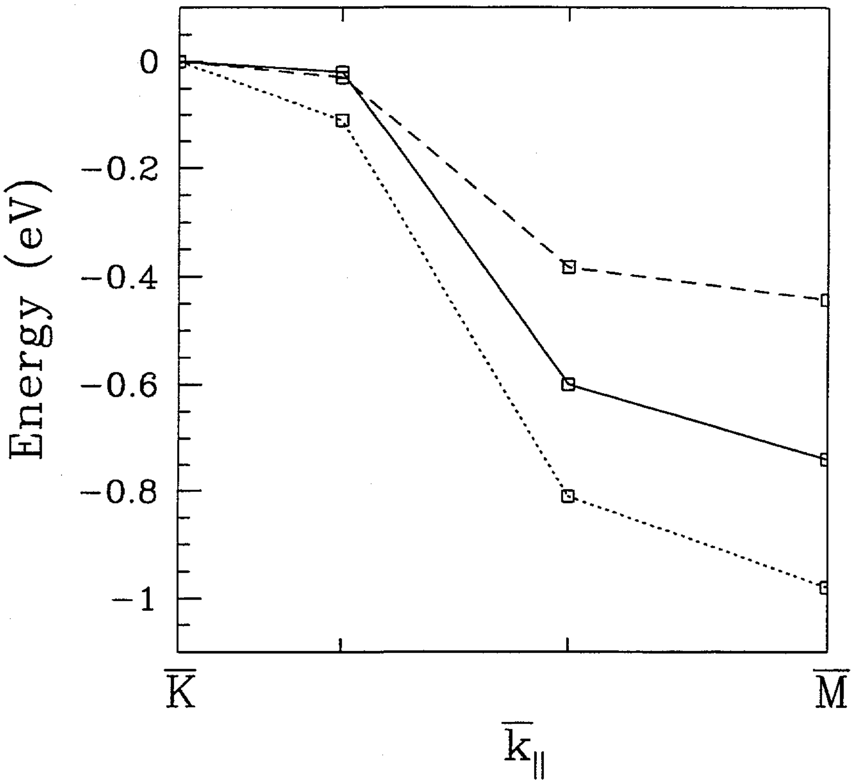

Figure 3.7: Energy dispersion for different approximations to the exchange-correlation operators for the surface-state band (a') at selected points between $\overline{K}$ and $\overline{M}$. The zero of energy scale is taken at $\overline{K}$. The solid line corresponds to the GW self-energy Σ operator, the dashed line to the LDA operator and the dotted line to the bare Hartree-Fock operator. The empty squares are the points where the energies have been calculated (in eV).

Chapter 4

Si 2*p* core level chemical shifts at the H/Si(111)-(1×1) surface

4.1 Introduction

As discussed in the previous chapter, a recently developed method of chemically etching silicon in buffered HF solutions allows the preparation of H-Si(111)-(1×1) surfaces with ideal H termination and high degree of homogeneity [63, 64]. The excellent quality of the surfaces obtained with this method, both with respect to the chemical purity and structural perfection, has been demonstrated by a variety of techniques [63, 64, 67]. The availability of such high quality surfaces has permitted very accurate experimental studies of the electronic structure of Si-H surfaces [67]. In particular the Si 2*p* core level spectra have been studied in great detail. Using surface sensitive spectra, this study was able to separate very clearly the bulk from the surface components of the Si 2*p* core level spectrum. Six lines were resolved within the Si $2p_{3/2}$ peak. Two of them were assigned to phonons, one to the bulk core level, and three to surface components. The three surface components however did not have a clear interpretation.

Motivated by experiment, we have carried out a first-principles calculation of the Si 2*p* core level shifts for Si atoms near the H/Si(111)-(1×1) surface. Pseudopotentials and a planewave basis are used to implement the local density approximation (LDA) of the density functional theory. All-electron calculations are in principle more desirable since they describe explicitly the core-valence interactions and core relaxation effects. However, pseudopotential calculations are easier to perform for large systems, and recently frozen-core-pseudopotential approaches have been used successfully to calculate core levels shifts [88, 89]. Following this line of work, we show in this Chapter that the use of a first-order perturbation theory to describe core-valence interaction in the framework of an *ab initio* pseudopotential approach gives good results for the Si 2*p* core level shift for the H/Si(111) surface. Contrary to methods based on total energy differences [89], our method can describe the splitting of a degenerate core level by the surface potential: this is of crucial importance in this work. In Ref. [88], a method similar to our approach has been proposed, but no experiment was available to demonstrate its validity. Here we show for the first time that this scheme gives excellent results when compared to experiment [67].

To describe the changes in the chemical environment at the surface as compared to the bulk, we must be able to describe accurately the modifications in both the ionic and electronic potentials. For the ionic potential, since the core regions do not overlap between neighboring atoms, the core electrons of each atom experience the tails of the real ionic potentials from neighboring atoms. We checked this by varying the extent of the pseudocore of both the H and Si atoms and no significant changes in the core level shifts were observed. More challenging is the description of the electronic potential felt by the core electrons. We find that the DFT-LDA formalism gives good results to describe such an interaction [90]. In the present scheme, we must in addition deal with the core-valence partitioning introduced by the pseudopotential technique. Since the core is frozen in the pseudopotential approach, core relaxation effects are not considered. Consequently, our calculations formally describe the escape of the core electrons in the sudden (or vertical) approximation and relaxation effects are neglected. Alternatively, the present theory corresponds to making the assumption that relaxation effects are similar for both surface and bulk atoms and that the core level shifts are mainly given by the potential changes. We agree with the conclusions of Ref. [89] that this might be a crude approximation in the case of surfaces with dangling bonds. However, consistently with Ref. [90], we show that in the present case of saturated surfaces, the present approximation gives good results.

4.2 Test of the method on the isolated atom core-level shifts

To study the validity of using perturbation theory, we look first at the isolated atom and study the shift in energy of the Si $2p$ atomic core level under a change in occupation of the 3p shell. In our perturbative approach, the zeroth-order wave function is taken to be the LDA all-electron Si $2p$ core level Ψ^0_{2p} of the atom in its ground state configuration. Results are reported in Table 4.1. We calculated the matrix elements $< \Psi^0_{2p}|V^{ps}_{HXC}|\Psi^0_{2p} >$ in various valence configurations of the atom. V^{ps}_{HXC} is the Hartree, exchange and correlation potential created by the valence electrons in the pseudopotential calculations. The shift of these matrix elements going from the ground state configuration to an excited-state configuration is compared to the shift ΔE^{ae} of the all-electron Si $2p$ eigenvalue under the same chemical change. Values for $< \psi_{2p}|\Delta V^{hxc}_{ae}|\psi_{2p} >$ and $< \psi_{2p}|\Delta V^{hxc}_{ps}|\psi_{2p} >$ are also reported. ψ_{2p} is the all electron Si $2p$ wavefunction for the given configuration (that is we allow the wavefunction to relax from Ψ^0_{2p} under the valence configuration change) and V^{hxc}_{ae} the all-electron LDA electronic potential. Δ indicates the changes between the studied configuration and the ground state configuration used as a reference. We looked at excited configuration with charge transfer comparable to or larger than the one expected in the solid, including ionic configurations. The agreement between the all-electron and pseudopotential calculations is very good, with largest error of about 9 % in the extreme case of complete ionization of the valence shell. This shows that the relaxation of the Si $2p$ wavefunctions is very small, that the change in the electronic potential created by the valence electrons only is responsible for virtually all the effect and that this change is well described in the pseudopotential approach.

4.3 Core-level shifts in the crystal

We turn now to the calculation of the core level shifts at the surface. Since the crystal potential is not spherically symmetric, we consider as zeroth-order wave functions the set of 6-fold degenerate spin-orbitals associated with the $2p$ atomic level in the (H_0, L^2, L_z) representation, where H_0 is the atomic potential in the absence of spin-orbit splitting and L the angular momentum operator. The angular part of the wavefunctions is written with usual notation: $\Psi_{2p}^{m}(\vec{r}) = R_{2p}(r) \times Y_1^m(\Omega_{\vec{r}})$ with m taking the values $-1, 0, 1$. The perturbation Hamiltonian contains the spin-orbit term $-\lambda \vec{L} \cdot \vec{S}$, where $\vec{S}$ is the spin momentum operator, and the crystal field potential $V(\vec{r})$. The strength of the spin-orbit coupling λ is taken to reproduce the experimental [67] splitting between the $2p_{1/2}$ and $2p_{3/2}$ levels in the crystal, and has the value $\lambda = 410$ meV.

The electronic part of the crystal potential is the same as that calculated in Chapter 3. To model the surface, we performed a supercell calculation with each supercell containing a 12-layer Si slab terminated by hydrogen saturating the dangling bonds on each side. The potential was expanded in a planewave basis with a kinetic energy cut-off $E_{max} = 20$ Ry. In the present work, we increase the ionic potential cut-off up to 56 Ry. For cut-offs smaller than 25 Ry, we find that the fluctuations of the ionic potential contribution to the core level shift as a function of E_{max} is of the same order of magnitude as the final result. We find that the short range non-local part of the ionic potential has no contribution to the core level shift.

We calculate first the matrix elements $V_{m',m}$ of the crystal potential in the (H_0, L^2, L_z) representation. We write then:

$$V_{m',m}(\vec{\tau}) = \int d^3\vec{r}\,(-1)^{m'}\Psi_{2p}^{-m'}(\vec{r}-\vec{\tau})\;V(\vec{r})\;\Psi_{2p}^{m}(\vec{r}-\vec{\tau})\;, \tag{4.1}$$

where $\vec{\tau}$ indicates the position of a Si atom in the supercell. $V(\vec{r})$ is the sum of the ionic and electronic potentials. Since we deal only with local potentials, it is convenient to work in Fourier space. Using the expansion of planewaves in terms of spherical harmonics, we get a multipole expansion of the potential and we may write:

$$V_{m',m}(\vec{\tau}) = \sum_{(L)} V^{(L)}_{m,m'}(\vec{\tau}), \tag{4.2}$$

with

$$V^{(L)}_{m',m}(\vec{\tau}) = 4\pi i^L \times$$
$$\textstyle\sum_{\vec{G}} V(\vec{G}) e^{i\vec{G}\cdot\vec{\tau}} \ \int r^2 dr j_L(Gr) R^2_{2p}(r) \ \sum_M [Y^M_L(\Omega_{\vec{G}})]^* \ \langle 1m' \mid Y^M_L(\Omega_{\vec{r}}) \mid 1m\rangle, \tag{4.3}$$

where $\mid 1m\rangle$ is the spherical harmonic $Y^m_1(\Omega_{\vec{r}})$ and j_L the spherical Bessel function of order L.

The selection rules for the angular integrals restrict terms of the sum in Eq. (4.2) to L=0,2. This implies that only two radial integrals need to be calculated numerically for each star of $\vec{G}$ vectors. Independent of the symmetry of the Hamiltonian, Eq. (4.3) yields the following set of relations:

$$V^{(0)}_{m',m}(\vec{\tau}) = V^{(0)}(\vec{\tau})\delta_{m,m'} \tag{4.4}$$

$$V^{(2)}_{1,1}(\vec{\tau}) = V^{(2)}_{-1,-1}(\vec{\tau}) = -\frac{1}{2} V^{(2)}_{0,0}(\vec{\tau}) \tag{4.5}$$

and in the case of a C_{3v} site-symmetry:

$$V^{(2)}_{1,0}(\vec{\tau}) = V^{(2)}_{-1,0}(\vec{\tau}) = V^{(2)}_{-1,1}(\vec{\tau}) = 0 \tag{4.6}$$

Eq. (4.4) indicates that the matrix $V^{(0)}_{m',m}(\vec{\tau})$ yields a rigid shift of the core level but does not induce any splitting of this level. On the other hand, the quadrupolar contribution (L=2) can in general couple different m and m' sublevels. However, in our geometry, these terms also must be zero because of the C_{3v} site-symmetry. Therefore, the matrix $V^{(2)}_{m',m}(\vec{\tau})$ is diagonal and, following Eqs. (4.5), only one matrix element needs to be calculated. Further, if we now consider the T_d symmetry of bulk silicon, $V^{(2)}_{0,0}$ and $V^{(2)}_{1,1}$ must be equal and therefore zero to satisfy Eqs. (4.5). This is also confirmed numerically in our calculations. We report in Table 4.2 the evolution of $V^{(0)}$ and $V^{(2)} = V^{(2)}_{0,0}$ for different values of $\vec{r}$. At the surface, $V^{(2)}$ is large and is responsible for the splitting of the core level (see below). As we go from the surface to the bulk, this matrix element decreases rapidly. This is an effect of the rearrangement of the charge density at the surface in order to screen the surface potential and restore the T_d symmetry of bulk silicon. For the innermost silicon atom, we find that $V^{(2)}(\vec{r}) = -1.5$ meV ; as expected, the crystal field splitting on this atom is negligible.

To diagonalize the perturbation Hamiltonian containing both the crystal field potential $V(\vec{r})$ and the spin orbit interaction $-\lambda\vec{L}\cdot\vec{S}$, we express first the matrix $V_{m',m}$ in the (H_0, L^2, J^2, J_z) representation where $\vec{J} = \vec{L} + \vec{S}$ is the sum of the angular momentum and electronic spin. In this basis set, the spin-orbit matrix is diagonal and yields the 2 levels $2p_{1/2}$ and $2p_{3/2}$, with degeneracy 2 and 4, respectively. Using Table 4.2 and taking as reference of energy the $2p_{3/2}$ energy level on the innermost silicon atom of our slab, we find that the $2p_{3/2}$ core level of a silicon atom at the surface is split into two peaks T_1 and T_2 at positions $E(T_1) = -40$ meV and $E(T_2) = -114$ meV on the higher binding energy side of the bulk core level (we neglect the -1.5 meV splitting of the "bulk" $2p_{3/2}$ core level). In terms of group theory analysis, this splitting can be explained by looking at the dimension of the irreducible representations compatible with the Si 2p orbital symmetry for respectively the bulk $\mathrm{T}_d^{'}$ and the surface $\mathrm{C}_{3v}^{'}$ double groups. The subsurface silicon atom $2p_{3/2}$ level (T_3) is shifted to $E(T_3) = 116$ meV at lower binding energy but its splitting is negligible as compared to the resolution of the experiment [67]. For the Si $2p_{1/2}$ core level, the surface potential gives rise to just two peaks, one at -83 meV and the other at 116 meV relative to the $2p_{1/2}$ bulk level. These peaks are associated respectively with the surface and subsurface Si atoms. No splitting is expected according to group theory analysis.

In addition to the position of the peaks, it is important to estimate their height in order to compare theoretical results to experimental results. Group theory analysis predicts that T_1, T_2 and the Si $2p_{1/2}$ surface level are all two fold degenerate. Therefore, the relative heights of these peaks should be given by the ratios of the corresponding electric dipole matrix elements. We calculated the matrix elements: $< e^{i\vec{K}\vec{r}}|X_\alpha|\Psi_{2p}^m >$ where X_α is x,y or z according to the polarization of the light source. This is consistent with the sudden approximation and the final state is chosen to be a planewave. Using these, we can estimate the relative intensities of the peaks T_1, T_2 and $2p_{1/2}$ for the surface atom, as well as the ratio of the $2p_{3/2}$ to the $2p_{1/2}$ peaks for the subsurface and bulk atoms.

With this set of theoretical values, a new fit for the data of Ref. [67] has been performed [91]. We present in Fig. 4.1 two of these fits. Both bulk and surface sensitive spectra are studied. The incoming light was polarized such that the electric field is parallel to the surface [92]. For this new set of fit, the 70 meV splitting between T_1 and T_2 has been respected. Because this splitting is dictated by the local properties of the potential at the surface (as shown in Table 4.2, this splitting is already negligible for atoms of the subsurface), it is insensitive to finite size effects induced by the slab model. Therefore, we believe that this value is well described in our calculation. For the same reason, the ratio of 0.4 for the relative height $I(T_1)/I(T_2)$ that we find in the case of an imposed parallel polarization. With these two constraints, the best fit yields surface and subsurface peaks in excellent agreement with our theoretical results aside from a rigid shift of -31 meV (allowing a ± 6 meV uncertainty on the experimental values). This rigid shift is related to the uncertainty on the position of the bulk peaks in our slab calculation. This kind of systematic error has been estimated to be 100 meV for a 8 layers Si slab [89] so that a rigid shift of 31 meV is reasonable for our larger 12-layer Si slab.

A comparison between theory and the fit values is presented in Table 4.3. In addition to the peak locations, we find that for the surface peaks, the ratios $I(2p_{1/2})/I(T_2)$ is calculated to be 0.79 in very good agreement with the experimental value of 0.71 [93]. For the subsurface and bulk peaks, the calculated ratios $I(2p_{1/2})/I(2p_{3/2})$ are 0.50 in both cases. We emphasize that the only constraint on the experimental fit is the shape of the $T_{1,2}$ peak as plotted in Fig. 4.1.

4.4 Conclusion

In conclusion, this work shows that the use of a first-order perturbation theory in the framework of a pseudopotential approach gives excellent results for the calculation of the core level shifts at the surface of a saturated system. We show that the surface Si $2p_{3/2}$ peak is split into two components by the surface crystal field. The present interpretation of the data of Ref. [67] gives a consistent description of the observed surface induced features: both peak positions and intensities are explained by the theoretical calculations. Experiment performed with different polarizations are suggested to further test the validity of our calculations. In particular, for the case of a polarization perpendicular to the surface, we predict the ratio $I(T_1)/I(T_2)$ to be close to 4.1 (instead of 0.4 in the present case). The peak $T_{1,2}$, which corresponds to the sum of the peaks T_1 and T_2, would then be displaced towards smaller binding energies [94].

Table 4.1: Core level shift for the Si $2p$ atomic core level under various valence shell configurations. The reference of energy is the all-electron ground state s^2p^2 configuration. The second column gives the core level shift from an all-electron calculation. The other columns give the results for various approximations. Energies are in eV.

	ΔE^{ae}	$< \Delta V_{ae}^{hxc} >_{\psi_{2p}}$	$< \Delta V_{ae}^{hxc} >_{\psi_{2p}^0}$	$< \Delta V_{ps}^{hxc} >_{\psi_{2p}^0}$
$s^2p^{1.5}d^{0.5}$	-0.2295	-0.2232	-0.2295	-0.2281
$s^{1.5}p^2d^{0.5}$	-0.2818	-0.2823	-0.2708	-0.2694
$s^2p^{1.5}$	-0.32627	-0.320766	-0.326275	-0.32546
$s^{1.5}p^2$	-0.38448	-0.37400	-0.384477	-0.37239
s^2p^1	-0.69999	-0.684577	-0.699979	-0.69540
s^2p^0	-1.571513	-1.520704	-1.571431	-1.547644
s^1p^0	-2.67917	-2.561516	-2.678618	-2.58616
s^0p^0	-3.76403	-3.56228	-3.76225	-3.42411

Table 4.2: Monopolar and quadrupolar contributions $V^{(0)}$ and $V^{(2)}$ to the crystal potential matrix elements for different silicon atoms $\vec{\tau}$. For the monopole contribution, only the difference from the value $V^0(\vec{0})$, where $\vec{0}$ is the innermost silicon of our slab, is given. The energies are in meV.

$\vec{\tau}$	$V^{(0)}(\vec{\tau}) - V^{(0)}(\vec{0})$	$V^{(2)}(\vec{\tau})$
surface silicon	-79	-70
subsurface silicon	116	2.8
second layer silicon	9	-0.5
innermost silicon	0	-1.5

Table 4.3: Theoretical and experimental values for the Si $2p$ core level shift. Shifts at the surface and subsurface for the Si $2p_{3/2}$ related peaks are given with respect to the bulk Si $2p_{3/2}$ level. The corresponding shifts for the Si $2p_{1/2}$ level are given with respect to the bulk Si $2p_{1/2}$ level. The theoretical values for the subsurface shifts are the same for both the Si $2p_{3/2}$ and Si $2p_{1/2}$ levels. The energies are in meV. The experimental values have a ± 5 meV uncertainty.

$\vec{\tau}$	This work	Exp.
surface Si $2p_{3/2}$	(-114,-44)	(-150,-80)
surface Si $2p_{1/2}$	-83	-120
subsurface silicon Si 2p	116	88

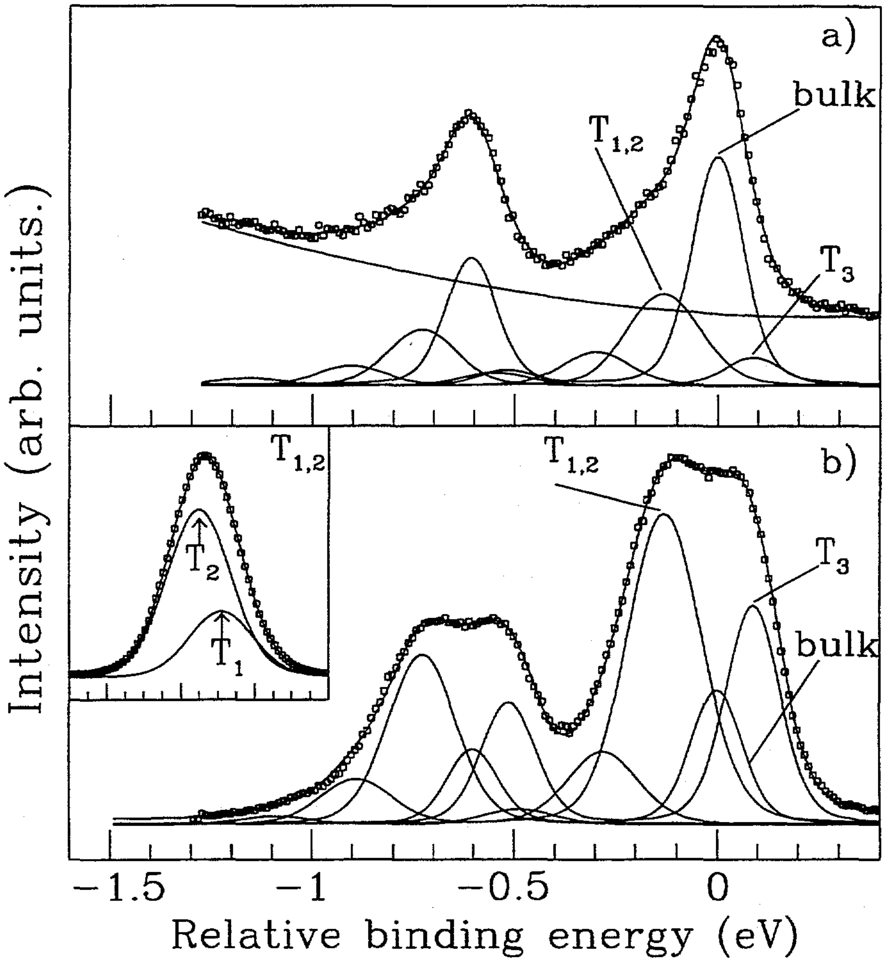

Figure 4.1: (a) Si_{2p} spectrum taken at hν=108 eV and normal emission to optimize the bulk component. The light is polarized in a direction parallel to the surface. The $T_{1,2}$ peak is the surface 2p$_{3/2}$ peak composed of the two components T_1 and T_2 as shown in the insert of (b). The peak designated by T_3 is the subsurface (or backbond) Si 2p$_{3/2}$ feature. (b) Surface sensitive Si$_{2p}$ spectra at hν= 130 eV. The light is polarized in a direction parallel to the surface.

Chapter 5

Quasiparticle band-structure of hexagonal BN

In this chapter, we study layered hexagonal BN structures. This work is carried out in conjunction with our study of the BN nanotubes. Compared to bulk semiconductor calculations, we are here confronted with the added complication of describing correctly the interactions between neighboring layers. These interactions are, in particular, responsible for the dispersion of the quasiparticle energy bands along directions perpendicular to the planes of atoms. In the case of bulk hexagonal BN, such dispersions can be as large as 2 eV. This is very large considering that two neighboring BN layers are 3.4 $\mathring{A}$ apart. Further, we find that these dispersions are nearly identical within LDA and GW. These two facts suggest that the layer-layer interactions in hexagonal BN are stronger than Van der Waals forces and are well described within LDA.

A striking feature of hexagonal BN from our calculations is the presence, at the bottom of the conduction bands, of an interlayer state with a charge density mostly localized in between two neighboring layers. When the BN layers are separated far from each other, this state evolves into a "single-layer" state of which the charge density has a maximum at 3.3 a.u. away from the plane of atoms. This state displays a nearly-free-electron-like character and, unlike other electronic states, the self-energy correction to LDA is negligible for this state. This state is the origin of the BN nanotubes nearly-free-electron-state described in section 2.3 of Chapter 2.

5.1 Introduction

Recently, using an analogy between carbon and BN-based materials, the existence of BN nanotubes has been suggested [14, 47]. Because these nanotubes can be viewed as being generated by rolling a sheet of hexagonal BN onto itself, this simple sheet structure has been the object of current interest [14, 95]. Further, it has been shown [14] that, in the case of multi-wall and single-wall BN nanotubes, the effect of intra- or inter-wall interactions on the electronic levels could be reproduced in a band-folding analysis by allowing the isolated BN sheet to interact appropriately with neighboring BN layers. In addition, the intrinsic properties of bulk BN motivate this study, since cubic BN is an extremely hard material [96] and displays the largest band gap of all III-V compounds. In this work, both bulk hexagonal BN and the isolated BN sheet are investigated. To our knowledge, this is the first quasiparticle calculation for bulk hexagonal boron nitride [97]. We also have examined intermediate structures composed of a periodic repetition of BN layers with an interlayer distance varying from $d = 5.5$ $\AA$ to $d = 13.5$ $\AA$ and analyzed the effect of the interlayer interaction on the band structures. We will use the notation, BN(d), for such hypothetical compounds.

As discussed before, because the density functional theory is a ground-state formalism, standard local density approximation (LDA) band structure calculations do not yield the true quasiparticle energy levels. In particular, it is well known that LDA underestimates the band gap of most semiconductors. In this Chapter, we show that LDA not only underestimates the gap of the structures under study, but also yields an incorrect ordering of the conduction bands in the case of the isolated BN sheet. In fact, for this system, the self-energy correction is strongly band- and **k**-dependent and therefore plays a more drastic role than one would expect from a simple "scissor" approach sometimes used to describe the results of self-energy corrections. As in the previous Chapters, the quasiparticle calculations are carried out using the Hybertsen-Louie method [2] which is based on Hedin's GW approximation [3] for the electron self-energy operator.

This Chapter is organized as follows. In section 5.2, the theoretical methods and technical details are discussed for the LDA and quasiparticle calculations. In section 5.3.1, the LDA band structures are given and the wavefunctions of the states controlling the band gaps are presented. In particular, it is shown that an interlayer free-electron-like-state forms the bottom of the conduction band in most structures. In the case of an isolated sheet, the interlayer state transforms into a state with a large extension into the vacuum, away from the plane of atoms. In section 5.3.2, the quasiparticle band structures are given, and the differences between the quasiparticle and the LDA results are discussed. Discrepancies with a previous quasiparticle band structure calculation performed on an isolated BN sheet [95] is analyzed. In section 5.4, a summary and conclusions are given.

5.2 Theoretical methods

We carry out *ab initio* pseudopotential LDA calculations, using a planewave expansion for the pseudopotentials and wavefunctions. The energy cut-off for the electronic wavefunctions is set at E_{cut}= 36 Ry. Boron and nitrogen pseudopotentials are generated following the Troullier and Martins pseudopotential generation scheme [41]. The Ceperley-Alder exchange and correlation potential [77] is used. The B-N bond length is set to the experimental distance of 1.45 $\AA$. The distance between two layers is chosen to be 3.34 $\AA$ for bulk hexagonal BN. For this structure, AB stacking with each B atom on top of a N atom is imposed in each unit cell. A 4x4x2 grid in the Monkhorst and Pack scheme [78] is used to generate 20 points in the irreducible Brillouin zone (BZ). The conventional notation for the hexagonal BZ are reproduced in Fig. 5.1. Among these 20 irreducible k-points, 10 are located in the ΓMK area and 10 in the ALH area.

For BN(d) structures, we choose an AA stacking with identical atoms on top of each other. This permits us to reduce the size of the unit cell by a factor two as compared to the stacking in bulk hexagonal BN, and the results make no difference in the limit of the isolated sheet. Both the isolated sheet and the intermediate BN(d) structures have the D_{6h} symmetry, while bulk hexagonal BN transforms according to the symmetries of the smaller C_{6h} group. The inter-layer distance is varied between d = 5.5 $\AA$ and d = 13.5 $\AA$ until stabilization of the electronic energy levels is achieved. We then obtain the band structure of an isolated BN sheet within this supercell approach.

The quasiparticle calculations are carried out using the scheme presented in section 3.2.2 of Chapter 3. The dielectric matrix is truncated at $|\mathbf{q}+\mathbf{G}| = 3$ a.u. This is sufficient to describe the local-field effects in the present cases. The **k**-point sampling used for the BZ summations involved in the calculation of both the dielectric matrix and the self-energy matrix elements is the same as those used in the LDA calculations. We include 40 bands per atom in the unit cell to perform the summation over the conduction bands for the calculation of the RPA independent-particle polarizability. The same number of bands is used to calculate the electron Green's function. Finally, a cut-off of $|\mathbf{q}+\mathbf{G}| = 4$ a.u. is used to converge the bare-exchange contribution to the self-energy. Coulomb-hole and screened-exchange terms converge faster, and we set $|\mathbf{q}+\mathbf{G}| \leq 3$ a.u. for these calculations. This set of convergency parameters gives quasiparticle energies converged to within 0.1 eV.

5.3 Results

5.3.1 LDA calculations

In Fig. 5.2, the LDA band-structure for bulk hexagonal boron-nitride is plotted along high symmetry directions of the BZ . The energy levels at high-symmetry points are reported in Table 5.1. Because of layer-layer interactions, the dispersion along the c-axis is non-negligible as can be seen from the band structure along the ΓA, ML and KH directions. Within LDA, we find that bulk hexagonal BN is a large gap semiconductor, with an indirect gap of 3.9 eV between the top of the valence band near K and the bottom of the conduction band at M. The top of the valence band, located near K along KΓ (we will use the notation T_1 for this point), is very close in energy to the highest occupied (HO) state at H (within room temperature in our calculations). The direct gap at Γ is found to be 5.95 eV. Both the indirect band gap and the direct gap at Γ are smaller than in cubic BN [98]. The direct band gap at Γ is most sensitive to the structure. It changes by 2.65 eV between the cubic and hexagonal structure (As discussed below, this is due to the "interlayer" nature of the conduction band minimum in the case of the hexagonal structure). We note that for AlN and GaN compounds [99], the direct gap at Γ differs by at most 0.3 eV between the cubic and the wurtzite structure (both exhibit sp^3 hybridization). By analogy, we conclude that the indirect gap at Γ must be also smaller by at least 2 eV for hexagonal BN as compared to wurtzite BN. This should help to identify the structurality of tubular BN in its recently predicted novel forms [34]. In Fig. 5.3(a),(b) and (c), electron densities are given for the bottom of the conduction band at M and the HO state at K and H, respectively. For the lowest unoccupied (LU) state at M, the charge density is localized on the boron atoms while for the HO state at K and H, the charge density is localized on the nitrogen atoms. All of these states display a π or $\pi^\star$-like character. We note the difference of charge localization for the HO state at K and H. A phonon-assisted optical transition from H to M would require phonons propagating along the c-axis. We expect these two features to help in the identification of the character of the states involved in either p-type doping or optical experiments.

We study also the LU state at Γ. The corresponding charge density is represented in Fig. 5.3(d). This state has most of its charge concentrated in the inter-layer region. The xy-average charge density plotted along the c-axis shows a strong maximum at the midpoint between the two neighboring BN layers. This state is the analog of the interlayer-state in graphite. The remaining charge on the BN planes is located mostly on the nitrogen atoms. This is in contrast to graphite where the on-plane charge for the inter-layer state is equally distributed on each carbon atom. The difference in ionicity between B and N explains this feature for hexagonal BN.

As intermediate structures between bulk hexagonal BN and an isolated sheet, we study the BN(d) "gedanken" compounds. We vary the inter-layer distance d from 5.5 $\AA$ to 13.5 $\AA$ (we note that d=3.4 $\AA$ is the bulk hexagonal interlayer distance). Stabilization of the band-structure is observed for d larger than 11.5 $\AA$. This is established by comparing with the band structure of the system with d=13.5 $\AA$. With the interlayer distance increasing from d=5.5 $\AA$ to larger values, the energy of the valence states and lowest unoccupied states hardly changes, except for the LU state at Γ which moves up in energy. This is not surprising since this state is the analogue of the inter-layer state in bulk hexagonal BN and has a very large extension into the interlayer region. We show in Fig. 5.4 the evolution of the charge density for this state for d=5.5, 9.5 and 13.5 $\AA$. As one can see, the corresponding wavefunctions from neighboring planes strongly overlap for d=5.5$\AA$ and d=9.5$\AA$. Only for d=13.5 $\AA$, this overlap begins to be negligible. In the case of d=13.5 $\AA$, we also plot the average potential along the c-axis. This potential is very flat in the middle of the inter-layer region, insuring that indeed the BN layers are not interacting. We list in Table 5.2 the energy of the band gap edge states at Γ, K and M. The eigenvalues stabilize for d $\geq$ 11.5 $\AA$. We check that for BN(d=13.5) there is no dispersion along the ΓA direction, which confirms that for such a layer-layer distance, two neighboring planes are not interacting. For d $\leq$ 6.5 $\AA$, the bottom of the conduction band is at Γ within LDA. For larger inter-layer distances (and therefore for the isolated sheet), it is at K. For all structures, the top of the valence bands is at M. The LDA band-structure for d=13.5 $\AA$ is presented in Fig. 5.5. Using our results for BN(d=13.5), we conclude that, within LDA, the isolated BN sheet is a 4.3 eV indirect gap semiconductor.

The lowest unoccupied level at Γ is a state which extends into the vacuum region with a maximum charge density at about 3.3 a.u. away from the plane of atoms. Such a state is difficult to understand in terms of B or N atomic orbitals. We note in Fig. 5.3(a),(b),(c) that the p_z-like orbitals associated with the BN sheet have a maximum charge density which is localized at most at 0.75 a.u. away from the atomic layer. Another important feature of the LU state at Γ is that its in-plane effective mass is calculated to be $m^\star = 0.95 \pm 0.05$ in units of the free electron mass (the value varies slightly along the different planar directions). Therefore, this state displays a nearly-free electron (NFE) like character, and an electron in this state would be mainly sensitive to the crystal potential averaged over the plane parallel to the BN layers. We denote this potential $V_{xy}(z)$, where z is the distance of the electron from the BN layer to which it is bound [100]. Following this idea, we solve the one-dimensional Schrödinger equation for an electron in the $V_{xy}(z)$ potential associated with an isolated BN sheet. Practically, we use the $V_{xy}(z)$ potential calculated for the BN(d=13.5) structure and set the vacuum level to the value of $V_{xy}(z)$ at 6.5 $\AA$ away from a given BN layer. We plot this potential in Fig. 5.6 together with the charge density for the bound state (n=0,1,2) solutions of this one-dimensional Schrödinger equation. The most important result is that the n=2 level (located -0.55 eV below the vacuum level) is very similar in shape to the charge density (represented in Fig. 5.4(c)) of the NFE state in BN(d=13.5). In particular, the n=2 level charge density has a maximum at around 4.1 a.u away from the BN layer. This is larger than the value of 3.3 a.u. that we find for the NFE-state but the qualitative agreement is satisfying, accounting for the simplicity of the model. Thus, our physical picture is that the NFE planar state is indeed the n=2 loosely bound state due to the attractive planar average potential of a BN sheet but slightly modified by the discrete atomic potentials. The n=0 and n=1 states are so tightly bound to the BN sheet that they are strongly modified by the crystal potential and become indistinguishable from states obtained within a tight-binding description. We believe that such NFE plane states could be a very general feature of isolated crystalline sheet.

5.3.2 Self-energy calculations

We have performed self-energy calculations for bulk hexagonal BN, BN(d=5.5), BN(d=7.5) and BN(d=13.5). As a first step, the static inverse dielectric matrix $\epsilon^{-1}_{GG'}(\mathbf{q})$ is calculated within the random phase approximation. From this calculation, the macroscopic dielectric constant can be extracted using the relation $\epsilon_M = \epsilon^{-1}_{00}(\mathbf{q} = 0)$. We find ϵ_M=4.9 for bulk BN and ϵ_M=3.3 for both BN(d=5.5) and BN(d=7.5). This can be compared to the value of $\epsilon_M = 4.5$ for cubic BN [97]. Using the Philips and van Vechten empirical relation (see formula (6) of Ref. [97]), one can see that the larger the average gap the smaller the macroscopic dielectric constant. Therefore, the ordering of the dielectric constants for these materials is consistent with the values for their respective gaps, since the band gap for cubic BN was calculated [98] to be 4.2 eV within LDA (which is larger than all LDA gaps calculated in the present work). However, owing to their different dimensionality, the plasmon energy for bulk BN structures and the isolated sheet may be significantly different and such an empirical relation cannot be straightforwardly used.

The quasiparticle band structure of bulk hexagonal BN is represented in Fig. 5.7. The main effect of the self-energy correction is to open the gap from 3.9 eV (LDA value) to 5.4 eV. Within GW, the calculated band gap is smaller for bulk hexagonal BN than for bulk cubic BN by 0.9 eV [97]. This is consistent with the closing of the gap going from diamond to graphite (in the case of BN, the ionicity gap prevents the occurrence of a semimetallic behavior). Quasiparticle eigenvalues are reported in Table 5.1 together with the LDA energies for high symmetry points. Because the self-energy is weakly k-dependent in this case, the GW band structure is very similar to the LDA band structure except for the band gap value. In particular, the gap remains indirect between the top of the valence band at T_1 near K and the bottom of the conduction band at M. We note that the self-energy correction for the HO state at H and K are nearly identical so that the LDA energy difference between the top of the valence band and the HO state at K is not changed by the self-energy correction and both states remain very close in energy.

For BN(d=5.5), the self-energy correction $\Delta E(E^{LDA}_{nk}) = E^{QP}_{nk} - E^{LDA}_{nk}$ is represented in Fig. 5.8. Contrarily to bulk hexagonal BN, the self-energy correction $\Delta E(E_{nk}^{LDA})$ is strongly **k**-dependent. In particular, the correction to the lowest-occupied state at Γ is negligible, while the self-energy correction for the LU state at K and M are both equal to 0.6 ± 0.1 eV. As a result, not only is the gap opened up in the quasiparticle approach but, in addition, the ordering of the lowest conduction bands is modified. In particular, the bottom of the conduction band is displaced from K to Γ by the quasiparticle treatment. Therefore, within GW, the gap is indirect between K and Γ. We note that, because the LU state at Γ displays a nearly-free-electron like character, it is not surprising that the LDA exchange-correlation potential and the self-energy operator yield the same expectation value for this state.

We performed the same self-energy calculation for BN(d=7.5). The self-energy corrections to the LDA eigenvalues are similar to those obtain for BN(d=5.5) within the accuracy of the method. This is presented in Table 5.3 for selected k-points. The stability of the quasiparticle corrections for $d \geq 5.5$ Å allows us to obtain the quasiparticle band structure of the isolated boron-nitride sheet. For this structure, we find the quasiparticle gap to be 6 eV and the conduction band minimum at Γ (see Fig. 5.9). The gap value is intermediate between the gap for bulk hexagonal and cubic BN (respectively 5.4 and 6.3 eV within GW). We note that layer-layer interaction increases the dispersion of the electronic bands and tends to reduce the gap. This effect can be used to understand the smaller gap of bulk hexagonal BN as compared to the isolated sheet [102].

We note that the present results show some discrepancies with a recent self-energy calculation [95] for an isolated BN sheet. The work in Ref. [95] was based on the Møller-Plesset perturbation theory, and STO-3G gaussian orbitals were used. The most important difference between the two sets of results is that the state predicted in the present work to be the bottom of the conduction band within GW (the NFE state at Γ) was reported to be 12.3 eV above the LU state at K in Ref.

[95]. This state is shown here to have a very large extension in the vacuum region. Such an extended state is easily described using a plane-wave basis. However, a localized basis such as STO-3G or a Slater-Koster type (3s,3p$_x$,3p$_y$,3p$_z$) basis [103] would have difficulty in reproducing the extension of such a wavefunction away from the atoms. A previous tight-binding (TB) calculation performed on bulk hexagonal BN [47] shows that the LU state at Γ is (within TB) located 10 eV above its "LDA-planewave basis" analogue (we aligned the bottom of the conduction band at K in both calculations). This is consistent with the results of Ref. [95] where the use of a limited localized basis underbinds the extended states.

5.4 Conclusion

We have calculated the quasiparticle band structure of the most common allotropic form of bulk BN which is hexagonal. The band gap is indirect and calculated to be 5.4 eV (that is 0.9 eV smaller than cubic BN). The isolated BN sheet has also been studied. The band gap of the sheet is calculated to be 6.0 eV. The bottom of the conduction band is a state with charge density which has a very large extent into the vacuum region. This feature makes its study difficult for theoretical methods based on the use of localized basis functions. The present results have been used to calculate the quasiparticle band-structure of BN nanotubes [14]. In particular, the LU state for these tube is found to be a nearly-free-electron state with charge density localized along the axis of the tubes. This free-electron-tubular state is derived from the "sheet" state of the isolated BN sheet when the planar structure is rolled into a tubular shape.

Table 5.1: Bulk hexagonal BN eigenvalues at high-symmetry points. The energies are in eV. The top of the valence band is taken to be the zero of energies for both LDA and GW results.

k-point	LDA	GW
Γ_{1v}	-17.94	-19.87
Γ_{3v}	-17.65	-19.57
Γ_{3v}	-6.33	-7.33
Γ_{1v}	-4.12	-4.80
Γ_{5v}	-1.45	-1.69
Γ_{6v}	-1.32	-1.57
Γ_{1c}	4.63	5.96
Γ_{3c}	10.06	12.61
K_{3v}	-14.14	-15.91
K_{1v}	-8.05	-9.01
K_{2v}	-7.89	-8.82
K_{3v}	-7.17	-8.45
K_{3v}	-0.14	-0.14
K_{3c}	4.50	6.19

Table 5.2: LDA band edge states energies at Γ, K and M for various BN interlayer distances d. The energies are in eV. The top of the valence band K_{3v} is taken to be the zero of energies.

	interlayer distance ($\AA$)				
state	5.5	7.5	9.5	11.5	13.5
Γ_{6v}	-1.43	-1.50	-1.57	-1.57	-1.57
Γ_{1c}	3.97	4.19	4.51	4.61	4.61
K_{3v}	0.00	0.00	0.00	0.00	0.00
K_{3c}	4.41	4.36	4.33	4.32	4.32
M_{3v}	-0.95	-0.97	-0.99	-0.99	-0.99
M_{1c}	4.57	4.49	4.45	4.43	4.43

Table 5.3: Selected energy levels at Γ, K and M for BN(d=5.5), BN(d=7.5) and BN(d=13.5) within LDA and GW. The energies are in eV. The top of the valence band is taken to be the zero of energies for both LDA and GW results.

d	d=5.5		d=7.5		d=13.5	
	LDA	GW	LDA	GW	LDA	GW
Γ_{1v}	-17.81	-19.74	-17.81	-19.75	-17.98	-19.92
Γ_{3v}	-5.31	-6.21	-5.32	-6.23	-5.40	-6.31
Γ_{5v}	-1.43	-1.64	-1.50	-1.61	-1.57	-1.68
Γ_{1c}	3.97	5.52	4.19	5.58	4.61	6.00
K_{3v}	-14.16	-15.82	-14.16	-15.84	-14.37	-16.05
K_{1v}	-7.98	-8.84	-7.99	-8.86	-8.21	-9.08
K_{2v}	-7.18	-8.37	-7.19	-8.40	-7.35	-8.56
K_{3v}	0.00	0.00	0.0	0.0	0.00	0.00
K_{3c}	4.41	6.45	4.36	6.46	4.27	6.37
K_{1c}	12.32	14.44	12.10	14.16	11.93	13.99
M_{1v}	-14.73	-16.42	-14.73	-16.05	-14.94	-16.26
M_{3v}	-8.92	-10.15	-8.91	-9.92	-9.10	-10.11
M_{1v}	-4.22	-4.72	-4.24	-4.73	-4.44	-4.93
M_{3v}	-0.95	-1.15	-0.97	-1.08	-0.96	-1.07
M_{1c}	4.57	6.65	4.49	6.39	4.43	6.33
M_{3c}	9.19	11.42	9.24	12.26	9.25	12.27

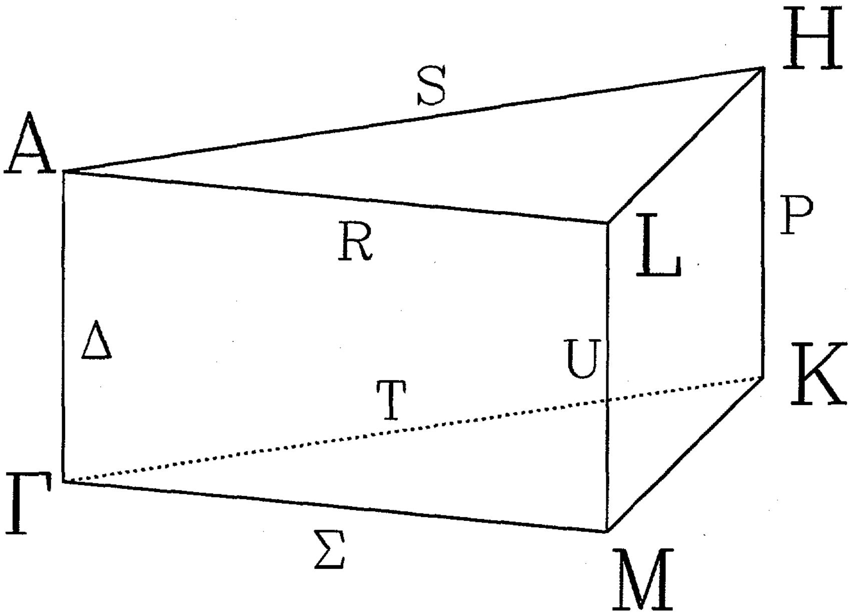

Figure 5.1: High symmetry points and directions are labeled for the irreducible part of the hexagonal Brillouin zone.

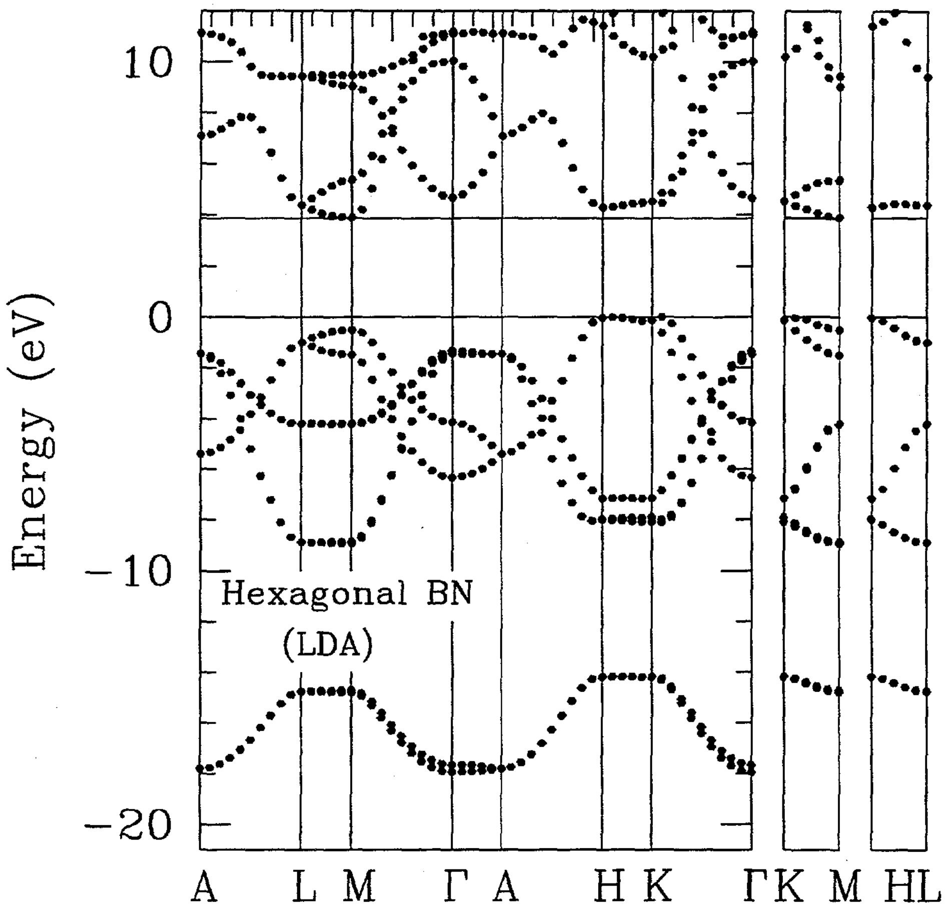

Figure 5.2: LDA band structure for bulk hexagonal boron nitride plotted along high symmetry directions of the BZ. The energies are in eV. The top of the valence band is taken to be the zero of energies. The edges of the gap are indicated by horizontal lines as a guide to the eyes.

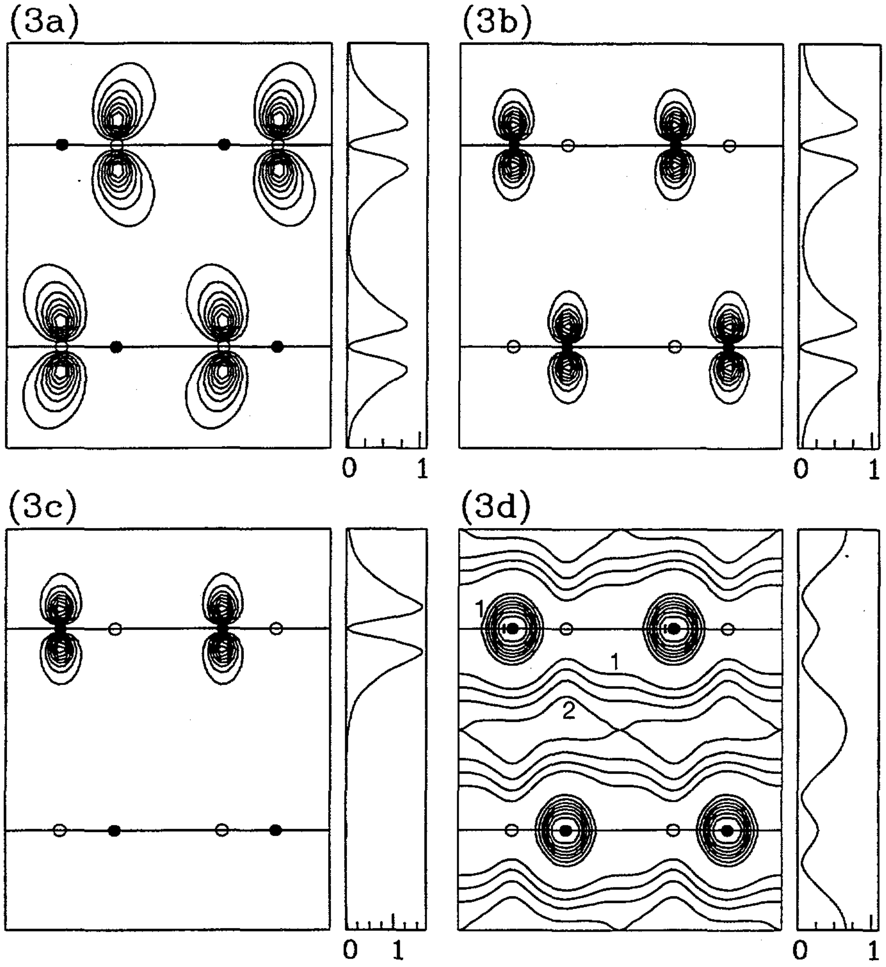

Figure 5.3: Contour plots in a plane perpendicular to the BN layers of the charge density of selected states for bulk hexagonal BN. BN layers are indicated by horizontal lines. N atoms are represented with filled circles and B atoms with empty circles. In addition, the charge density averaged over planes parallel to the BN layers is represented as a function of the distance perpendicular to the BN layers; this charge density is normalized to unity within one unit-cell. Figures (a), (b), (c) and (d) correspond respectively to the LUMO state at M, the HOMO state at K, the HOMO state at H and the LUMO state at Γ. In (d), contours labeled (1) and (2) correspond to a charge density of respectively 0.16×10^{-4} and 0.63×10^{-4} electron/$a.u.^3$. The maximum charge density is 1.26×10^{-4} electron/$a.u.^3$ on the nitrogen atoms.

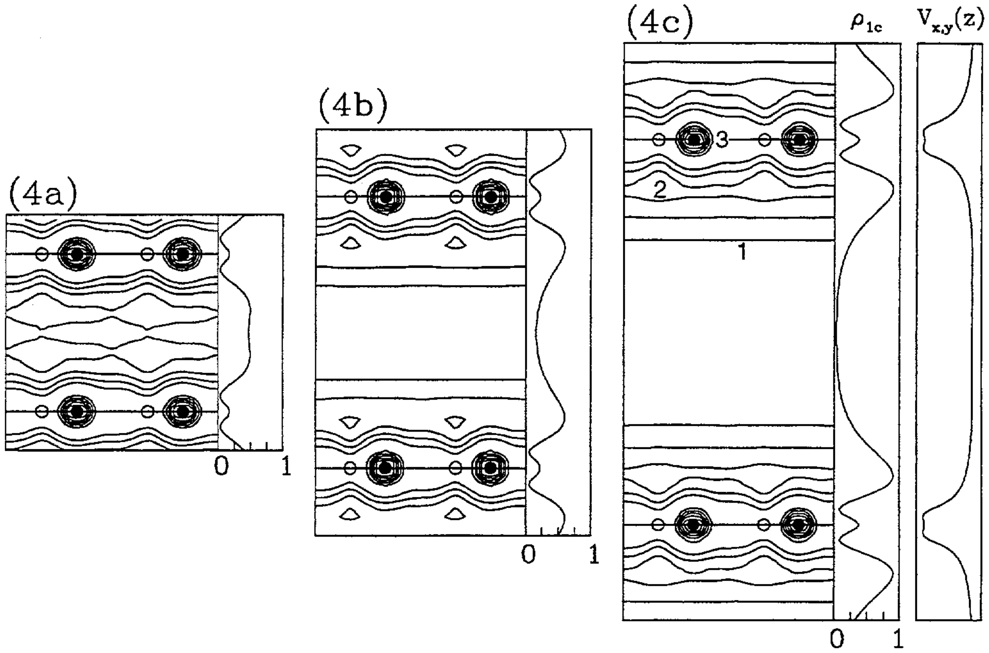

Figure 5.4: Contour plot in a plane perpendicular to the BN layers of the charge density of the LUMO state at Γ for (a) BN(d=5.5), (b) BN(d=9.5) and (c) BN(d=13.5). BN layers are indicated by horizontal lines. N atoms are represented with filled circles and B atoms with empty circles. In addition, the charge density averaged over planes parallel to the BN layers is represented as a function of the distance to the BN layers. This charge density is normalized to unity within one unit-cell. In (c), contours labeled (1), (2) and (3) correspond to a charge density of respectively 0.14×10^{-4}, 0.43×10^{-4} and 0.28×10^{-4} electron/$a.u.^3$. The maximum charge density is 0.85×10^{-4} electron/$a.u.^3$ on the nitrogen atoms. The total potential averaged over planes parallel to the BN layers ($V_{x,y}(z)$) is also represented. $V_{x,y}(z)$ varies from -2.05 Ry to the vacuum level (origin of energies).

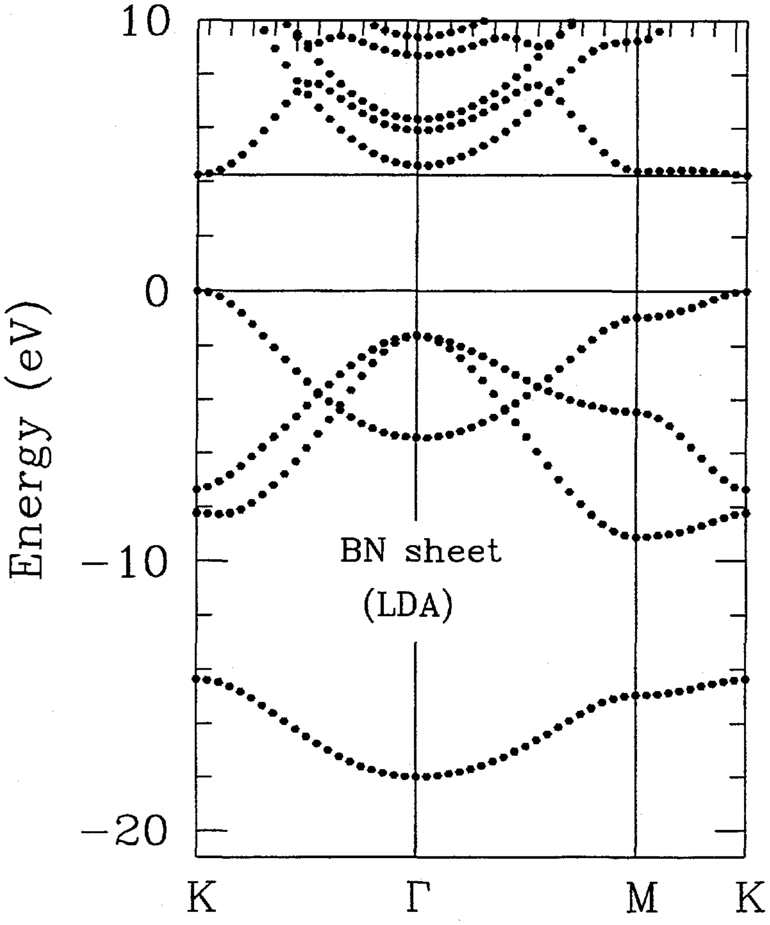

Figure 5.5: LDA band structure for an isolated BN sheet plotted along high symmetry directions of the BZ. The energies are in eV. The top of the valence band is taken to be the zero of energies. The edges of the gap are indicated by horizontal lines as a guide to the eyes.

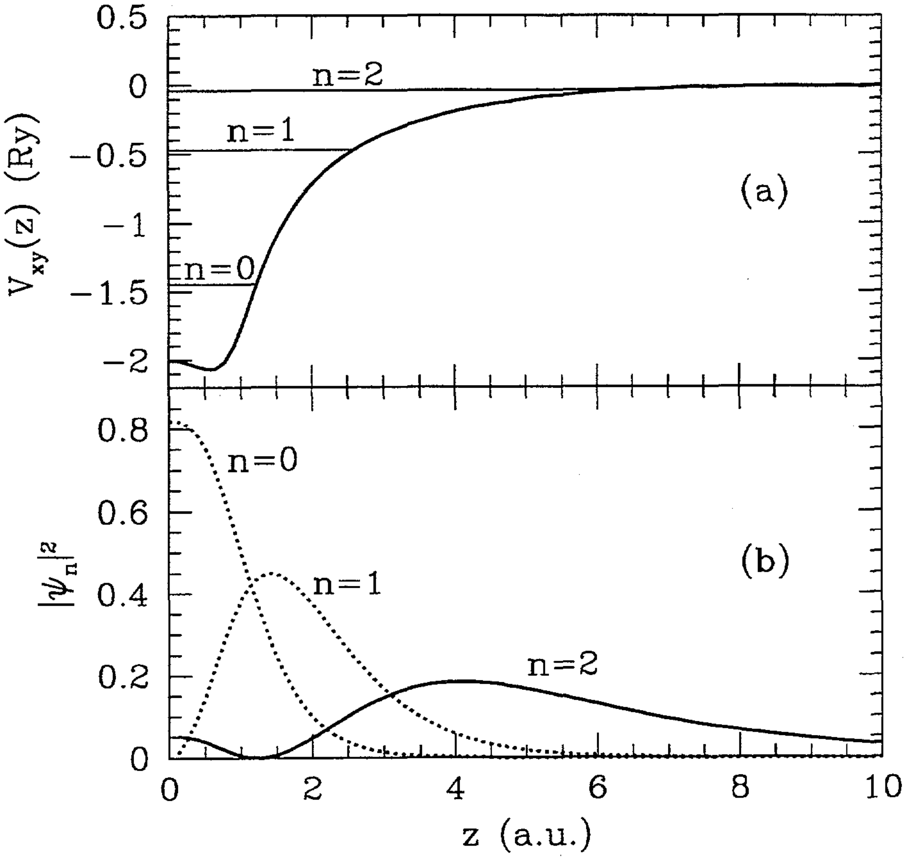

Figure 5.6: (a) $V_{x,y}(z)$ potential and (b) bound eigenstate charge densities are represented. The potential is in Rydberg and the distance in a.u. Positions of the eigenvalues with respect to the vacuum level are represented by horizontal line in (a).

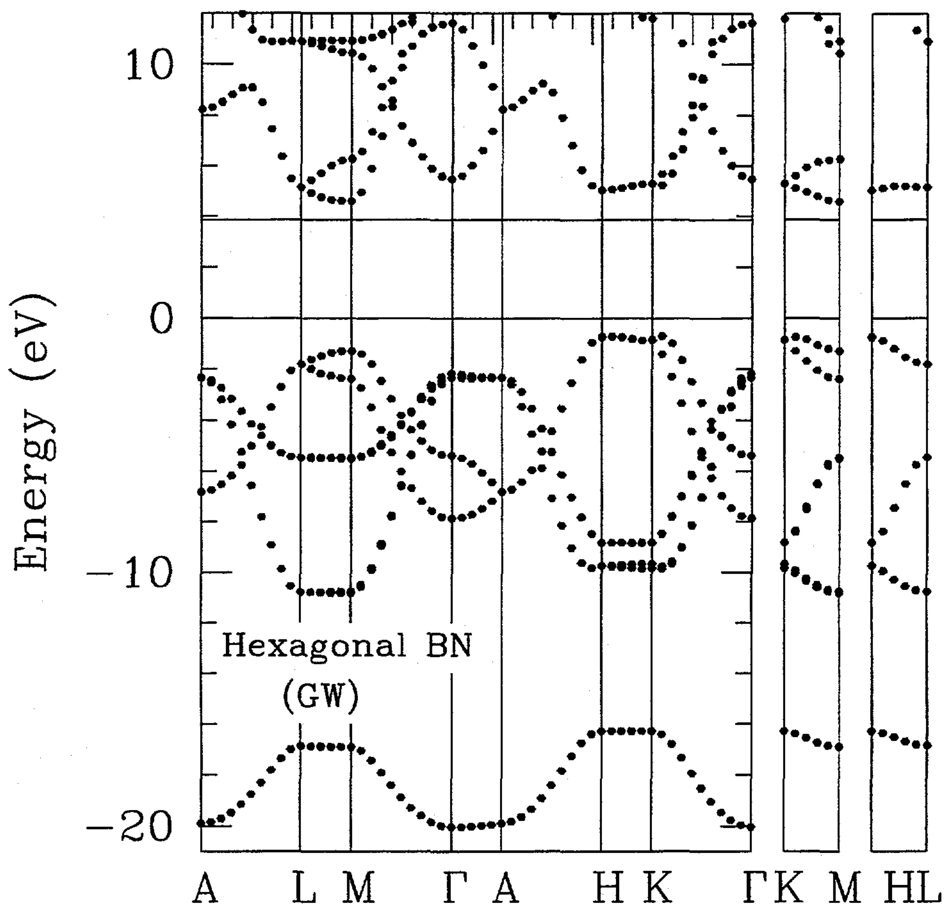

Figure 5.7: GW band structure for bulk hexagonal boron nitride plotted along high symmetry directions of the BZ. The energies are in eV. The top of the LDA valence band is taken to be the zero of energies. The edges of the LDA gap are indicated by horizontal lines as a guide to the eyes.

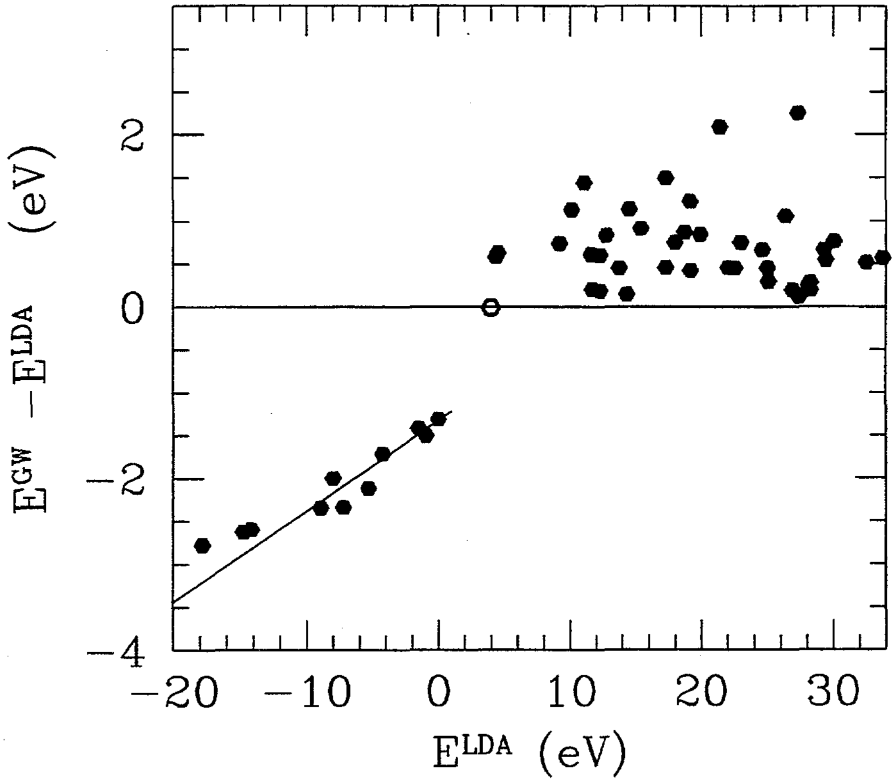

Figure 5.8: The self-energy correction $E^{QP}_{nk} - E^{LDA}_{nk}$ versus the LDA eigenvalues E^{LDA}_{nk} is represented for BN(d=5.5). The energies are in eV. The hollow hexagon represents the self-energy correction for the LUMO state at Γ.

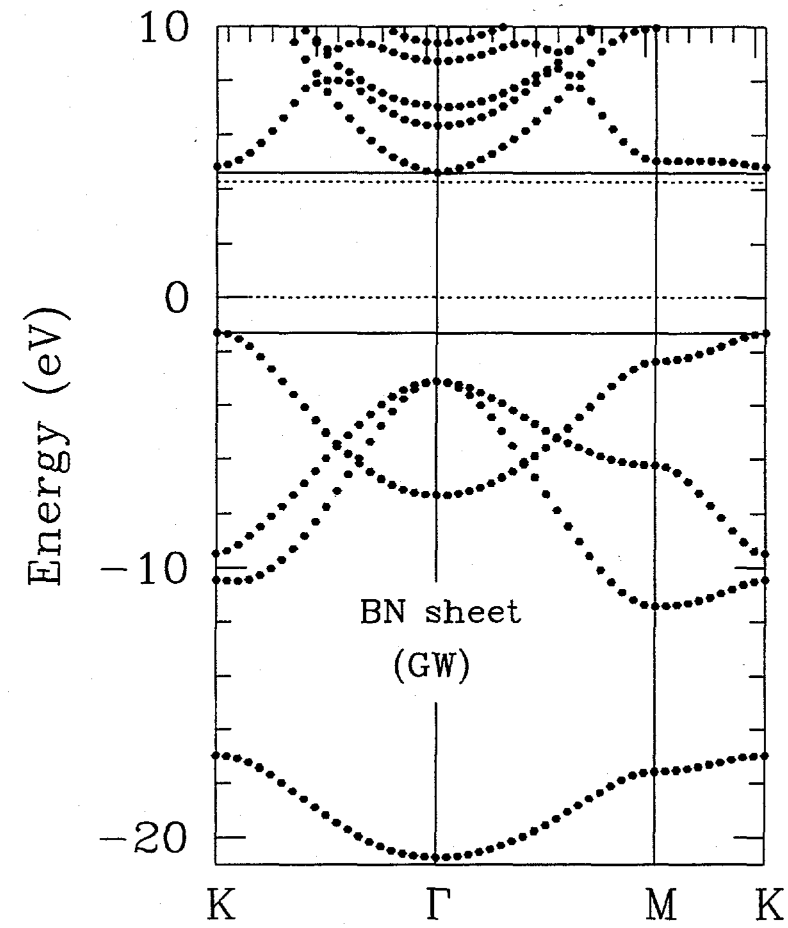

Figure 5.9: GW band structure for an isolated BN sheet plotted along high symmetry directions of the BZ. The energies are in eV. The top of the LDA valence band is taken to be the zero of energies. The edges of the GW gap is indicated by solid horizontal lines and the LDA gap by dashed horizontal lines as a guide to the eyes.

Chapter 6

A mixed-space formalism for quasiparticle energy calculations

6.1 Introduction

The use of reciprocal space formalisms, in which all quantities of interest are expanded in a planewave (PW) basis, has imposed itself as a privileged tool to study the properties of periodic systems. The simplicity of such formalisms, the orthonormality of the PW basis, the unambiguous way of controlling the convergency with respect to the number of basis functions, and the efficiency of fast Fourier transforms (FFT) explain the success of these methods [104]. However, the drawbacks of the PW basis are well-known and are related mainly to the difficulty in using them to describe localized states and to the fact that each region of real space is necessarily described by the same number of planewaves. For systems containing several types of atoms, the deepest potential controls the planewave energy cut-off so that the shallow atomic potential regions are unnecessarily over-converged. Another common situation in modern calculations concerns the study of molecules (or surfaces) in a supercell (or slab) geometry where the vacuum constitutes a large part of the unit cell. Since the number of planewaves needed (at a given energy cut-off) is proportional to the cell volume, a large fraction of CPU-time and memory is spent in describing the vacuum region [105].

For these systems, the use of a real-space formalism presents some advantages. First, localized objects are easily described and different basis functions can be used to describe different regions of space. Another crucial advantage is related to the decay at "large" distance of the screened Coulomb interaction. This is the origin of the success of recent N-linear methods (where N is the number of atoms in the unit cell) proposed to perform band structure calculations in crystals [8, 9, 10, 11]. Furthermore, there is a strong motivation for developing a real-space approach for the study of response functions such as pair distribution functions, Green's functions, polarizability, self-energy operator and vertex correction, which are known to have a shorter range than the screened Coulomb potential.

We present in this Chapter a mixed-space formalism for the calculation of the dielectric response of infinitely extended periodic systems. The response functions f(r,r') of interest are directly calculated on a (r,r') grid in real space. No localized basis such as gaussians, Slater-type, or atomic orbitals are used in the present scheme. In particular, the problems of convergency, non-orthonormality and explicit dependence in ionic coordinates associated with these basis are avoided [106]. In this respect, our method is significantly different from recent real-space approaches based in particular on the use of linear muffin-tin orbitals to express and calculate the dielectric matrices [107], self-energy operator, and quasiparticle energies [108] of periodic systems.

The obvious difficulty related to a purely real-space formalism is that a typical response function, such as the independent polarizability $\chi^0(\mathbf{r},\mathbf{r}')$, do not have the full translational symmetry of the crystal; that is for two lattice vectors $\mathbf{R}$ and $\mathbf{R}'$, $\chi^0(\mathbf{r}+\mathbf{R},\mathbf{r}'+\mathbf{R}')$ is in general not equal to $\chi^0(\mathbf{r},\mathbf{r}')$ unless $\mathbf{R}=\mathbf{R}'$. Therefore, in theory, $\chi^0(\mathbf{r},\mathbf{r}')$ needs to be calculated for $\mathbf{r}$ in a single Wigner-Seitz (WS) cell and $\mathbf{r}'$ in the entire crystal. In practice [109], the response function $\chi^0(\mathbf{r},\mathbf{r}')$ decays rapidly as $|\mathbf{r}-\mathbf{r}'|\rightarrow\infty$ so that for each $\mathbf{r}$, $\chi^0(\mathbf{r},\mathbf{r}')$ would need to be calculated only for $\mathbf{r}'$ in a sphere of radius R_{max} around $\mathbf{r}$. However, for metals, and also small gap semiconductors, the decay of the response function may be slow and R_{max} could span the length of many unit cells so that the computational task would remain considerable.

We show here that $\chi^0(\mathbf{r},\mathbf{r}'|\omega)$ (and related response functions) can be written in terms of a "mixed-spaced" response function $\chi^0_{\mathbf{q}}(\mathbf{r},\mathbf{r}')$ where $\mathbf{r}$ and $\mathbf{r}'$ are restricted to a single Wigner Seitz (WS) cell and $\mathbf{q}$ spans the irreducible part of the Brillouin zone (BZ). This method is shown to be very general, and its application to the calculation of the self-energy operator in the GW approximation [3] is presented.

This chapter is organized as follows. In section 6.2, the formalism for calculation of the polarizability, self-energy operator and quasiparticle energies is presented. In section 6.3, some results are given, and in section 6.4, some extensions of this work and perspectives associated with this method are given. Section 6.5 concludes this chapter.

6.2 Formalism

6.2.1 The independent-particle polarizability

The independent polarizability $\chi^0(\mathbf{r},\mathbf{r}'|\omega)$, which can be explicitly written in terms of the eigen-solutions (ε_i,ψ_i) of a one-electron Hamiltonian [110]:

$$\chi^0(\mathbf{r},\mathbf{r}'|\omega) = \sum_{i,j} (f_i - f_j)\, \frac{\psi^\star_{\mathbf{i}}(\mathbf{r})\psi_{\mathbf{j}}(\mathbf{r})\psi^\star_{\mathbf{j}}(\mathbf{r}')\psi_{\mathbf{i}}(\mathbf{r}')}{\varepsilon_{\mathbf{i}} - \varepsilon_{\mathbf{j}} + \omega + \mathbf{i}\eta} \quad , \tag{6.1}$$

where η is a positive infinitesimal, is the usual starting point for dielectric screening and, subsequent, self-energy calculations. Taking the (i,j) pairs of states to be the usual ($\mathbf{nk}$,$n'\mathbf{k}'$) Bloch states, it is straightforward to show that:

$$\chi^0(\mathbf{r},\mathbf{r}'|\omega) = \sum_{q} e^{i\mathbf{q}\cdot(\mathbf{r}'-\mathbf{r})}\, \chi^0_{\mathbf{q}}(\mathbf{r},\mathbf{r}'|\omega) \quad , \tag{6.2}$$

with

$$\chi^0_{\mathbf{q}}(\mathbf{r},\mathbf{r}'|\omega) = \sum_{n,n',k} (f_{n,k+q} - f_{n'k})\, \frac{u^\star_{n,k+q}(\mathbf{r})u_{n'k}(\mathbf{r})\; u^\star_{n',k}(\mathbf{r}')u_{n,k+q}(\mathbf{r}')}{\varepsilon_{\mathbf{n},\mathbf{k}+\mathbf{q}} - \varepsilon_{\mathbf{n}'\mathbf{k}} + \omega + \mathbf{i}\eta} \quad , \tag{6.3}$$

where the u's are the periodic part of the Bloch states. Obviously, the $\chi^0_{\mathbf{q}}$'s are periodic in space, so that they need to be calculated only for $\mathbf{r}$ and $\mathbf{r}'$ within a single WS cell. In the following, the variable $\mathbf{r}$ will be understood to span the entire space, while the variable ζ will be restricted to a single WS cell. The fact that $\chi^0_{\mathbf{q}}$ is a periodic function is the advantage of the present mixed-space formalism over a straightforward implementation of Eq. 6.1 in real-space. We can rigorously "fold" the entire space onto a single WS cell without having to rely on the decay rate of the response function of interest [111]. In particular, as shown below, the domain of integration of all real-space integrals involved in the calculation of the dielectric response function, the self-energy operator, and the quasiparticle energies can be rigorously restricted to a single WS cell. We emphasize that the combination of Eqs. 6.2 and 6.3 is just a partitioning of the double sum over states in Eq. 6.1 and does not introduce any additional Brillouin zone (BZ) summation. On the contrary, because the $e^{i\mathbf{q}\cdot(\mathbf{r}'-\mathbf{r})}$ phase factor is explicitly preserved in our formalism (in particular not integrated as in Eq. 6.1), conservation of momentum can still be used to restrict BZ summations.

Equation 6.2 can be inverted and we obtain:

$$\chi^0_{\mathbf{q}}(\zeta,\zeta') = \frac{1}{N}\sum_{\mathbf{R}} e^{-i\mathbf{q}\cdot(\zeta+\mathbf{R}-\zeta')}\,\chi^0(\zeta+\mathbf{R},\zeta') \ . \tag{6.4}$$

In particular, if χ^0 is known from the calculation of $\chi^0_{\mathbf{q}}$ on a given $\mathbf{q}$-grid in the irreducible part of the whole BZ, then one can calculate easily $\chi^0_{\mathbf{q}}$ at any $\mathbf{q}$-point in the BZ. We note also that the independent polarizability in reciprocal space can be written:

$$\chi^0_{\mathbf{G},\mathbf{G}'}(\mathbf{q}|\omega) = \frac{1}{\Omega_{WS}}\int\!\!\int d\zeta d\zeta'\, e^{-i\mathbf{G}\cdot\zeta}\,\chi^0_{\mathbf{q}}(\zeta,\zeta'|\omega)\,\mathrm{e}^{\mathbf{i}\mathbf{G}'\cdot\zeta'} \ . \tag{6.5}$$

The inversion of equation 6.5 reads:

$$\chi^0_{\mathbf{q}}(\zeta,\zeta'|\omega) = \sum_{\mathbf{G},\mathbf{G}'} \mathbf{e}^{\mathbf{iG}\cdot\zeta}\, \chi^{\mathbf{0}}_{\mathbf{G},\mathbf{G}'}(\mathbf{q}|\omega)\, \mathbf{e}^{-\mathbf{iG}'\cdot\zeta'} \quad . \tag{6.6}$$

The set of equations 6.1, 6.3, 6.4, 6.5 and 6.6 establishes the relations among the present "mixed-space" formalism, the direct real-space formalism, and the reciprocal space formalism. The same set of relations will be used throughout this chapter to define other mixed-spaced quantities (such as the full polarizability $\chi_{\mathbf{q}}$, the inverse dielectric matrix $\epsilon^{-1}_{\mathbf{q}}$, the screened potential $W_{\mathbf{q}}$, and the self-energy operator $\Sigma_{\mathbf{q}}$) and relate them to their real-space or reciprocal space counterparts.

Compared to the usual Adler-Wiser reciprocal-space formalism, where the $\chi^0_{\mathbf{G},\mathbf{G}'}(\mathbf{q})$ are written (for systems with a gap and ω=0):

$$\chi^0_{\mathbf{GG}'}(\mathbf{q}) = \frac{4}{\Omega} \sum_{c,v,\mathbf{k}} \frac{< v,\mathbf{k}|e^{-i(\mathbf{q}+\mathbf{G})\cdot\mathbf{r}}|c,\mathbf{k}+\mathbf{q} >< c,\mathbf{k}+\mathbf{q}|e^{i(\mathbf{q}+\mathbf{G}')\cdot\mathbf{r}'}|v,\mathbf{k}>}{\varepsilon_{v,\mathbf{k}} - \varepsilon_{c,\mathbf{k}+\mathbf{q}}} \quad , \tag{6.7}$$

the present "mixed-space" scheme (as also the "direct" real-space scheme) does not require the calculation of any matrix elements. This simplification contributes largely to the efficiency of the present scheme as compared to a reciprocal-space approach. Indeed, the calculation of the matrix elements in Eq. 6.7 scales as N^2_{PW} in reciprocal space, where N_{PW} is the number of planewaves used to expand the electron wavefunctions. Further, since such matrix elements must be computed for each combination of valence and conduction bands and **G**-vector, the calculation in reciprocal space of the polarizability matrix $\chi^0_{\mathbf{q}}$ scales as $N^2_{atom}N^2_{PW}N_G$, where N_{atom} is the number of atoms in the unit cell and N_G the size of the dielectric matrix. (N_G and N_{PW} scale also as N_{atom}, but we keep distinct notations here because N_{PW} accounts also for the chemical nature of the atoms. This is a crucial information in this type of calculation. N_G is usually one order of magnitude smaller than N_{PW}). This should be compared to the $N^2_{atom}N^2_\zeta$ scaling of the mixed-space approach, where N_ζ is the number of real-space grid point in the WS cell. Therefore, the ratio of the mixed-space approach to the reciprocal space approach scales as $N^2_\zeta/N^2_{PW}N_G$, where N_ζ and N_G are formally equivalent through Fourier transform. Thus, the reduction in computational effort is then equal to N_G/N_{PW}. In addition, the scaling given above does not take into account the use of a cut-off technique in real-space which, formally, reduces by another factor N_ζ/N_{PW} the cost of the mixed-space approach in the limit of large unit cells.

We note that an alternative scheme would be to adopt a "reciprocal-space" approach but with calculation of the matrix elements in real-space using fast Fourier transform techniques. In this case, the "reciprocal-space" approach would scale as $N_{atom}^2 N_G N_\zeta Log(N_\zeta)$. This is then equivalent to the $N_{atom}^2 N_\zeta^2$ scaling given above for the mixed-space approach. Also, it is important to consider the fact that in the reciprocal-space approach, the number N_G taken to be the size of the dielectric matrix is the number of **G**-vectors within the sphere of radius G_{max} which is inscribed *inside* the polyhedron defined by $G_i \leq G_{max}$ (with G_i the components of the **G** vectors). For a typical BCC or FCC packing, the sphere is roughly 30 % smaller in volume than the corresponding polyhedron, which means that N_G may be actually smaller than N_ζ. This explains why, in the case of bulk silicon (see below), we find "only" a 50 % saving for the mixed-space approach as compared to the reciprocal-space approach (and not one order of magnitude as stated above). As mentioned above, in the case of large unit cells, the scaling of the mixed-space approach reduces to $N_{atom} N_\zeta^2$, that is one N_{atom} factor less that the "alternative" reciprocal-space approach. It is obvious that for large unit cells and for unit cells containing vacuum and/or several types of atom, the saving over the number of grid points effectively used in real-space can easily over-reach the 30% factor described above.

6.2.2 The inverse dielectric response function

Within RPA, the dielectric matrix $\epsilon(\mathbf{r}, \mathbf{r}'|\omega)$ can be calculated from the independent polarizability $\chi^0(\mathbf{r}, \mathbf{r}'|\omega)$ using the following equation:

$$\epsilon(\mathbf{r},\mathbf{r}'|\omega) = \delta(\mathbf{r}-\mathbf{r}') - \int d\mathbf{r_1}\, V(\mathbf{r},\mathbf{r_1})\, \chi^0(\mathbf{r_1},\mathbf{r}'|\omega) \ , \tag{6.8}$$

where V is the bare Coulomb potential. We may define a "mixed-space" dielectric function $\epsilon_{\mathbf{q}}$ by the following equation:

$$\epsilon_{\mathbf{q}}(\zeta,\zeta') = \delta(\zeta-\zeta') - \int d\zeta_{\mathbf{1}}\, \tilde{V}_{\mathbf{q}}(\zeta,\zeta_{\mathbf{1}})\, \chi^0_{\mathbf{q}}(\zeta_{\mathbf{1}},\zeta') \ , \tag{6.9}$$

where $\tilde{V}$ is related to the Coulomb potential V by the following transformation:

$$\tilde{V}_{\mathbf{q}}(\zeta,\zeta_{\mathbf{1}}) = \sum_{\mathbf{R}} V(\zeta+\mathbf{R},\zeta_{\mathbf{1}})\, e^{-i\,\mathbf{q}\cdot(\zeta+\mathbf{R}-\zeta_{\mathbf{1}})} \ . \tag{6.10}$$

Further, the inversion of $\epsilon_{\mathbf{q}}$ yields $\epsilon_{\mathbf{q}}^{-1}$. It is easy to verify that $\epsilon^{-1}_{G,G'}(\mathbf{q})$, $\epsilon^{-1}(\mathbf{r},\mathbf{r}')$ and $\epsilon_{\mathbf{q}}^{-1}(\zeta,\zeta')$ are related to each other through similar relations written in Eq. 6.2, 6.4, and 6.5 for the independent polarizability.

We note that $\tilde{V}_{\mathbf{q}}$ can be efficiently calculated using standard Ewald summation techniques [112]. However, the definition of $\tilde{V}_{\mathbf{q}}$ as $q \rightarrow 0$ requires special care. It is a standard result that (in 3D):

$$\frac{1}{\Omega}\sum_{\mathbf{R}} \frac{e^{-i\,\mathbf{q}\cdot(\zeta+\mathbf{R}-\zeta_{\mathbf{1}})}}{|\zeta+\mathbf{R}-\zeta_{\mathbf{1}}|} = O(\frac{1}{q^2}) \ . \tag{6.11}$$

As expected (see the analysis by Pick *et al* [113]), $\tilde{V}_{\mathbf{q}}$, and also $\epsilon_{\mathbf{q}}$, are non-analytic for $q \rightarrow 0$. We describe in the Appendix to this Chapter how such singularities can be handled in the present formalism.

In the case of isolated molecules in a supercell geometry, one can formally argue that the length of the smallest lattice vector **R** is infinite. Then, the summation over **R**'s in the definition of $\tilde{V}$ can be dropped, leading to a perfectly well defined expression for $\mathbf{q} = 0$. Physically, this means that we switch off the undesirable cell-cell interactions.

6.2.3 The self-energy operator and quasiparticle energies

In this section, we extend the mixed-space formalism to the calculation of the quasiparticle energies in the GW approximation. Following the expression for the self-energy operator Σ in real-space:

$$\Sigma(\mathbf{r},\mathbf{r}';E) = i \int \frac{dE'}{2\pi}\, e^{-i\delta E'}\, G(\mathbf{r},\mathbf{r}';E-E')\, W(\mathbf{r},\mathbf{r}';E') \quad , \tag{6.12}$$

we define the mixed-space screened interaction

$$W_{\mathbf{q}}(\zeta,\zeta') = \int d\zeta_1\, \tilde{V}_{\mathbf{q}}(\zeta,\zeta_1)\, \epsilon_{\mathbf{q}}^{-1}(\zeta_1,\zeta') \tag{6.13}$$

and the mixed-space Green's function

$$G_{\mathbf{q}}(\zeta,\zeta'|\omega) = \sum_n \frac{u_{n\mathbf{q}}(\zeta)u^{\star}_{n\mathbf{q}}(\zeta')}{\omega - \varepsilon_{n,\mathbf{q}} + i\delta} \quad . \tag{6.14}$$

It is then straightforward to show that

$$\Sigma(\mathbf{r},\mathbf{r}';E) = \sum_{\mathbf{q}} e^{i\mathbf{q}\cdot(\mathbf{r}-\mathbf{r}')}\, \Sigma_{\mathbf{q}}(\zeta,\zeta';E) \tag{6.15}$$

where

$$\Sigma_{\mathbf{q}}(\zeta,\zeta';E) = i \sum_{\mathbf{q}'} \int \frac{dE'}{2\pi}\, e^{-i\delta E'}\, G_{\mathbf{q}-\mathbf{q}'}(\zeta,\zeta';E-E')\, W_{\mathbf{q}'}(\zeta,\zeta';E') \quad . \tag{6.16}$$

Further, the matrix elements of Σ with the electron wavefunctions can be written

$$< n\mathbf{k}|\Sigma(E)|n'\mathbf{k}' >= N\, \delta(\mathbf{k}-\mathbf{k}') \int d\zeta d\zeta'\, \psi^{\star}_{n\mathbf{k}}(\zeta)\, \Sigma_{\mathbf{k}}(\zeta,\zeta';E)\, \psi_{n'\mathbf{k}'}(\zeta') \tag{6.17}$$

where conservation of momentum has been used. Equation 6.17 is the key equation for quasiparticle self-energy calculations.

6.3 Results and discussions

We perform test calculations on bulk silicon and on the H/Si(111)-(1x1) surface in a supercell slab geometry. For each case, we generate first the electron wavefunctions in a planewave basis using standard pseudopotential LDA calculations. In the case of the H/Si(111)-(1x1) slab, the details of the unit cell geometry and the LDA calculations are described in Chapter 3. The wavefunctions are then Fourier transformed into real space onto a grid with dimensions equivalent to the $\mathbf{G}$-space grid used in the LDA calculation (e.g. a 18×18×18 grid for bulk silicon which corresponds to a 12 Ry energy cut-off for the expansion of the wavefunctions in reciprocal-space). Further, one grid point out of n is kept in each direction to build the real-space grid on which $\chi^0_{\mathbf{q}}(\zeta,\zeta')$ will be calculated. The convergency with respect to the real-space grid size (that is with respect to n) is then studied by Fourier transforming $\chi^0_{\mathbf{q}}(\zeta,\zeta')$ back to reciprocal-space using Eq. 6.5. The resulting matrix elements, which will be written $\mathrm{FT}[\chi^0_{\mathbf{q}}(\zeta,\zeta')]_{\mathbf{G},\mathbf{G}'}$, are then compared to the $\chi^0_{\mathbf{q}}(\mathbf{G},\mathbf{G}')$ calculated in reciprocal-space using the existing method [2]. The comparison is performed for $|\mathbf{q}+\mathbf{G}|$ and $|\mathbf{q}+\mathbf{G}'|$ up to the typical cut-off value G_{max} used in reciprocal space to determine the dielectric matrix size (e.g. G_{max}= 3 a.u. for bulk silicon). As expected, we verify that a good agreement is reached when the real-space grid is equivalent to the $\mathbf{G}$-space grid on which $\chi^0_{\mathbf{q}}(\mathbf{G},\mathbf{G}')$ is calculated in the reciprocal space approach. In the examples treated below, this corresponds roughly to selecting n=3 (that is N_{PW}= 27 N_{ζ} with the notations of section 6.2.1). Similar tests are performed for $\epsilon_{\mathbf{q}}(\zeta,\zeta')$ and $\epsilon^{-1}_{\mathbf{q}}(\zeta,\zeta')$.

6.3.1 Bulk Silicon

We calculate for selected $\mathbf{q}$-points the independent polarizability $\chi^0_{\mathbf{q}}(\zeta,\zeta')$ on different real-space grids. The summation over the BZ in equation 6.3 is performed with a 4×4×4 Monkhorst-Pack grid in the BZ and 80 states are used in the summation over conduction bands. The results are presented in Table 6.1 where we compare $\mathrm{FT}[\chi^0_{\mathbf{q}}(\zeta,\zeta')]_{\mathbf{G},\mathbf{G}'}$ to $\chi^0_{\mathbf{G},\mathbf{G}'}(\mathbf{q})$ for various set of $(\mathbf{G},\mathbf{G}')$. The $\chi^0_{\mathbf{G},\mathbf{G}'}(\mathbf{q})$'s were calculated using the same BZ sampling and the same number of conduction bands. We include sets of $(\mathbf{G},\mathbf{G}')$ such that $|\mathbf{q}+\mathbf{G}|$ and $|\mathbf{q}+\mathbf{G}'|$ are smaller than 3 a.u. (which is the typical cut-off used for self-energy calculations on bulk Si). We see that the diagonal elements are excellently converged for a 6×6×6 grid in the WS cell, and the non-diagonal elements are well converged for small and medium **G** vectors and reasonably well converged for the largest **G** vectors considered. We note that large **G** vectors account for the very short-range behavior of the screening effects, and we do not expect the small discrepancy observed for these **G** vectors to have a large effect on the values of ϵ^{-1}.

Further, with $\chi^0_{\mathbf{q}}(\zeta,\zeta')$ calculated on the 6×6×6 grid, we calculate $\epsilon_{\mathbf{q}}(\zeta,\zeta')$ following Eq. 6.9 and by inversion we obtain $\epsilon^{-1}_{\mathbf{q}}(\zeta,\zeta')$. The results are summarized in Fig. 6.1 where we compare $\mathrm{FT}[\epsilon^{-1}_{\mathbf{q}}(\zeta,\zeta')]_{\mathbf{G},\mathbf{G}'}$ to the $\epsilon^{-1}_{\mathbf{q}}(G,G)$'s calculated in reciprocal space. In Fig. 6.1(a), the diagonal elements $\mathrm{FT}[\epsilon_{\mathbf{q}}(\zeta,\zeta')]_{\mathbf{G},\mathbf{G}}$ and $\epsilon^{-1}_{\mathbf{G},\mathbf{G}}(\mathbf{q})$ are given (filled circles and left vertical axis) together with the corresponding percent error (open triangles and right vertical axis). The results are in nearly perfect agreement, and the two sets of data are nearly indistinguishable. The maximum per cent error is smaller than 0.1 %, indicating the accuracy of the present calculation. In Fig. 6.1(b), the non-diagonal elements $\mathrm{FT}[\epsilon_{\mathbf{q}}(\zeta,\zeta']_{\mathbf{G},\mathbf{G}'}$ are ploted versus the corresponding $\epsilon^{-1}_{\mathbf{G},\mathbf{G}'}(\mathbf{q})$. The points obtained land nicely on the diagonal line, indicating again the accuracy of the present calculations. The largest errors are related to the large G-vectors off-diagonal elements near the origin on the graph. These matrix elements, which are smaller than 1 % of the diagonal elements, hardly contribute to the screening properties. We emphasize that the accuracy of the mixed-space approach as compared to the reciprocal space approach has more significance than simply noting that, via Fourier transform, a 6×6×6 grid in real-space contains formally as much information as a 6×6×6 grid in reciprocal space. Indeed, the matrix elements calculated in the reciprocal-space approach require to include (for the same accuracy) Fourier components of the wavefunction up to $G_{max} = 12$ Ry in reciprocal space, which amounts to a 18×18×18 sampling grid. This illustrates the power of a real-space approach as compared to the reciprocal approach and explains why, even for bulk silicon, we find the mixed-space approach to be already as efficient as the fully reciprocal space approach. Therefore, the present method has significantly better scaling properties than the reciprocal-space approach, with a crossover between the two methods which occurs for systems as small as bulk silicon.

In a recent study, a "direct" real-space scheme, based on the straightforward implementation of Eq. 6.1 combined with a real-space cut-off technique, has been tested for silicon [109]. We note that in the calculation of $\chi^0(\mathbf{r},\mathbf{r}')$ given by Eq. 6.1 the entire point group of the crystal can be used to reduce the number of independent matrix elements needed to be actually calculated. Practically, one of the variable (say $\mathbf{r}$) can be restricted to the irreducible part of the Brillouin zone (IBZ), the other variable spanning a sphere of radius R_{max} around $\mathbf{r}$ (see Fig. 6.2). In the mixed-space approach, for a given $\chi^0_{\mathbf{q}}(\mathbf{r},\mathbf{r}')$, only the small group of $\mathbf{q}$ can be used to reduce the number of $(\mathbf{r},\mathbf{r}')$ pairs for which the summation over $\mathbf{k}$-points, valence and conduction bands must be performed. However, as soon as R_{max} is larger than the "average" WS cell radius R_{WS}, the effective folding of the entire space on a single WS cell in the mixed-space approach quickly counter-balance this disadvantage. This is illustrated in Fig. 6.2 where we compare the WS cell for bulk silicon to a sphere a radius R_{max} ($\mathrm{R}_{max} \sim 16$ a.u.) centered on a given point $\mathbf{r}$ in the WS cell. As soon as R_{max} is larger than R_{WS} ($\mathrm{R}_{WS} \sim 7$ a.u. for bulk silicon), the area spanned by $\mathbf{r}'$ becomes rapidly much larger in the real-space approach than in the present scheme. For a more quantitative analysis, we calculate the number of "independent" $(\mathbf{r},\mathbf{r}')$ pairs needed in the calculation of $\chi^0(\mathbf{r},\mathbf{r}')$ as a function of the cut-off radius R_{max}. Our 6×6×6 grid in a single WS cell is periodically repeated over the entire space for use in the direct method. The curve corresponding to the real-space method is plotted in Fig. 6.3 (long dash line). As expected, the number of pairs scales as R^3_{max} (that is as the volume of the sphere built around each $\mathbf{r}$ in the IBZ). We discuss now the number of independent pairs required in the calculation of the $\chi^0_{\mathbf{q}}(\mathbf{r},\mathbf{r}')$'s. The average number of pairs for the $\mathbf{q}$'s on a 4×4×4 Monkhorst-Pack mesh in the BZ is given in solid line. Because, for each $(\mathbf{r},\mathbf{r}')$ pair accounted for in this graph, a double summation over the BZ need to be performed in both formalisms (compare Eq. 6.1 for the real-space approach to Eqs. 6.2 and 6.3 for the mixed-space approach), the ratio of the long dash line to the solid line (for a given R_{max}) gives really the ratio of the total number of operations performed to get $\chi^0(\mathbf{r},\mathbf{r}')$ to the number of operations performed to obtain *all* $\chi^0_{\mathbf{q}}(\mathbf{r},\mathbf{r}')$. The cross-over between the two schemes takes place at $\mathrm{R}_{max} \sim 6$ a.u. Following Ref. [109] (and as confirmed in the next section), a cut-off of 16 a.u. is needed in the case of bulk silicon for a good convergency of $\chi^0(\mathbf{r},\mathbf{r}')$ in the direct real-space approach. For such a cut-off, the mixed-space approach is manifestly advantageous over the direct method. Even in the case where "no-symmetry" $\mathbf{q}$-points are used in the present mixed-space approach (upper dotted line), the cross over takes place at $\mathrm{R}_{max} \sim 10$ a.u. This illustrates the advantage of the mixed-space scheme as compared to the direct scheme. We emphasize that the advantage should be even more considerable in the case of metals or small gap semiconductors for which R_{max} may be very large. We note however that, in the limit of large size unit-cell (that is when R_{max} is smaller than R_{WS}), both methods are identical. In particular, if the BZ sampling reduces to the center of the zone Γ, then obviously $\chi^0_{q=\Gamma}(\mathbf{r},\mathbf{r}') = \chi^0(\mathbf{r},\mathbf{r}')$.

6.3.2 H/Si(111)-(1x1) slab

As in the case of silicon, we calculate first $\chi^0_{\mathbf{q}}(\zeta,\zeta')$ on various grids covering the unit cell (with decreasing spacing between the grid points) and compare $\mathrm{FT}[\chi^0_{\mathbf{q}}(\zeta,\zeta')]_{\mathbf{G},\mathbf{G}'}$ to the $\chi^0_{\mathbf{G},\mathbf{G}'}(\mathbf{q})$'s calculated in chapter 3 (as for silicon, the reciprocal space cut-off used for the dielectric calculations in H/Si(111)-(1x1) is $|\mathbf{q}+\mathbf{G}| \leq$

3 a.u.). Results are reported in Table 6.2. With a 6×6×40 grid covering the WS cell, a good convergency of both diagonal and non-diagonal matrix elements is achieved. This grid is similar to the reciprocal space **G**-vectors sampling grid imposed by the 3 a.u. cut-off.

We test now the possibility of taking off the grid sampling points which are located in the vacuum between neighboring slabs. We proceed by subtracting from the mesh entire planes of 6×6 grid points, starting from the planes in the middle of the vacuum and progressing towards the surfaces (the planes of grid points are symmetrically removed from the mesh on both sides of the slab). We find that seven 6x6 layers of grid points can be kept out of the summation in Eq. 6.5 while keeping the $\mathrm{FT}[\chi^0_{\mathbf{q}}(\zeta,\zeta')]_{\mathbf{G},\mathbf{G}'}$ within 1% of their value on the initial 6x6x40 grid. This procedure yields a 6×6×33 grid in real-space and 35% of the CPU-time can be saved by using this grid instead of the 6×6×40 one.

Further, we plot in Fig. 6.4 the maximum value of $|\chi^0_{\mathbf{q}=\mathbf{\Gamma}}(\zeta,\zeta')|$ for a given $|\zeta-\zeta'|$ as a function of $|\zeta-\zeta'|$. We see that $\chi^0_{\mathbf{q}}$ has a decay length which is significantly smaller than R_{WS} in this case (the maximum $|\zeta-\zeta'|$ allowed by the WS cell is $\sim$ 45 a.u.). Thus, we impose a real-space cut-off R_{max} upon the 6×6×33 grid, that is we calculate only the $\chi^0_{\mathbf{q}}(\zeta,\zeta')$ such that $|\zeta-\zeta'|\leq R_{max}$. The results are reported in Table 6.2 for different R_{max}. We see that a cut-off a 16 a.u. can be used which keeps the calculated $\mathrm{FT}[\chi^0_{\mathbf{q}}(\zeta,\zeta')]_{\mathbf{G},\mathbf{G}'}$ within 1% of the values given in Table 6.4 for the 6×6×33 grid. As expected, it is the "long-range" matrix elements which are the most sensitive to a cut-off in real space. This cut-off is the same as used in Ref. [109] for bulk silicon in the direct method. It is important to note that, within a unit-cell, the decay rate of the $\chi^0_{\mathbf{q}}(\zeta,\zeta')$'s is comparable to the decay rate of $\chi^0(\mathbf{r},\mathbf{r}')$.

The combination of both neglecting sampling points in the vacuum and imposing a real-space cut-off adds up to a $\sim$ 58 % saving in CPU-time as compared to the initial regular 6×6×40 grid (see Table 6.3). We plot in Fig. 6.5 a schematic representation of the intersection of the [110] plane with the WS cell. On the left panel, we schematically represent in shaded the "effective" size of the unit cell once the vacuum (unshaded areas) have been "subtracted off" the sampling grid. On the right panel, we symbolize in addition the effect of imposing a real-space cut-off by drawing the portion of effective material (excluding the vacuum) which is intersected by a 16 a.u. radius circle centered on a surface H atom. We note that the number of **G**-vectors needed in the reciprocal-space approach would roughly correspond (via Fourier transform) to a real-space grid covering the entire WS cell, including vacuum. In the "direct" real-space method, the entire shaded semi-circle would need to be sampled. In the mixed-space approach, only the portion of this semi-circle which intersects the WS cell need to be considered. This illustrates the efficiency of the mixed-space approach as compared to both the real-space and reciprocal space approaches.

6.4 Perspectives

An important issue not addressed in this chapter is how to deal with the frequency dependence of the response functions and with the energy integration involved in the calculation of the self-energy operator. We note that the approach used throughout the previous chapters was based on the Hybertsen-Louie's generalized plasmon pole model [79] for $\epsilon_{\mathbf{G},\mathbf{G}'}(\mathbf{q},\omega)$. Such an approach, although has been proven successful for all the systems studied in the previous chapters, may fail to describe correctly the dynamics of electronic excitations in complex materials where more than one "type" of electron is involved. This is exemplified in Appendix A where it is shown that the generalized plasmon-pole model probably fails to describe correctly the dynamics of both the very localized Zn $3d$ electrons and the valence *s-p* electrons of cubic ZnS. Further, it is obvious that a plasmon-pole-type model is not easily adaptable to a real-space approach. For these two reasons, it appears preferable to "explicitly calculate" $\epsilon_{\mathbf{q}}^{-1}(\zeta,\zeta'|\omega)$. On a more general point of view, the knowledge of the frequency dependance of ϵ^{-1} yields straightforwardly the quasiparticle lifetime. Also, this would allow the calculation within the present many-body approach of quantities such as Compton profiles or the total energy of the system.

The explicit calculation of the dynamical behavior of the response functions is a problem which has attracted a lot of attention recently. We note first that the direct use of Eq. 6.1 with ω on the real axis yields singularities which are difficult to handle. A cure to this problem is to calculate $\epsilon_{\mathbf{q}}^{-1}(\zeta,\zeta'|\omega')$ for a set of ω' slightly off the real axis, that is take $\omega' = \omega + i\Delta$, where ω is on the real axis and Δ is a small real number. This is equivalent to introducing a lorentzian broadening of the electronic energy levels (that is a finite lifetime) and the problem of the singularities is circumvented. This method is straightforward to implement and has been used with success to look at the dynamical behavior of atoms [114], clusters [115, 116] and crystals [117]. We note however that, in the case of molecules or small clusters, the plasmon modes may be very sharp (less than 1 eV) so that the spacing needed between successive ω's for which ϵ^{-1} is calculated may be quite small. Since typical plasmon frequencies range from 10 to 30 eV, the calculation of $\epsilon_{\mathbf{q}}^{-1}(\zeta,\zeta')$ may have to be repeated 10 to 30 times, which is computationally very expensive for large systems.

Another method, which has been used in some early GW calculations [109], is to calculate the Green's function $G(\omega)$, the polarizability $\chi^0(\omega)$ and further the dielectric function $\epsilon^{-1}(\omega)$, for ω on the imaginary axis. The advantage here is that these functions are relatively structure-less on the imaginary axis, so that much less ω-frequencies need to be included in the integration of Eq. 6.12 to calculate the self-energy operator. The integration along the imaginary axis can be then continuated onto the real-axis by use of the Cauchy theorem. However, a serious problem related to this method comes from the fact that the self-energy operator $\Sigma(E)$ must be calculated on the quasiparticle energy E=E^{QP}. Practically, $\Sigma(E = E^{QP})$ is evaluated from $\Sigma(E = E^{LDA})$ through a Taylor expansion of $\Sigma(E)$ around E=E^{LDA}. If $\Sigma(E)$ is known only for E on the imaginary axis, such a Taylor expansion is valid only for E outside the E(k) spectrum, so that only the self-energy of the band edge states can be obtained. In addition, if the explicit ω-dependancy of $\epsilon^{-1}(\omega)$, for ω along the real axis, is of interest, then this method cannot be used.

More recent approaches [118, 119, 109] are based on the possibility of analytically continuing $\chi^0(r, r'|\omega)$ from ω in the complex plane to ω near the real axis. The basic idea is to seek if a response functions $f(\omega)$ can be written (for a large range of ω slightly off the real axis) in the form:

$$f(\omega) = \sum_{i=1}^{N} \frac{a_i}{b_i - \omega} \ , \tag{6.18}$$

with a small number N of complex pairs (a_i, b_i) which may be determined by explicitly calculating $f(\omega)$ on selected ω's in the complex plane. Recent calculations performed on bulk silicon [109] suggest that N=2 yields good results for the calculation of the quasiparticle energy.

Further, a promising approach is to combine the present MS approach to the imaginary-time technique introduced in Ref. [109]. The idea is to define MS-Imaginary-Time Green's functions

$$\begin{aligned} G^0_{\mathbf{k}}(\mathbf{r}, \mathbf{r}'|i\tau) = & \quad i \textstyle\sum_v \ \psi_{vk}(\mathbf{r})\psi^\star_{vk}(\mathbf{r}') \, e^{-\varepsilon_{vk}\tau} \ , \qquad \tau \leq 0 & (6.19) \\ = & \ -i \textstyle\sum_c \ \psi_{ck}(\mathbf{r})\psi^\star_{ck}(\mathbf{r}') \, e^{-\varepsilon_{ck}\tau} \ , \qquad \tau > 0 & (6.20) \end{aligned}$$

and calculate $\chi^0_{\mathbf{q}}(\mathbf{r}, \mathbf{r}'|i\tau)$ as follows

$$\chi^0_{\mathbf{q}}(\mathbf{r}, \mathbf{r}'|i\tau) = \ -i \sum_{\mathbf{k}} \ G^0_{\mathbf{k}}(\mathbf{r}, \mathbf{r}'|i\tau) \ G^0_{\mathbf{k}+\mathbf{q}}(\mathbf{r}', \mathbf{r}| - i\tau) \quad . \tag{6.21}$$

The important advantage of this approach is that the summations over valence and conduction bands can now be decoupled, leading in the large system size limit to a N^2 scaling for the calculation of an entire $\chi^0_{\mathbf{q}}(\mathbf{r}, \mathbf{r}'|i\tau)$ matrix. We note that "imaginary frequency" quantities can be obtained as the Fourier transformed of their "imaginary time" analogues and that, as mentioned above, analytical continuation techniques can be used to map the imaginary-frequency axis to the real-frequency axis.

The possibility of including such methods in the present formalism is currently under study.

Another important issue in dielectric response and self-energy calculations is related to the possibility of calculating $\chi^0(\omega)$ without performing any summation over conduction states as done in Eqs. 6.1 and 6.3. These methods are based on the use of the following relation [114]:

$$\begin{aligned}\chi^0(\mathbf{r},\mathbf{r}'|\omega) = \sum_{n,\mathbf{k}} \quad & \psi^\star_{n,\mathbf{k}}(\mathbf{r})\psi_{\mathbf{n},\mathbf{k}}(\mathbf{r}')\ \mathbf{G}(\mathbf{r},\mathbf{r}'|\varepsilon_{\mathbf{n},\mathbf{k}}+\omega) \\ & +\psi_{n,\mathbf{k}}(\mathbf{r})\psi^\star_{\mathbf{n},\mathbf{k}}(\mathbf{r}')\ \mathbf{G}^\star(\mathbf{r},\mathbf{r}'|\varepsilon_{n,\mathbf{k}}-\omega) \end{aligned} \tag{6.22}$$

instead of Eq. 6.1. The needed Green's functions are then calculated by inverting their equation of motion, that is, formally:

$$G(\mathbf{r},\mathbf{r}'|\omega) = <\mathbf{r}|\frac{1}{H-\omega-i\delta}|\mathbf{r}'> \tag{6.23}$$

so that no summation over the conduction bands is needed. Such an approach has been successfully applied to the calculation of the dynamical dielectric response of atoms [114, 120], clusters [116], crystal semiconductors [121] and metals [117]. This is an important improvement because the number of conduction states which need to be included may be very large for unit cells containing a large number of atoms (an average of 30 to 40 bands per atom is usually included in the calculation of χ^0). Using iterative schemes, the inversion required in Eq. 6.23 scales as $\mathrm{N}^2\mathrm{N}_{iter}$, where N is the number of grid points $\mathbf{r}$ and N_{iter} the number of iterations needed to reach convergency. Since practically N_{iter} is usually much smaller than the number of conduction bands, this method offers a significant saving. In addition, such an approach saves the calculation of the conduction states in the step preceding the actual calculation of χ^0. State-of-the-art LDA band structure algorithms scales linearly in CPU-time and memory with the number of bands to be calculated. We note also that all pseudopotentials, and in particular the most popular (because it is the most efficient!) non-local Kleinman-Bylander pseudopotentials, are not as reliable for the calculation of conduction states as they are for the valence bands.

6.5 Conclusion

We presented in this chapter a method which aims at providing a more efficient self-energy calculation scheme. A particularly important domain of application for the new formalism is the calculation of the dielectric function and, further, of the self-energy effects on "low-dimension" systems, such as surfaces, nanotubes, small molecules or clusters in a supercell geometry. It is well known that the self-energy corrections to the LDA eigenvalues for such systems is in general larger than the typical self-energy corrections calculated for extended crystalline systems. For example, it was shown in Chapter 3 that the self-energy correction for H chemisorption, which resemble molecular orbitals, was much larger than the self-energy corrections to the extended bulk states. It is this "differential" correction which led to improving within GW the position of the surface states as compared to the bulk state energy continuum.

However, both dielectric function and self-energy calculations in the framework of the GW approximation are relatively scarce for "real" low-dimension systems such as molecule or clusters. Excitations in metallic clusters, such as alkali or alkaline-earth clusters [116, 118], were mostly investigated in the jellium model. This approach is justified by the fact that the atomic potential for these atoms is very soft, leading to a nearly-free-electron like charge distribution in the cluster environment. In such a jellium model, the goal is merely to study the effect on the dielectric response of confining these nearly-free electrons on given geometrical shapes such as spheres, cylinders or "dots".

It was shown however that the "introduction" of the crystal lattice can change dramatically the position of the plasmon peaks of metallic clusters [122, 123] or crystals [117]. A specific example is the dramatic dependence, for Sb_n clusters

[123], of the photoionization spectra on the molecular architecture. Further, for semiconducting or insulating systems, we expect the introduction of the discrete atomic structure to have even more important effects on the dynamical dielectric response and further the self-energy corrections. As emphasized in Chapter 2, a study of the dielectric response of nanotubes beyond the jellium model [124] would be very interesting. Further, the study of the polarizability and dielectric response of open-ended nanotubes would bring much insight in fundamental questions such as the growth mechanism and capillarity of nanotubes.

Other systems of interest to which the mixed-space approach would be useful are those composed of several types of atoms combining soft and "deep" potentials in the same unit cell. An important example is the II-VI wide gap semiconductors involved in particular in the making of blue-green lasers. We show in Appendix A, where we study cubic ZnS, that while *s* or *p*-like valence wavefunctions can be described with an average of 300 planewaves, more localized $3d$ electrons requires a minimum of 5000 planewaves to be accurately described. In a reciprocal space formalism, the $3d$ electrons define the number of plane-waves used to describe all states. In real-space, it is straightforward to build a fine mesh around the Zn atoms (on which the $3d$ levels are localized) and a much coarser mesh in the remaining part of the unit cell. This scheme would constitute a considerable saving. Another example of interest would be the study of impurities in metals, where typically the metallic ionic potentials are very soft but the impurity potential very deep (e.g. oxygen). Because the unit cell is usually very large (depending on the effective Bohr radius of the impurity state), a study in reciprocal space of the quasiparticle energies of such systems would be prohibitively costly using the energy cut-off imposed by the impurity. As in the case of ZnS, a mixed-space approach with an "adaptive" grid should allow such a study.

The above list of examples is of course not exhaustive. We expect that the new formalism presented here will open many doors and allow the study of new systems. Because the work presented in this Chapter is, in some sense, more "technical" and conceptual, most of its interest lies ahead in the variety and interest of the applications it will allow to tackle.

6.6 Appendix: The long-wavelength limit

In the long-wavelength limit ($\mathbf{q} \rightarrow 0$), the mixed-space potential $\tilde{V}$ can be written (see Ref. [112]):

$$\tilde{V}_{\mathbf{q}}(\zeta,\zeta') = \frac{\sqrt{\pi}}{\Omega_{WS}} \frac{1}{q^2} + A_{\mathbf{q}}(\zeta,\zeta') \ , \tag{6.24}$$

where $A_{\mathbf{q}}$ is analytic for $\mathbf{q} \rightarrow 0$. Further, using $\mathbf{k}\cdot\mathbf{p}$ perturbation theory, one can write (see below):

$$\chi^0_{\mathbf{q}\rightarrow\mathbf{0}} = \chi^0_{\mathbf{q}=\mathbf{0}} + qB_{\mathbf{q}}(\zeta,\zeta') + q^2 C_{\mathbf{q}}(\zeta,\zeta') \ , \tag{6.25}$$

where $B_{\mathbf{q}}$ and $C_{\mathbf{q}}$ are analytic for $\mathbf{q} \rightarrow 0$. To obtain $\epsilon^{-1}_{\mathbf{q}}$ we need therefore to invert a matrix which can be symbolically written: $\mathbf{D}/q^2 + \mathbf{E}/q + \mathbf{F} + q\mathbf{G}$, where again $\mathbf{D}$, $\mathbf{E}$, $\mathbf{F}$ and $\mathbf{G}$ are analytic in q. We note that it is important to "keep track", beyond the leading term, of the singularities all through the inversion (see Ref. [113]) in order to obtain the analytic behavior of $\epsilon^{-1}_{\mathbf{q}}$. One could then formally expand the inverse matrix as follows:

$$(\frac{\mathbf{D}}{q^2} + \frac{\mathbf{E}}{q} + \mathbf{F} + q\mathbf{G})^{-1} = q^2\mathbf{D}^{-1}\left[\mathbf{I} - \mathbf{D}^{-1}\mathbf{E} + ...\right] \ , \tag{6.26}$$

but it is straightforward to show that $\mathbf{D}$ is a singular matrix so that the above expansion cannot be used as such.

An alternative approach is to Fourier transform $\chi^0_{\mathbf{q}}$ to reciprocal space where the singularities are easy to handle (see Ref. [113]). We note however that the Fourier transform of $\chi^0_{\mathbf{q}=\mathbf{0}}(\zeta,\zeta')$ to reciprocal space yields (because of the wavefunctions orthogonality) zero for the head and wings of $\chi^0_{\mathbf{G},\mathbf{G}'}(\mathbf{q} \to 0)$. This is consistent with the fact that the matrix elements of $\chi^0_{\mathbf{G},\mathbf{G}'}(\mathbf{q} \to 0)$ are proportional to $|\mathbf{q}|$ for $\mathbf{q}$ going to zero and $\mathbf{G}$ (or $\mathbf{G}'$) equal to zero. Taking the exact $\mathbf{q} \to 0$ limit requires therefore the calculation of the proportionality coefficient for each of these matrix elements. This can be done using $\mathbf{k} \cdot \mathbf{p}$ perturbation theory. In the case of non-local pseudopotentials V_{NL}, this leads to

$$\psi_{v,\mathbf{k}+\mathbf{q}}(\zeta) = \psi_{v\mathbf{k}}(\zeta) + q\, e^{i\mathbf{q}\cdot\zeta} \sum_{n \neq v} \alpha_n(v\mathbf{k})\psi_{n\mathbf{k}}(\zeta) \ , \tag{6.27}$$

with ($\hbar$ = m = 1 in Rydberg)

$$\alpha_n(v\mathbf{k}) = \frac{< n, \mathbf{k}| - i\hat{\mathbf{q}} \cdot \nabla_{\mathbf{r}} + \ [V_{NL}, i\hat{\mathbf{q}} \cdot \mathbf{r}]|v, \mathbf{k} >}{\epsilon_{n,\mathbf{k}} - \epsilon_{v,\mathbf{k}}} \ , \tag{6.28}$$

where $\hat{\mathbf{q}}$ is the unitary vector in the direction of $\mathbf{q}$. This is equivalent to the reciprocal space formulation for the long-wavelength matrix elements (see Appendix B, Ref. [79])

$$< v, \mathbf{k}|e^{-i\mathbf{q}\cdot\mathbf{r}}|c, \mathbf{k}+\mathbf{q} >= \frac{< v, \mathbf{k}| - 2i\mathbf{q} \cdot \nabla_{\mathbf{r}} + \ [V_{NL}, i\mathbf{q} \cdot \mathbf{r}]|c, \mathbf{k} >}{\epsilon_{c,\mathbf{k}} - \epsilon_{v,\mathbf{k}}} \ , \tag{6.29}$$

The calculation of such matrix elements, which involves the commutator $[V_{NL}, i\hat{\mathbf{q}} \cdot \mathbf{r}]$, is a serious bottleneck in the generation of the independent-particle polarizability since such matrix elements have to be computed for each valence and conduction bands. We note in addition that the use of $\mathbf{k} \cdot \mathbf{p}$ perturbation theory disables the decoupling of the valence and conduction bands which could be gained in an imaginary-time formalism.

For these reasons, a "direct" approach is preferable. In this approach, the additional cost related to treating the $\mathbf{q} \to \mathbf{0}$ limit is transferred to the solving of the Kohn-Sham Hamiltonian for a set of $\mathbf{k}$-points on a slighlty shifted grid $\{\mathbf{k} + \mathbf{q}\}$, where $\{\mathbf{k}\}$ is the $\mathbf{k}$-point grid used in the summation of Eq. 6.3. We note that only the valence wavefunctions in the $\{\mathbf{k} + \mathbf{q}\}$ set are required, so that modern iterative techniques can be used to calculated efficiently the eigenfunctions needed. Preliminary results show that the present method is numerically very stable with respect to the choice of $\mathbf{q}$. For example, in the case of bulk silicon, we verify that $\mathbf{q} = 0.01$ $(\mathbf{1}, \mathbf{1}, \mathbf{1})$ and $\mathbf{q} = 0.001$ $(\mathbf{1}, \mathbf{1}, \mathbf{1})$ yield both excellent results for the matrix elements of the independent-particle polarizability and dielectric response in the long wavelength limit. We note that, as expected, the $\mathbf{q} \to 0$ singularity of $\tilde{V}_{\mathbf{q}}$ in Eq. 6.24 comes from the infinite summation over lattice vectors in Eq. 6.10, that is from the long-range behavior of the Coulomb potential. In practice, the Ewald summation is truncated to a finite number of unit cells, that is $|\mathbf{R}| \leq Na$ where a is the lattice constant and N the number of unit cells considered in each direction in the Ewald summation. This imposes the size of the smallest non-zero BZ $\mathbf{k}$-point to be roughly $2\pi/Na$. In the case of bulk silicon, the $\mathbf{q}$-points selected above correspond to including N = 35 to 350 unit-cells in the Ewald summation. We verify that for $N \geq 30$, the Ewald summation is indeed extremely well converged.

An important case is the one of an isolated cluster or molecule in a supercell geometry. In this case, the BZ summations are restricted to the center of the zone Γ point and the MS formalism is identical to the direct real-space approach. Indeed, Eq. 6.2 reads then

$$\chi^0(\mathbf{r}, \mathbf{r}'|\omega) = \chi^0_{\mathbf{q}=\mathbf{\Gamma}}(\mathbf{r}, \mathbf{r}'|\omega) \quad . \tag{6.30}$$

and Eq. 6.9 become identical to Eq. 6.8. This means that $\tilde{V}$ is now the real Coulomb potential restricted to a single unit cell, consistently with taking the $R \to +\infty$ limit in Eq. 6.10. In practice, this is equivalent to cutting off the spurious cell-cell interactions which arise from the long-range tail of the Coulomb potential. As a consequence, one can take $\mathbf{q}$ exactly equal to $\mathbf{0}$ in Eq. 6.3. This is a considerable advantage of a real-space approach as compared to a reciprocal-space method since (a) we do not need to calculate the valence wavefunctions on a slightly shifted grid and (b) the full group of the crystal can be used to reduce the cost of the calculations.

Finally, we note that even if time-dependent LDA (TDLDA) is preferred over RPA,

$$V(\mathbf{r}, \mathbf{r_1}) = V_C(\mathbf{r} - \mathbf{r_1}) + \frac{dV_{XC}(\mathbf{r})}{dn(\mathbf{r})}\, \delta(\mathbf{r} - \mathbf{r_1}) \,, \tag{6.31}$$

then the LDA exchange-correlation kernel does not introduce any singularity in q since the summation over lattice vectors **R** is prevented by the locality of the LDA exchange-correlation potential (in other words, the LDA kernel is infinitely short range). In the case where non-local kernels may be preferable (to include for example vertex correction beyond TDLDA), one expects such kernels to decay much faster than the bare Coulomb potential and therefore to be analytic in the $\mathbf{q} \rightarrow 0$ limit [125].

Table 6.1: Convergency of selected FT$[\chi^0_{\mathbf{q}=\mathbf{X}}(\zeta,\zeta'|\omega=0)]_{\mathbf{G},\mathbf{G}'}$ for bulk Si as a function of the mesh used in real space.

G and ($\lvert G\rvert^2$)	G' and ($\lvert G'\rvert^2$)	4×4×4	6×6×6	8×8×8	10×10×10
0 0 0 (0.281)	0 0 0 (0.281)	-0.02754	-0.02721	-0.02720	-0.02720
0 1 -2 (4.781)	0 1 -2 (4.781)	-0.02892	-0.01593	-0.01592	-0.01592
1 3 2 (8.532)	1 3 2 (8.532)	-0.02593	-0.00374	-0.00369	-0.00369
0 1 0 (1.031)	-1 0 -1 (1.031)	0.00841	0.00716	0.00715	0.00715
1 3 2 (8.532)	1 1 0 (1.031)	-0.00161	-0.00153	-0.00150	-0.00150
1 3 2 (8.532)	2 3 2 (7.782)	-0.00945	-0.00155	-0.00147	-0.00148

Table 6.2: Convergency of selected FT$[\chi^0_{\mathbf{q}=\mathbf{\Gamma}}(\zeta,\zeta'|\omega=0)]_{\mathbf{G},\mathbf{G}'}$ for H/Si(111) as a function of the mesh used in real space.

G	G'	6×6×32	6×6×36	6×6×40	6×6×48	6×6×64
0 0 -1	0 0 -1	-0.00426	-0.00421	-0.00421	-0.00421	-0.00421
3 2 7	3 2 7	-0.00208	-0.00205	-0.00205	-0.00205	-0.00205
3 2 7	1 -2 7	0.00029	0.00028	0.00028	0.00028	0.00028
0 0 14	0 0 14	-0.02494	-0.01933	-0.01819	-0.01792	-0.01790
0 0 14	-1 0 11	0.00642	0.00530	0.00517	0.00510	0.00509

Table 6.3: Convergency of selected $\mathrm{FT}[\chi^0_{\mathbf{q}=\mathbf{\Gamma}}(\zeta,\zeta'|\omega=0)]_{\mathbf{G},\mathbf{G}'}$ for H/Si(111) as a function of the number of grid points in the vacuum taken off the real space mesh. Starting from a 6×6×40 grid covering the entire Brillouin zone, successive "layers" of grid points in the vacuum are subtracted to the mesh.

G	G'	6×6×39	6×6×37	6×6×35	6×6×33	6×6×31
0 0 -1	0 0 -1	-0.00421	-0.00421	-0.00420	-0.00419	-0.00427
3 2 7	3 2 7	-0.00205	-0.00205	-0.00205	-0.00205	-0.00204
3 2 7	1 -2 7	0.00028	0.00028	0.00028	0.00028	0.00028
0 0 14	0 0 14	-0.01819	-0.01818	-0.01819	-0.01826	-0.01813
0 0 14	-1 0 11	0.00517	0.00516	0.00516	0.00518	0.00508
CPU saved	(%)	4.9	14.4	23.4	31.9	39.9

Table 6.4: Convergency of selected $\mathrm{FT}[\chi^0_{\mathbf{q}=\mathbf{\Gamma}}(\zeta,\zeta')]_{\mathbf{G},\mathbf{G}'}$ for H/Si(111) as a function of the real-space cut-off R_{max}. We study the 6×6×33 mesh and impose in addition $|\zeta-\zeta'| \leq R_{max}$ to determine the pairs (ζ,ζ') for which $\chi^0_{\mathbf{q}}(\zeta,\zeta')$ is calculated.

G	G'	40	30	20	16
0 0 -1	0 0 -1	-0.00419	-0.00419	-0.00417	-0.00413
3 2 7	3 2 7	-0.00205	-0.00205	-0.00205	-0.00205
3 2 7	1 -2 7	0.00028	0.00028	0.00028	0.00028
0 0 14	0 0 14	-0.01826	-0.01826	-0.01826	-0.01823
0 0 14	-1 0 11	0.00518	0.00518	0.00518	0.00518
CPU saved	(%)	31.93	36.5	49.79	58.0

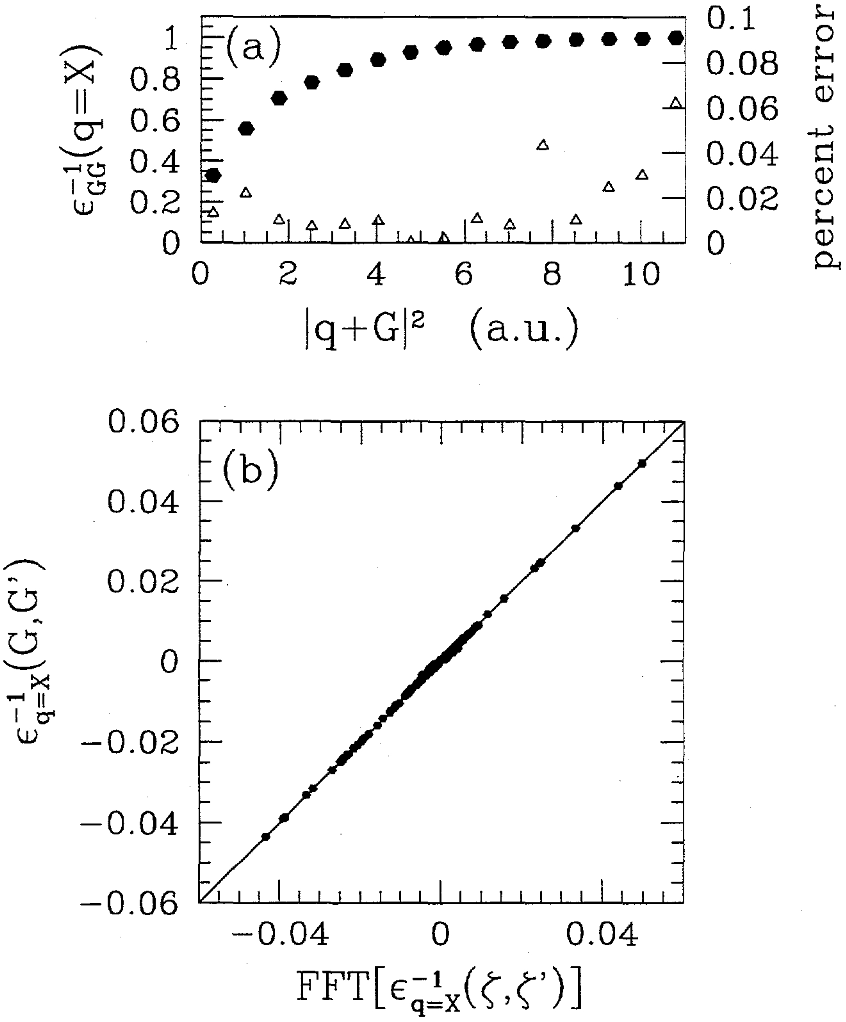

Figure 6.1: (a) The diagonal elements of $\epsilon^{-1}_{q=X}$ for bulk silicon are plotted as a function of $|q+G|^2$ in a.u. (left vertical axis and filled circles). The corresponding error in % between $\epsilon^{-1}_{\mathbf{G},\mathbf{G}}(q=X)$ and $\mathrm{FT}[\epsilon^{-1}_{q=X}(\zeta,\zeta')]_{\mathbf{G},\mathbf{G}}$ is also given (right vertical axis and empty triangles). (b) The non-diagonal elements of $\epsilon^{-1}_{\mathbf{G},\mathbf{G}'}(q=X)$ are plotted as a function of the corresponding $\mathrm{FT}[\epsilon^{-1}_{q=X}(\zeta,\zeta')]_{\mathbf{G},\mathbf{G}'}$ non-diagonal elements. The solid line is a guide to the eyes.

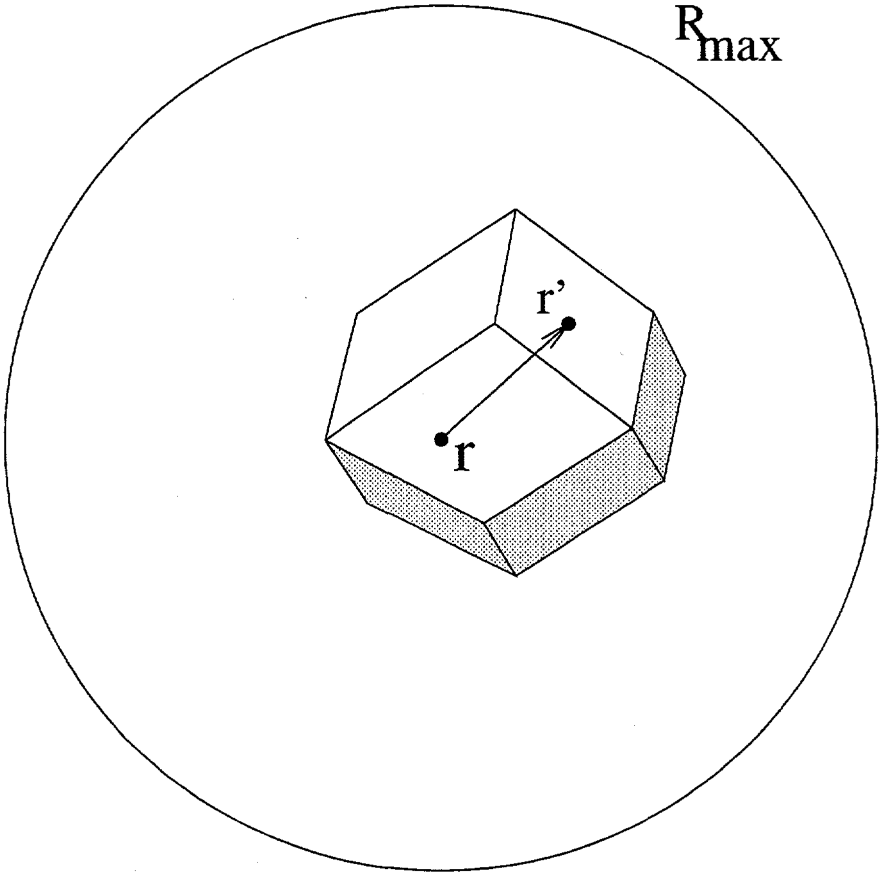

Figure 6.2: The Wigner-Seitz cell for bulk Si is drawn. For a selected **r** in the Wigner-Seitz cell, a circle of radius ~ 16 a.u., centered on **r**, is represented to indicate the domain spanned by **r**' in the "direct" real-space approach.

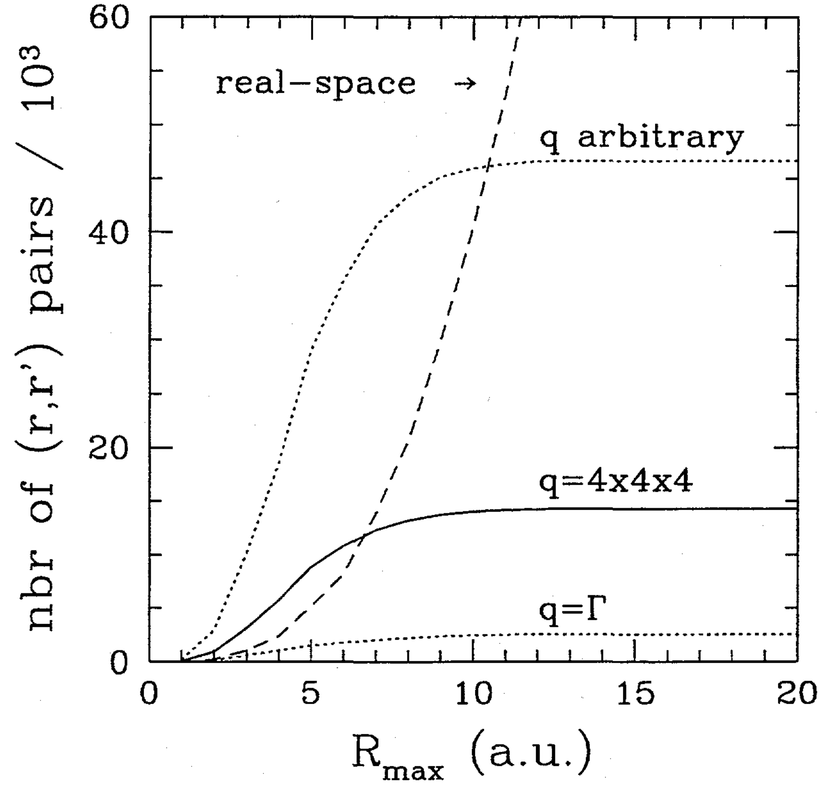

Figure 6.3: Number of "independent" pairs $(\mathbf{r}, \mathbf{r}')$ (see text) in the case of bulk silicon corresponding to a 6×6×6 grid in the Wigner Seitz (WS) cell. The long dash line (with the label "real-space →") corresponds to the real-space approach. The solid line (with the label "q=4×4×4") corresponds to the average number of pairs sampled for $\mathbf{q}$'s on a 4×4×4 Monkhorst-Pack grid in the BZ, and the upper dotted line (with the label "q arbitrary") corresponds to the case where the small group of each $\mathbf{q}$ considered is restricted to the identity. The lower dotted line (with the label "q=Γ") applies when all BZ summations are restricted to the center of the zone.

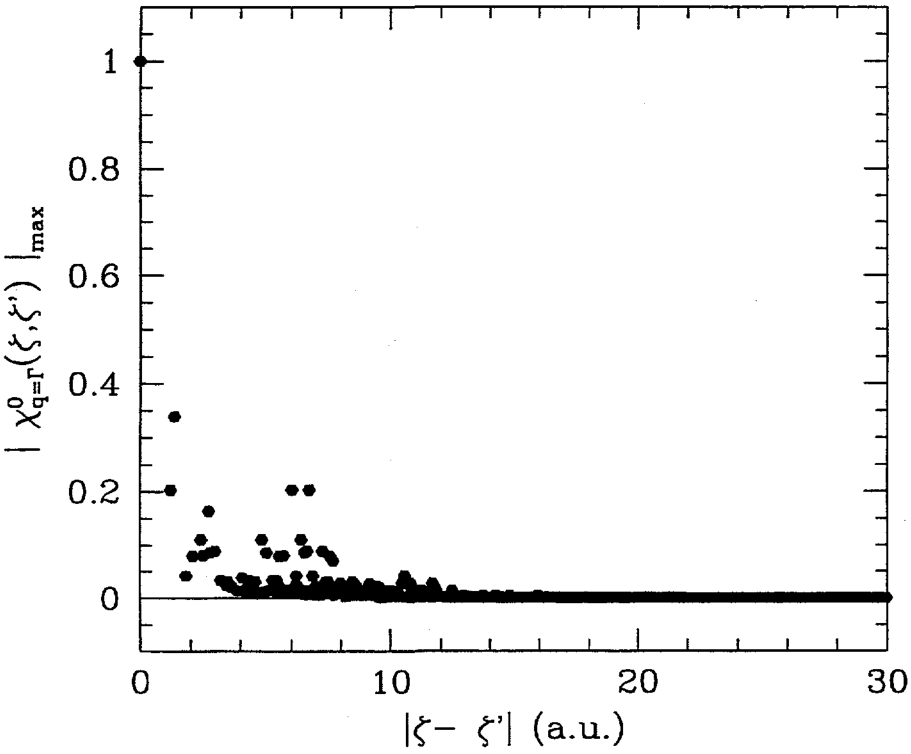

Figure 6.4: Value of $|\chi^0_{q=\Gamma}(\zeta,\zeta')|_{max}$ as a function of $|\zeta-\zeta'|$ for the H/Si(111)-(1×1) slab. $|\chi^0_{q=\Gamma}(\zeta,\zeta')|_{max}$ is renormalized by its value for $|\zeta-\zeta'| = 0$. $|\zeta-\zeta'|$ is in a.u.

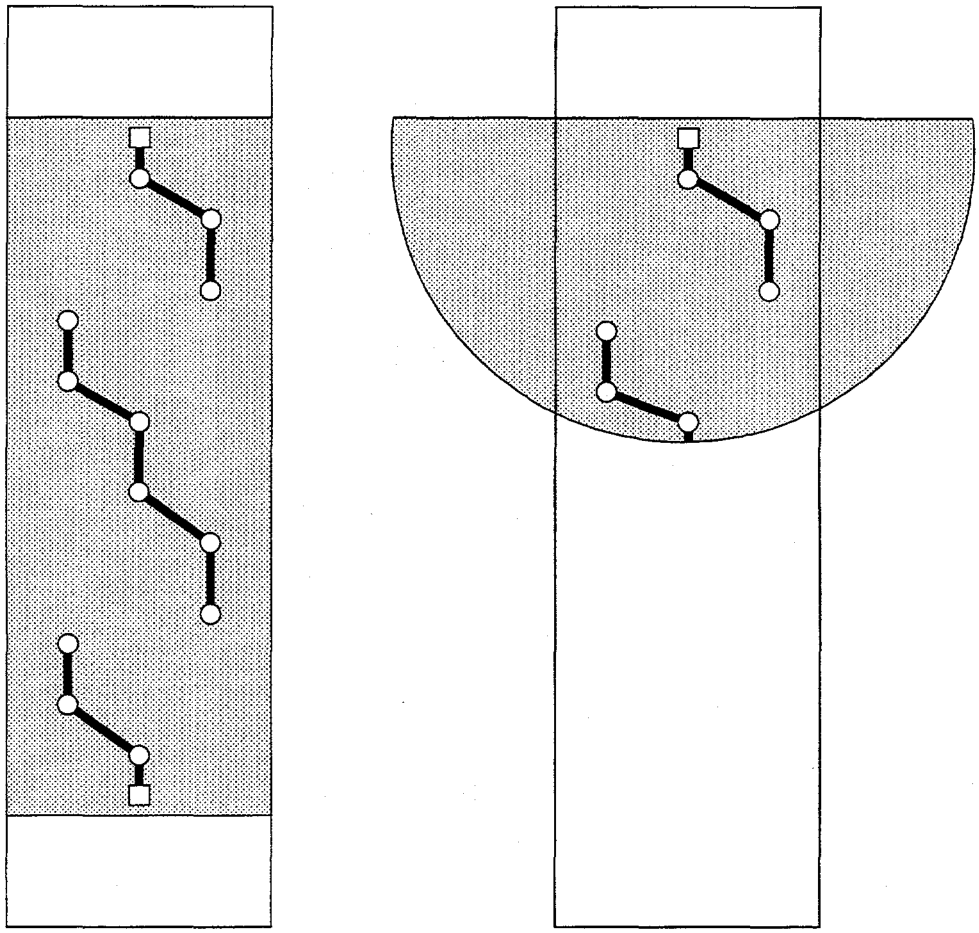

Figure 6.5: Symbolic representation of the cross-section in the [110] plane of a Wigner Seitz (WS) cell of the H/Si(111)-(1x1) surface. The left panel shows in shaded area the effective Wigner Seitz cell excluding vacuum. The right panel shows the effective Wigner Seitz cell spanned by ζ' in the calculation of $\chi^0_q(\zeta,\zeta')$ for ζ on an hydrogen atom. In the mixed-space approach, only the portion of the shaded semi-circle which intersects the WS cell is sampled, while in the real-space method, the entire shaded semi-circle need to be considered. The empty circles represent the Si atoms and the empty squares the hydrogen atoms. Bonds are symbolically represented by thick solid lines.

Appendix A

Quasiparticle energy calculations for cubic ZnS

The technological importance of II-VI semiconducting compounds is mainly related to the making of blue-green short-wavelength lasers [126]. From the theoretical point of view, II-VI semiconductors are challenging compounds; it is known [127] that their structural and electronic properties (in particular the band gap) are importantly related to the position of the metal $3d$ levels in the valence bands. In the case of cubic ZnS, in addition to the usual problem with the LDA gap, because LDA underestimates the binding energy of the Zn $3d$ levels by as much as 4 eV, the p-d repulsion is severely overestimated, leading to a 1.56 eV band gap as compared to the experimental value of 3.8 eV. To explore this problem, we perform in this Appendix a quasiparticle calculation of the band-structure of cubic ZnS. To describe the influence of the Zn $3d$ levels on the electronic band structure, we study both cubic ZnS with the $3d$ levels frozen into the core and with the $3d$ levels fully included in the valence band. We use, respectively, the notations ZnS_{sp} and ZnS_{spd} for these two systems.

The LDA calculations for ZnS_{spd} are carried out using the Zn and S pseudopotentials described in Ref. [128]. In the case of ZnS_{sp}, the non-local d channel is derived from the atomic unoccupied $4d$ level and core correction is used in generating the pseudopotential. Eigenfunctions and pseudopotentials are expanded in a planewave basis. For ZnS_{sp}, planewaves with energy up to E_{cut}= 20 Ry are used to describe the wavefunctions. For ZnS_{spd}, the cut-off is increased up to E_{cut}= 80 Ry in order to describe correctly the Zn $3d$ component of the pseudopotential.

LDA calculations are performed using the experimental lattice constant, that is $a = 10.22$ a.u. for ZnS in the zinc-blende structure. The Ceperley-Alder exchange and correlation potential is used. We present in Fig. A.1 the LDA band structure for ZnS_{sp} (dotted lines) and ZnS_{spd} (full lines) and the energy levels at Γ are given in Table A.1 for both systems. The two band structures have been aligned at the bottom of the conduction band at Γ. In the zinc-blende structure, the crystal symmetry is the tetrahedral T_d group. The top of the valence band at Γ is a 3-fold *p*-like state which transforms according to the Γ_{15} representation of the group. The bottom of the conduction band is a singly degenerate *s*-like state at Γ and transforms according to the Γ_1 representation. Γ_1 and Γ_{15} levels do not couple in the tetrahedral environment. In the crystal potential, the 5-fold $3d$ atomic level is split into a 2-fold Γ_{12v} complex and a 3-fold Γ_{25v} complex. In the tetrahedral environment, the Γ_{12v} does not couple to neither Γ_1 or Γ_{15} levels. We note on Fig. A.1 that the $(\Gamma_{1v} - \Gamma_{1c})$ energy difference is indeed insensitive to the introduction of the $3d$ levels. However, the Γ_{25v} states can couple with the *p*-like Γ_{15v} states at the top of the valence band and *p*-*d* hybridization may be expected to occur between the top of the valence band and the $3d$ levels. The top of the valence band is pushed up to higher energy while the bottom of the conduction bands does not move (since it does not couple to the *d* levels). As a result, the LDA band gap reduces from 2.37 eV (for ZnS_{sp}) to 1.56 eV (for ZnS_{spd}) under introduction of the *d* level in the valence complex.

We perform first a quasiparticle calculation on ZnS_{sp} following the procedure described in section 3.2.2. We calculate the static dielectric response in the random phase approximation (RPA). In the summation over the conduction bands, 80 bands are included. Local field effects are taken into account by calculating the off-diagonal elements of the inverse dielectric response $\epsilon^{-1}_{GG'}(q)$ with a cut-off of $|\mathbf{q} + \mathbf{G}| \leq 3$ a.u. The dielectric constant is calculated to be 5.43 for ZnS_{sp}. This is 4.5-6.5 % larger than the experimental value of 5.1-5.2. Calculations performed on IV or III-V compounds show that the RPA macroscopic dielectric constant is on the average larger than the experimental one by at least 10 %. The relatively better agreement found here indicates that the $3d$ levels are also slightly polarizable and that they should yield a small, but not negligible, contribution to the polarizability of the present system.

We turn now to the calculation of the quasiparticle energies. Results are reported in Table A.1 along with the LDA values. The self-energy corrections to the LDA energy for states at Γ for ZnS_{sp} are represented in Fig. A.2 (empty circles). In particular, the band gap opens from 2.37 eV (LDA value) to 3.97 eV. We study also the influence of using core-correction when generating the Zn pseudopotential. Results are reported in Table A.2. We do not observe any significant modification of both the LDA and quasiparticle band-structures. We also test the accuracy of using the Levine-Louie model dielectric function [129] as compared to RPA (see Table A.2). Consistently with previous calculations [17], the two approaches give very similar results for states around the gap, even though (see Fig. A.2), the model yields too small a screening in the intermediate range. We note that the GW band gap of 3.97 eV obtained in this calculation is actually larger than the experimental band gap. This is unusual since previous calculations on *s*-*p* bonded semiconductors show that the GW band gap is usually slightly smaller than the experimental value. This fact is just a reminder that in real cubic ZnS, *p*-*d* repulsion is a factor of importance and that a quasiparticle calculation performed on ZnS_{spd} should yield a smaller gap.

We then perform the self-energy calculation of the band-structure of ZnS_{spd}. We include 120 bands in the summation over the conduction states and the dielectric matrix is cut at $|\mathbf{q}+\mathbf{G}| \leq 4$ a.u. With these values, the macroscopic dielectric constant is calculated to be $\epsilon_M = 7.58$. This is at least 43 % larger than the experimental value. This means that the use of the LDA eigenvalues and eigenfunctions to calculate within RPA the dielectric constant of cubic ZnS leads to a severe overestimation of the polarizability of the $3d$ levels. Both the severe reduction within LDA of the Zn $3d$ to conduction band energy differences and the introduction of too strong a p character in these $3d$ levels (which allows transitions which should be by symmetry disallowed), can explain this fact. If we use further this static dielectric function to calculate the quasiparticle energies of ZnS_{spd}, we obtain the self-energy corrections to LDA as plotted in Fig. A.2 (filled circles). The most striking result is that the self-energy correction, instead of bringing the $3d$ levels down to a larger binding energy, worsens the situation by pushing them up in energy by as much as 2.90 eV. In addition, the self-energy correction for states near the gap is reduced as compared to the ZnS_{sp} case, while the self-energy for the bottom of the valence band is increased. We do not have, at the time of redaction of this section, a clear explanation for such a failure of GW. However, we feel that this "unsuccessful" calculation contains novel and important informations concerning the limits of the present self-energy approach. In the following, we enumerate some facts and the results of some "computational experiments" which suggest the possible origin(s) of the problem:

a) We look at the Hartree-Fock eigenvalues associated with the Zn $3d$ levels, that is we calculate:

$$E_{3d}^{HF} = \epsilon_{3d}^{LDA} + < \psi_{3d} | V_x - V_{LDA} | \psi_{3d} > \tag{A.1}$$

where V_x is the bare exchange operator. Since the bare exchange operator does not require the knowledge of the screening, it is free from the errors found for the dielectric matrix. Further, since the $3d$ levels system does not couple to the Γ_{1c} LUMO state, we are confident that the self-energy correction to LDA found for this state in the ZnS_{sp} system (0.42 eV) applies to the ZnS_{spd} system. With this correction, we can estimate the "correct" quasiparticle energy for this state in ZnS_{spd}. We find that the "Hartree-Fock" $3d$ levels obtained from Eq. A.1 are located around 12.8 eV below the "correct" quasiparticle energy of the LUMO state at Γ. This is in excellent agreement with the experimental value of 13-13.5 eV for this transition energy. This computational "experiment" seems to indicate that vertex corrections should not contribute significantly to the Zn $3d$ quasiparticle energy.

b) We find that the LDA wavefunctions are not in the present case a good approximation for the quasiparticle wavefunctions. As explained above, the *p*-*d* coupling is severely over-estimated within LDA, so that both the Γ_{25v} and the Γ_{15v} levels have, respectively, too much p and d character. We check this by calculating the non-diagonal elements of the self-energy operator. Results are reported in Table A.3. We look first at the ZnS_{sp} system. Most non-diagonal elements are zero because of symmetry arguments. For example, the non diagonal elements between the Γ_{1v} and Γ_{15v} occupied states are strictly equal to zero in ZnS_{sp}. Nevertheless, as exemplified in Table A.3, the Γ_{1v} and Γ_{1c} levels can couple and the self-energy operator yields indeed a large non-diagonal element between these two levels. However, this matrix element is equal, within 0.27 %, to the LDA exchange-correlation potential expectation value between the same states, so that for the difference operator $(\Sigma - V_{xc}^{LDA})$, this non diagonal element is negligible as compared to the diagonal terms. Turning now to the case of ZnS_{spd}, we calculate the non-diagonal elements that couple the Γ_{25v} to the Γ_{15v} levels. As shown in Table A.3, the non-diagonal elements of $(\Sigma - V_{xc}^{LDA})$ between these levels can be of the same order of magnitude as compared to the diagonal self-energy correction itself. However, we notice that the Γ_{12v} levels cannot couple to the Γ_{15v} *p*-like levels and we check indeed that the non-diagonal elements of Σ and V_{xc}^{LDA} are zero with the Γ_1, Γ_{15} or Γ_{12} levels. This indicates that the problem does not entirely lie in the quality of the LDA wavefunctions.

c) To improve upon the mediocre quality of the LDA eigenvalues and wavefunctions, we build an *ansatz* pseudopotential for Zn designed to yield better Zn $3d$ eigenvalues and eigenfunctions in the LDA self-consistent calculation. Our scheme is to add to the Zn pseudopotential a short range attractive potential $\delta V(|r|)$ adjusted such that it pulls down the $3d$ levels to their experimental position. Formally, the energy levels obtained with such a potential can be written

$$\tilde{E} = < T > + < V^{ionic} > + < V_H > + < \tilde{V}_{xc} > \tag{A.2}$$

where T is the kinetic operator, V^{ionic} the ionic pseudopotential, V_H the Hartree potential and $\tilde{V}_{xc} = V_{xc}^{LDA} + \delta V(|r|)\hat{P}_d$. Because of the projector $\hat{P}_d$ on the L=2 spherical harmonic, $\delta V(|r|)$ will be seen only by the $3d$ electrons. Roughly speaking, $\tilde{V}_{xc}$ is an effective exchange-correlation potential designed to mimic the Hartree-Fock exchange operator for the $3d$ levels only. We verify indeed that for the $3d$ levels: $< \tilde{V}_{xc} >_{3d} \sim < V_x >_{3d}$. With this *ansatz* Hamiltonian, we find that the s and p levels are very similar to those obtain for the ZnS$_{sp}$ system, except for the band gap which we find to be 2.50 eV instead of 2.41 eV for the ZnS$_{sp}$ system. This may seem surprising since the $3d$ levels, even located 10 eV below the top of the valence band, should still exert a small repulsion effect on the Γ_{15} states, leading to a smaller gap as compared to ZnS$_{sp}$. However, because indeed there is still a small p-d coupling, the Γ_{15} states feel, through their d component, the attractive $\delta V(|r|)\hat{P}_d$ potential. We find the expectation value of $\delta V(|r|)\hat{P}_d$ with the Γ_{15} states to be -0.4 eV. Without this contribution, the band gap would be 2.1 eV, that is 0.31 eV smaller than in the ZnS$_{sp}$ case. This 0.31 eV is therefore an estimate of the "real" p-d repulsion in cubic ZnS. We check that, as expected, $\delta V(|r|)\hat{P}_d$ has no matrix elements with the Γ_{1c} and Γ_{1v} levels. Further, with this new set of eigenvalues and eigenfunctions, we calculate the RPA response function. We find ϵ_M to be 5.68, that is in much better agreement with experiment. We perform then the self-energy calculations. The quasiparticle energies are obtained through

$$E^{QP} = \tilde{E} + < \tilde{\psi} | \Sigma - \tilde{V}_{xc} | \tilde{\psi} > \tag{A.3}$$

where $(\tilde{E}, \tilde{\psi})$ are the eigenvalues and eigenfunctions obtained from the LDA calculation performed with $\delta V(|r|)\hat{P}_d$ added to the original LDA Hamiltonian. The quasiparticle band gap is calculated to be 3.73 eV in excellent agreement with experiment. However, the Zn $3d$ levels land around 4-4.5 eV below the top of the valence band. This is comparable to the position of the $3d$ levels in the quasiparticle approach for the original ZnS$_{spd}$ system. Therefore, even with a "correct" p-d

coupling and a good static dielectric function, yielding quasiparticle *s-p* levels in excellent agreement with experiment, the $3d$ levels are not well treated within the present GW approach. However, again, we verify that the Hartree-Fock treatment:

$$\tilde{E}_{3d}^{HF} = \tilde{E}_{3d} + < \tilde{\psi}_{3d} | V_x - \tilde{V}_{xc} | \tilde{\psi}_{3d} > \tag{A.4}$$

yields the experimental position for the $3d$ levels. Therefore, the failure of the present GW approach for the $3d$ levels lies in the fact that self-energy operator $\Sigma = iGW$ and the bare Fock operator V_x do not yield the same expectation value for the $3d$ levels. Equivalently, the Coulomb-hole and screened-exchange contributions to $\Sigma = iGW$ do not cancel out as they should. Since the GW approximation *per se* is found to be reasonable, this suggests that the dynamical effects are ill-described within the present generalized plasmon-pole approach.

In conclusion, we suggest the following scheme to perform a fully *ab initio* study of the ZnA compounds, with A= O, S, Se or Te. We follow the prescription of (c) to yield a better basis for the self-energy calculation. However, to avoid the "empirical" aspect of the scheme presented in (c), we perform both an atomic LDA and HF calculation for Zn and build $\delta V(|r|)$ to be:

$$\delta V(|r|) = V_x^{HF,atom}(|r|) - V_{xc}^{LDA,atom}(|r|) \quad . \tag{A.5}$$

Because the $3d$ levels do not relax significantly in the crystal, we can write:

$$< \delta V(|r|) > + < V_{xc}^{LDA,crystal} > \sim < V_x^{HF,atom} > \sim < V_x^{HF,crystal} > \tag{A.6}$$

where the expectation value is understood to be taken over the $3d$ states. The $3d$ levels are therefore treated in an Hartree-Fock way while the s and p electrons feel the standard LDA exchange-correlation potential. We have tested this approach and find similar results as the one given in (c), but this scheme has the advantage of being parameter free [130]. Further, it appears necessary to go beyond the generalized plasmon-pole model to describe correctly the dynamical effects on the self-energy operator for the 3*d* levels. A recent self-energy calculation performed on Ni [108] yielded reasonable results within the GW approximation, while calculating explicitly the energy dependence of the dielectric function. Further, the spectral function calculated in this work exhibited two peaks around -20 and -30 eV. These peaks were identified as plasmon peaks. This confirms that the one plasmon pole model may fail for such systems. It is not surprising that the localized 3*d* levels and extended *s*-*p* states do not share the same dynamics, and we expect the 3*d* levels to yied a plasmon peak at higher energy than the *s*-*p* electrons. We indicate to the reader that a systematic study, within the GW approximation, of the quasiparticle band structure of II-VI compounds with *d* electrons in the core has been carried out in Ref. [131].

Table A.1: LDA and GW eigenvalues at Γ for zinc-blende ZnS_{sp} and ZnS_{spd}. The zero of energy is set at the top of the valence bands. Energies are in eV.

	ZnS_{sp}		ZnS_{spd}		exp.
	LDA	GW	LDA	GW	
Γ_{1v}	-12.63	-12.73	-13.47	-14.55	
Γ_{25v}			-6.93	-4.47	$\sim$ -10
Γ_{12v}			-6.46	-3.49	$\sim$ -10
Γ_{15v}	0.00	0.00	0.00	0.00	0.00
Γ_{1c}	2.37	3.97	1.56	2.26	
Γ_{15c}	6.83	8.87	5.96	6.91	

Table A.2: Quasiparticle energies at high-symmetry points for ZnS_{sp}. The influence of the core-correction in the pseudopotential and of the use of the Levine-Louie model dielectric function as compared to full RPA is presented. Energies are in eV and referenced to the top of the valence band in each case.

level	Without core correction		With core correction			Exp.
	LDA	GW-RPA	LDA	GW-model	GW-RPA	
Γ_{1v}	-12.61	-12.71	-12.63	-13.42	-12.73	-13.5
Γ_{15v}	0	0	0	0	0	0
Γ_{1c}	2.47	4.22	2.373	3.98	3.97	3.80
Γ_{15c}	6.82	8.91	6.83	8.74	8.87	8.35
X_{1v}	-10.89	-11.06	-10.92	-11.71	-11.08	-12.0
X_{3v}	-4.61	-4.82	-4.591	-4.89	-4.80	-5.5
X_{5v}	-1.93	-2.00	-1.935	-2.06	-2.01	-2.5
X_{1c}	3.66	5.45	3.548	5.14	5.30	
X_{3c}	4.40	6.31	4.339	6.025	6.20	4.9
L_{1v}	-11.33	-11.48	-11.352	-12.15	-11.50	-12.4
L_{1v}	-4.89	-5.10	-4.90	-5.2	-5.11	-5.5
L_{3v}	-0.74	-0.76	-0.73	-0.78	-0.78	-1.4
L_{1c}	3.66	5.53	3.60	5.28	5.425	
L_{3c}	7.33	9.38	7.29	9.17	9.289	

Table A.3: Real-part of the non-diagonal elements for the self-energy Σ, the LDA exchange-correlation potential V_{xc}^{LDA} and the difference $\Sigma - V_{xc}^{LDA}$ operators. Values are given for selected levels of Si, ZnS$_{sp}$ and ZnS$_{spd}$. ZnS is in the zinc-blende structure. Energies are in eV.

(i,j)	$<\Sigma>_{ij}$	$<V_{xc}^{LDA}>_{ij}$	$<\Sigma - V_{xc}^{LDA}>_{ij}$
		Si	
(1,9)	-1.7741	-1.7759	0.0018
		ZnS$_{sp}$	
(1,5)	2.9827	2.9745	0.0082
		ZnS$_{spd}$	
(2,7)	0.4664	0.7894	-0.3230
(2,8)	-2.3520	-3.8349	1.4823
(2.9)	-0.0558	-0.0396	-0.0162

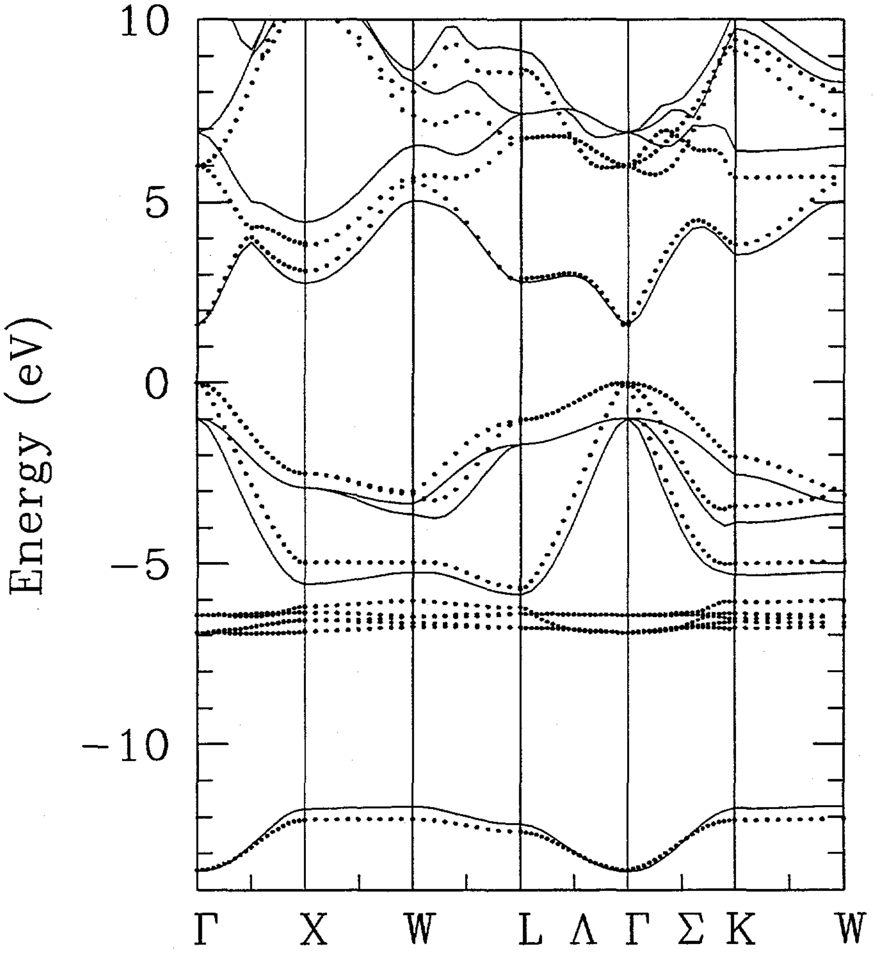

Figure A.1: LDA band structures for ZnS_{sp} (solid lines) and ZnS_{spd} (dotted lines). Both band structures have been aligned at the bottom of the conduction bands at Γ. The zero of energies is the top of the valence band of ZnS_{spd}. The energies are in eV.

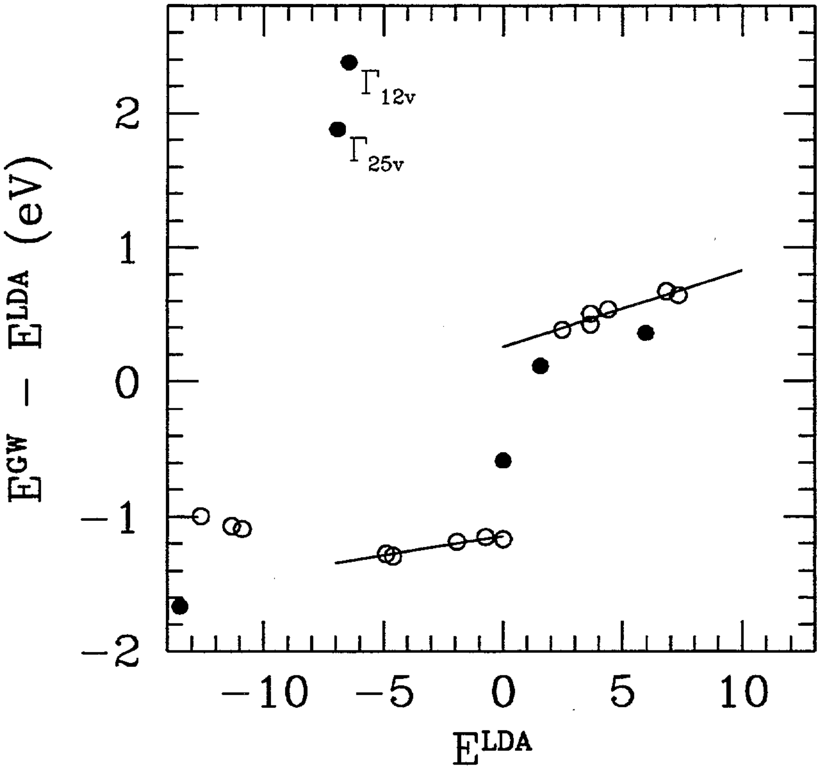

Figure A.2: Self-energy corrections ($E^{GW} - E^{LDA}$) as a function of E^{LDA} for selected states at Γ for ZnS$_{sp}$ (open circles) and ZnS$_{spd}$ (filled circled). Energies are in eV.

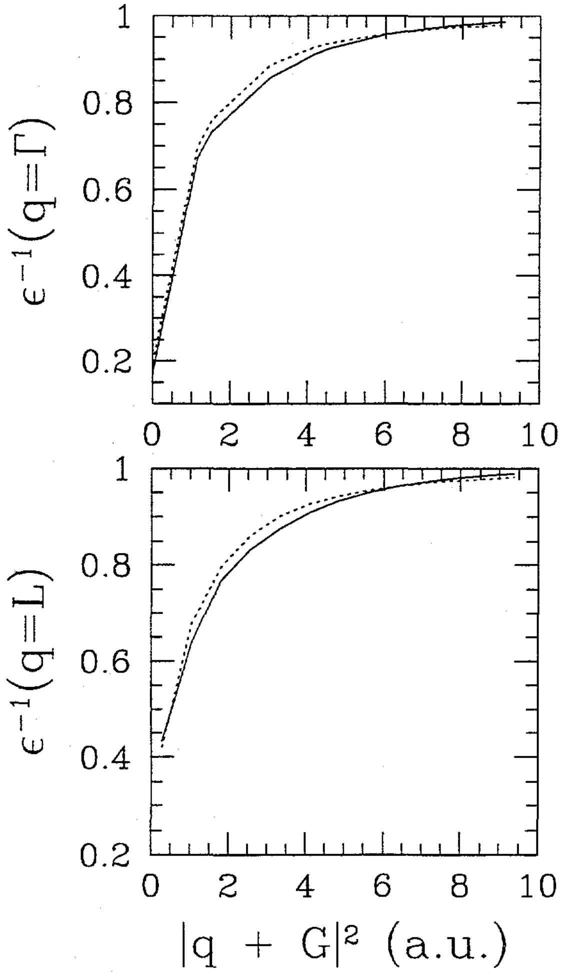

Figure A.3: Comparison of the diagonal elements of the model (dotted lines) and the RPA (solid lines) ϵ^{-1} for ZnS_{sp} at Γ and L.

Appendix B

Two-phonon bound states at the H/C(111)-(1×1) surface

In order to explain an anomaly in the Raman spectrum of bulk diamond [132], the existence of a two-phonon bound state was suggested [133]. Even though it was shown later [134] that such a state cannot exist in bulk diamond (the effective anharmonic coupling between optical phonons is actually repulsive in this system), the mechanism for the pairing of two delocalized vibrational quanta was understood. Because the localization of two phonons over a few bond lengths requires a large negative phonon-phonon coupling compared to the one-phonon energy dispersion, two-phonon bound states were suggested to be found mainly in molecular crystals, where the intra-molecular forces are usually much larger than the Van der Waals inter-molecular forces. However, recently, the existence of a two-phonon bound state was observed at the hydrogen covered Si(111) surface [135]. Two reasons favor the existence of this state. First, the bond formed by the adsorbate with the substrate atom exhibits a strong molecular character. Second, the lower dimension of a surface, as compared to bulk, favors the existence of bound states. We present in this paper a calculation of the binding energy of a two-phonon bound state at the H/C(111)-(1x1) surface. We show that the anharmonic phonon-phonon coupling is larger than in the case of the H/Si(111)-(1x1) surface. In addition, the one-phonon energy dispersion is much smaller in the present case of carbon susbtrate. Both arguments lead to a larger binding energy for the two-phonon bound states at the H/C(111)-(1x1) surface. The dispersion of the two-phonon bound state band is calculated to be 14 times smaller than its analogue at the H/Si(111) surface, leading to very localized two-phonon bound states.

We use a slab model to study theoretically the vibrational modes of H on the

C(111)-(1×1) surface. Total energies are calculated within the local density approximation of the density functional theory. The wavefunctions are expanded in a planewave basis and the ionic potentials are described by *ab initio* pseudopotentials. Technical details for the slab geometry, energy cut-off and carbon pseudopotential can be found in Ref. [136]. Following a previous work on H/Si(111)-(1×1) surface [67, 137], an hydrogen pseudopotential has been generated to describe the proton Coulombic potential.

We perform a large number of frozen-phonon calculations and determine the coefficients of the fourth-order polynomial used to model the potential in which each hydrogen atom is moving in phase with others:

$$\begin{aligned} V(x,y,z) &= V_0 + \frac{m}{2}[\omega_{0z}^2 z^2 \ + \omega_{0x}^2(x^2+y^2)] + a_3 z^3 \ + b_3(x^2+y^2)z \\ &\quad + a_4 z^4 \ + b_4(x^2+y^2)z^2 + c_4(x^2+y^2)^2 \ . \end{aligned} \tag{B.1}$$

This potential includes the effects of both the anharmonicity of the stretching mode and the coupling between stretching and wagging motions. The mass m is the reduced mass of the C-H two-body problem. We plot in Fig. B.1(a) the calculated potential for the (x=y=0) stretching motion and in Fig. B.1(b) for the (z=0) wagging motion. In Fig. B.1(b), for each value of $\rho = \sqrt{x^2+y^2}$ that we considered, we plot two points which correspond to the maximum and minimum value of V(x,y,z=0). One can see that for the range of ρ-values considered, (which corresponds to wagging angles smaller that $\theta_{max} < 1.2^o$), the anisotropy is very small. This justifies the choice of a (x,y)-symmetrical potential for the motion of H at the diamond surface. The values for the coefficients of Eq. B.1 are reported in Table B.1, together with the results of Ref. [136] for the uncoupled C-H stretching mode. The small difference between the two studies can be accounted for by the use of a pseudopotential for hydrogen instead of the full Coulombic potential. We report also the coefficients obtained in Ref. [138] for the H/Si(111)-(1×1) system. We note that while the frequency ω_{0z} and ω_{0x} for the uncoupled motions are much larger in the H/C case, the wagging-stretching coupling coefficients b_3 and b_4 are comparable in both systems. Therefore, the coupling between the wagging and stretching modes is relatively less effective in the case of the diamond substrate.

This model potential is then diagonalized in the basis of the 3D harmonic oscillators $\mid n_x, n_y, n_z >$, and quantum numbers up to $n_x = n_y$=10 and n_z=20 are included to converge the lowest eigenvalues up to the second excited stretching mode. The eigenmodes $\mid \nu >$ are no longer pure wagging or stretching modes. We present in Fig. B.2 the potential felt by the hydrogen around its equilibrium position, together with the ground-state, first excited stretching mode, first excited wagging mode and second excited stretching level densities. The deviation of the potential shape from an ideal ellipsoid is mainly due to the anharmonicity of the stretching mode. In particular, the extra node observed in the plot of $|\psi_{stretch,2}|^2$ originates from the coupling through anharmonicity to higher stretching modes. Because the stretching-wagging coupling is relatively weak, the identification of the lowest eigenstates as (renormalized) wagging or stretching modes is still unambiguous. We present in Fig. B.3(b) (solid line) the theoretical absorption spectrum for transition from the ground state for a s-polarized light, that is, we plot: $\sum_\nu |< \nu = 0 \mid z \mid \nu >|^2 \delta(\omega - \omega_{0,\nu})$ as function of ω, where $\omega_{0,\nu} = E(\nu) - E(\nu = 0)$. The theoretical "spectrum" clearly isolates a transition corresponding to a state at 2740 cm^{-1} above the (ν=0) ground state. This state, with a weight of 84 % on the $\mid n_x = n_y = 0, n_z = 1 >$ basis vector, is clearly identified as the first excited stretching level $|\nu_1 >$ for the coupled system. Because of the anharmonicity, this state has also a 7% weight on the $\mid n_x = n_y = 0, n_z = 2 >$ vector. A 3.4% weight on both $\mid n_x = 2, n_y = 0, n_z = 0 >$ and $\mid n_x = 0, n_y = 2, n_z = 0 >$ expresses the coupling between the stretching and the wagging. Further, we plot (dotted line) $\sum_\nu |< \nu_1 \mid z \mid \nu >|^2 \delta(\omega - \omega_{\nu_1,\nu})$ where $\omega_{\nu_1,\nu} = E(\nu) - E(\nu_1)$. This again isolates a transition corresponding to a state at 2633 cm^{-1} above the (ν_1) energy level with a weight of 46.6 % on the $\mid n_x = n_y = 0, n_z = 2 >$ basis vector and 16.4 % on the $|n_x = n_y = 0, n_z = 3 >$

vector. This state is associated with the second excited stretching level $|\nu_2>$ for the coupled system.

Results for the theoretical and experimental wagging and stretching frequencies are reported in Table B.2, together with an anharmonic shift $-2\Gamma = (E(\nu_2) - E(\nu_1)) - (E(\nu_1) - E(\nu_0))$ of 107 cm^{-1} for the calculated stretching mode. The agreement between theory and experiment seems good. In particular, the position of the absorption peaks in figures B.4(a) and B.3(b) match excellently if we allow a 97 cm^{-1} rigid shift of the theoretical spectrum to larger energy. We note that -2Γ is rather insensitive to the stretching-wagging coupling (we calculate the anharmonic shift of the uncoupled stretching mode to be 107.7 cm^{-1}). This is consistent with the fact that the stretching-wagging coupling is relatively weak in the present system. In the case of H/Si(111)-(1×1), the effect of the coupling with the wagging modes has been calculated [138] to result in nearly doubling the anharmonic shift of the stretching mode.

In terms of the phonon picture, the above $|\ \nu = 1>$ mode corresponds to the one-phonon mode at the Brillouin zone center $\overline{\Gamma}$. We can also calculate the frequency $\omega_1(\overline{M})$ of the one-phonon mode at the zone edge $\overline{M}$ using the frozen-phonon scheme with neighboring atoms moving out of phase. We find $\omega_1(\overline{\Gamma}) - \omega_1(\overline{M}) = 2\ \mathrm{cm}^{-1}$, indicating a rather weak dispersion. The entire one-phonon band $\omega_1(\mathbf{k})$ can then be calculated using the tight-binding model for the surface hexagonal C-H bond lattice, which yields, in the first-nearest-neighbor approximation:

$$\omega_1(\mathbf{k}) = 2\ t\ [\ cos(2\pi k_1) + cos(2\pi k_2) + cos(2\pi(k_1 - k_2))] \tag{B.2}$$

with $\mathbf{k} = (k_1, k_2)$ in reciprocal latttice vector coordinates. This is presented in Fig. Fig. B.5(a) for $\mathbf{k}$ along the high-symmetry directions of the hexagonal Brillouin zone. The very small dispersion and rather large anharmonicity suggests the existence of two-phonon bound state. Moreover, in view of the very narrow phonon dispersion, we may take the anharmonic shift Γ' for a single C-H bond to be the same as that calculated Γ above for the zone center mode, that is $-2\Gamma'=107$ cm^{-1} with an uncertainty much less than 2 cm^{-1}. To study the interaction between the stretching modes of the C-H bonds at the H/C(111)-(1×1) surface, we use the Hubbard-like Hamiltonian proposed in Ref. [138]:

$$H = t \sum_{<i,j>} b_i^+ \, b_j \; + \Gamma' \sum_i b_i^+ \, b_i^+ \, b_i \, b_i \ , \tag{B.3}$$

where b_i and b_i^+ are the harmonic oscillator annihilation and creation operators for a C-H bond on site i (the energy reference is taken to be the ground-state frequency of the C-H modes). The pairs $< i, j >$ index neighboring sites. The one-body operator is the usual hopping term which yields the phonon bands in the harmonic approximation. The two-body term expresses the fact that, because of the anharmonicity, the system gains an energy 2Γ' by localizing two vibrational quanta on the same C-H bond. This model Hamiltonian is valid in the limit of a large Γ'/t ratio [138]. We shall see that this condition is fully satisfied in the present case. To study the extended and localized collective modes of the surface 2D hexagonal lattice of interacting C-H bonds, we go from the harmonic single-bond oscillators basis to the surface extended harmonic phonon basis by building the phonon creation and destruction operators $a_{\mathbf{k}}^+$ and $a_{\mathbf{k}}$:

$$a_{\mathbf{k}} = \frac{1}{\sqrt{N}} \sum_{R_i} e^{i\mathbf{q}\cdot\mathbf{R_i}} \, b_i \tag{B.4}$$

where R_i runs over the N sites of the system and Eq. B.3 becomes then, in the C-H surface phonon basis:

$$H = \sum_{\mathbf{k}} \omega_1(\mathbf{k}) \, a_{\mathbf{k}}^+ \, a_{\mathbf{k}} \; + \frac{\Gamma'}{N} \sum_{\mathbf{Q},\mathbf{k},\mathbf{k'}} a_{\mathbf{k}}^+ \, a_{\mathbf{Q}-\mathbf{k}}^+ \, a_{\mathbf{k'}} \, a_{\mathbf{Q}-\mathbf{k'}} \ , \tag{B.5}$$

where $\omega_1(\mathbf{k})$ is the energy of a phonon with vector $\mathbf{k}$. $\mathbf{Q}$ is the momentum associated with the two-phonon states solution of Eq. B.3. Therefore, the on-site "negative Γ'" term of Eq. B.3 yields an effective attractive phonon-phonon interaction. Within the nearest-neighbor tight-binding model, $\omega_1(\mathbf{k})$ depends on t and $\omega_1(\overline{\Gamma}) - \omega_1(\overline{M}) = 2t$. We therefore find t=0.25 cm^{-1}. We note that the hopping parameter t obtained here is much smaller than the value t_{Si}=0.8 cm^{-1} calculated for the H/Si(111)-(1x1) surface [138]. This can be understood from the much smaller polarizability of the C-H bond which over compensates the fact that the nearest-neighbor distance for the C-H lattice is smaller than the one at the H/Si(111)-(1x1) surface. Our values for t and Γ' yield a ratio Γ'/t which is much larger at the H/C(111) surface than at the H/Si(111) surface. This indicates that a strongly bound two-phonon state should exist in the present system [139].

The inversion of the Hubbard equation is standard [140]. Because **Q** is a good quantum number for the two-phonon states solution of the Hamiltonian B.5, the eigenstates of this Hamiltonian can be written:

$$|\psi(\mathbf{Q} >= \sum_{\mathbf{k}} \chi_k \; a_k^+ a_{Q-k}^+ \; |0> \;\;, \tag{B.6}$$

where $|0>$ is the ground state of the system. It is easy to show then that:

$$\begin{aligned} H\;|\psi(\mathbf{Q} >= &\sum_{\mathbf{k}} \left[\omega_1(\mathbf{k}) + \omega_1(\mathbf{Q}-\mathbf{k})\right] \chi_k \; a_k^+ a_{Q-k}^+|0> \\ &+ \frac{2\Gamma'}{N}\,(\sum_{\mathbf{k'}} \chi_{k'}) \; \sum_{\mathbf{k}} a_k^+ a_{Q-k}^+|0> \end{aligned} \tag{B.7}$$

where boson commutation relations have been used, so that the eigenvalue equation $H|\psi(\mathbf{Q}) >= \omega_2(\mathbf{Q})|\psi(\mathbf{Q}) >$ can then be written:

$$\frac{1}{N} \sum_{\mathbf{k}} \frac{1}{\omega_1(\mathbf{k}) + \omega_1(\mathbf{Q}-\mathbf{k}) - \omega_2(\mathbf{Q})} \;=\; -\frac{1}{2\Gamma} \tag{B.8}$$

This equation, for excitations with wave-vector **Q**, yields (N-1) energies in the quasi-continuum of unbound two single-particle states $\omega_2(\mathbf{Q}) = \omega_1(\mathbf{k}) + \omega_1(\mathbf{Q}-\mathbf{k})$ (shown in Fig B.5(b)) and one solution $\omega_2(\mathbf{Q})$ out of this continuum (shown in Fig B.5(c)). With the calculated values of t and Γ', we find that this latter solution is located

110 cm^{-1} below the one-phonon state energy at $\overline{\Gamma}$. This value is taken to be the two-phonon binding energy E_b for the H/C(111)-(1x1) surface [141]. The agreement with experiment is excellent (see Table B.2). As expected, the present binding energy for H/C is much larger than the one measured [135] and calculated [138] for the H/Si(111)-(1x1) surface. The dispersion of the two-phonon bound state band is calculated to be 0.01 cm^{-1}, which is 14 times smaller than the dispersion calculated for the two-phonon bound state on the H/Si(111) surface. Both the larger binding energy and the absence of dispersion indicates a very localized two-phonon bound state.

Table B.1: Parameters for the potential felt by an hydrogen atom at the C(111)-(1×1) surface.

	H/Diamond		H/Si
	This work	Ref. [136]	Ref. [138]
$\omega_{0z}(meV)$	355.74		250.84
$\omega_{0x}(meV)$	146.40		69.35
a_3 (eV/$\mathring{A}^3$)	-28.34	-28.01	-11.13
b_3 (eV/$\mathring{A}^3$)	5.45		4.00
a_4 (eV/$\mathring{A}^4$)	28.23	27.41	9.94
b_4 (eV/$\mathring{A}^4$)	-12.46		-11.66
c_4 (eV/$\mathring{A}^4$)	0.68		0.78

Table B.2: Experimental and theoretical stretching and wagging frequencies ω_z and ω_x, together with the anharmonic shift -2Γ and the two-phonon bound state energy E_b, are given in cm^{-1} (1 meV = 8.04 cm^{-1}).

	Theory	Experiment
ω_z	2740	2838 ± 2
ω_x	1189	1331 ± 1
-2Γ	107	
E_b	-110	-110 ± 5

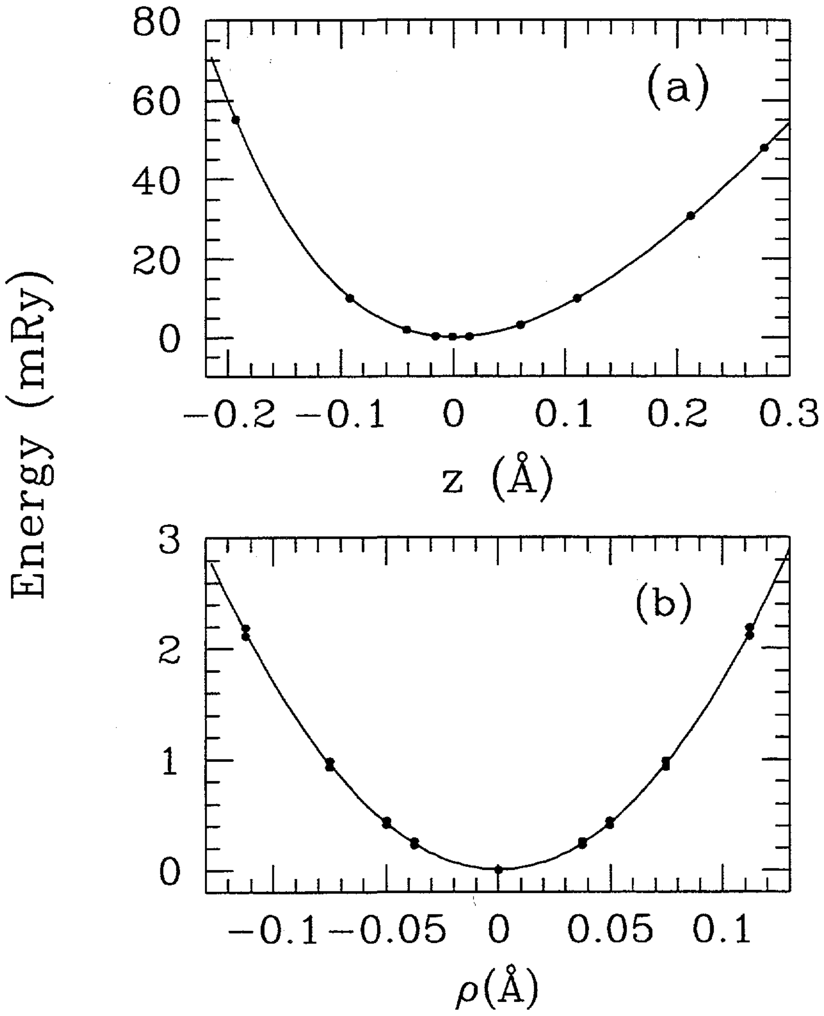

Figure B.1: (a) Calculated potential well for (a) the (x=y=0) hydrogen motion as a function of the displacement z from equilibrium bond length and for (b) the wagging mode (z=0) as a function of the displacement ρ from the equilibrium position. The open squares are the calculated points and the solid lines are a fourth order polynomial least-square fit.

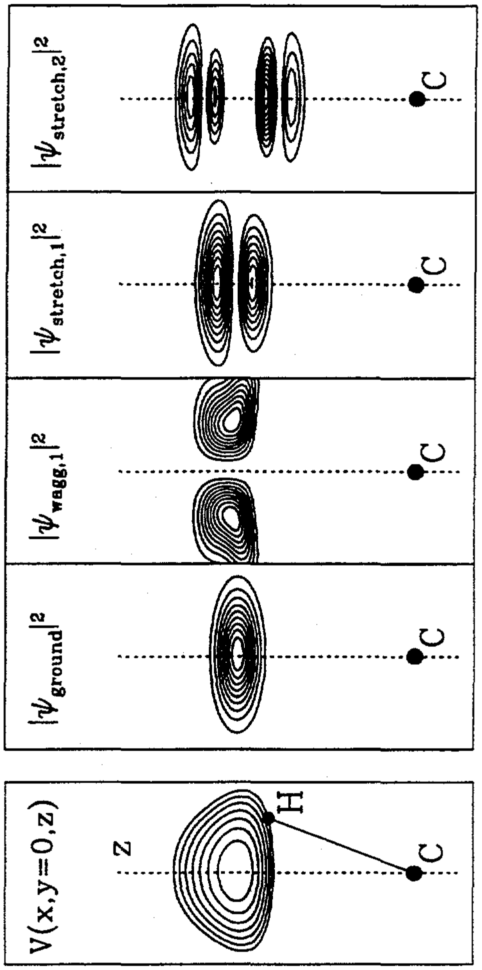

Figure B.2: Presented from left to right: contour plots in the y=0 plane of the potential felt by the hydrogen atom at the surface and of the wavefunction squared of the ground state, first excited wagging mode, first excited stretching mode and second excited stretching mode. For the potential, the contours correspond to energies ranging from $\omega_{0z}/2$ to $7\omega_{0z}/2$ by increment of $\omega_{0z}/2$. For each eigenstate density, we plot 10 density contours with constant increment between the minimum and maximum in-plane density. The position of the carbon atom is indicated as a guide to the eyes. All figures have rotational symmetry around the z axis.

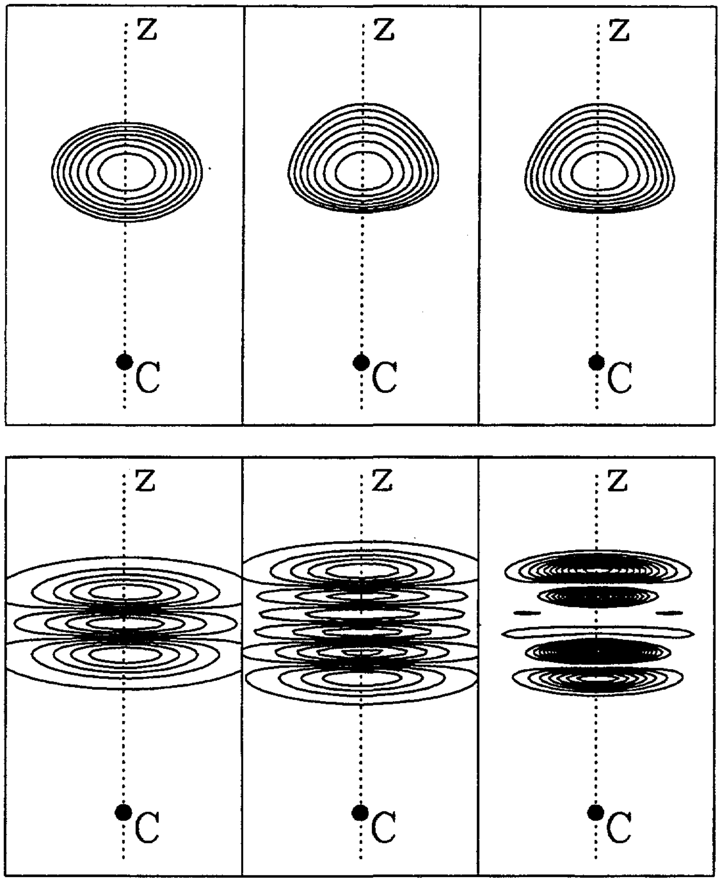

Figure B.3: In the upper panel, contour plots in the y=0 plane of the potential felt by the hydrogen atom in the harmonic case (left), when the stretching anharmonicity is included (center) and finally when both anharmonicity and coupling to the wagging are included (right). The contours correspond to energies ranging from $\omega_{0z}/2$ to $7\omega_{0z}/2$ by increment of $\omega_{0z}/2$. In the lower panel, the second-excited stretching mode wavefunction $|\psi_{stretch,2}|^2$ corresponding to the potential plotted right above are presented in the y=0 plane.

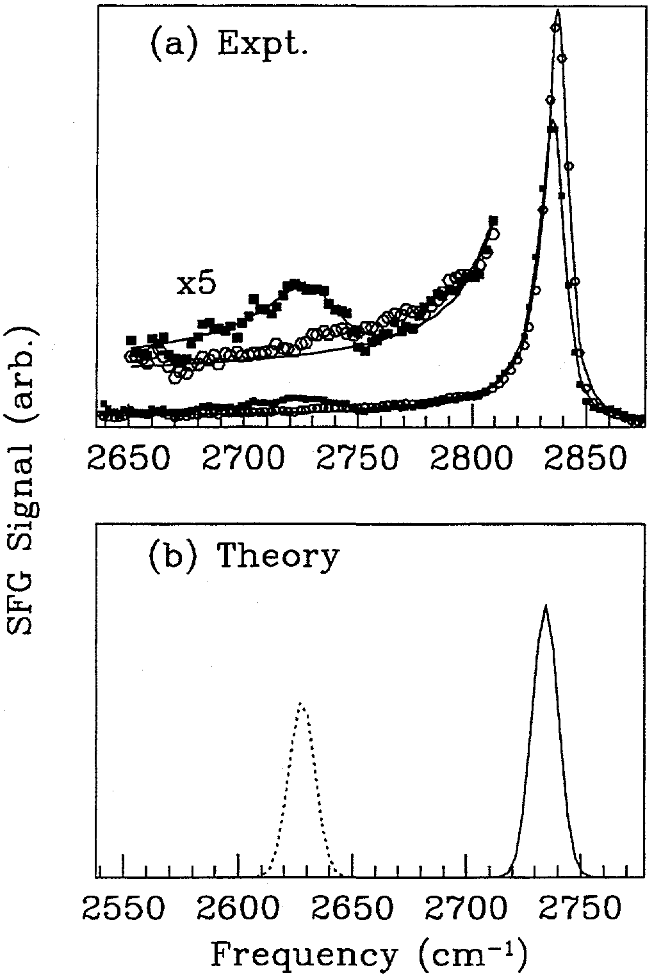

Figure B.4: a) Infrared SFG probe spectrum on the H/C(111)-(1×1) surface showing the fundamental $\nu_{0\rightarrow1}$ vibrational transition (open circles) and the $\nu_{1\rightarrow2}$ vibrational transition (solid squares). The inset is expanded five times. Solid lines are fit to the experimental data points. b) Theoretical absorption spectrum for the stretching modes of the C-H bond with incoming s-polarized light. The solid line corresponds to the $\nu_{0\rightarrow1}$ transition and the dashed line to the $\nu_{1\rightarrow2}$ transition. A 1 meV gaussian broadening for the energy levels has been used and the relative peak height between the two transitions is arbitrary. Frequencies are in cm^{-1}.

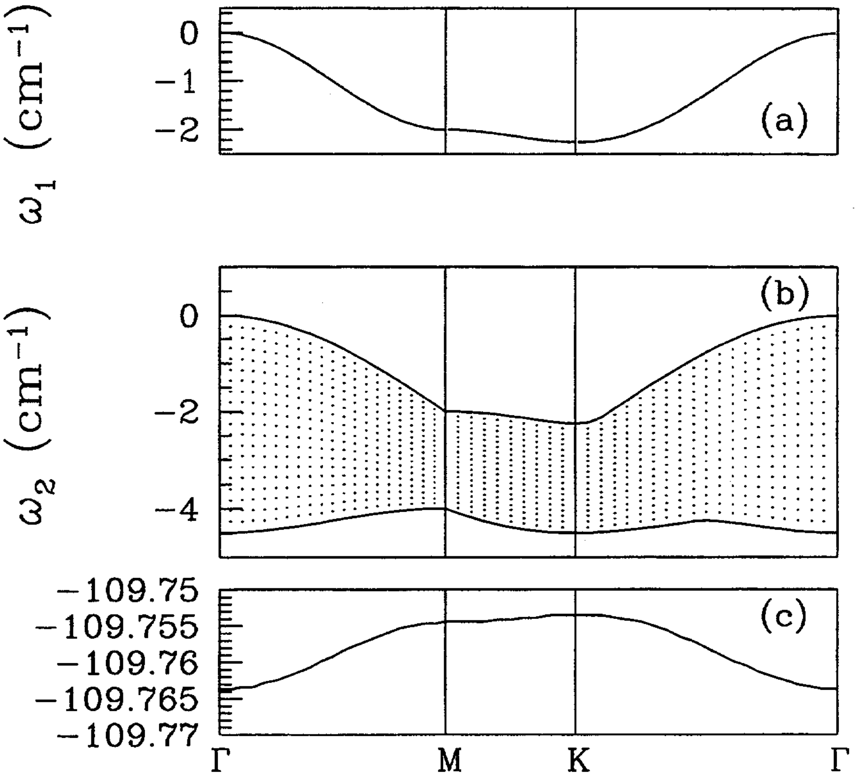

Figure B.5: Dispersion along high-symmetry directions for (a) the one-phonon states, (b) the unbound two-phonon continuum and (c) the two-phonon bound states. Energies are in cm^{-1}. Note that the energy scale of (c) is 150 smaller that the energy scale for (a) and (b). However, (a), (b) and (c) share the same energy reference.

Bibliography

[1] P. Hohenberg and W. Kohn, Phys. Rev **136**, B864 (1964); W. Kohn and L. J. Sham, Phys. Rev. **140**, A1133 (1965).

[2] M. S. Hybertsen and S. G. Louie, Phys. Rev. Lett. **55**, 1418 (1985); Phys. Rev. B, **34**, 5390 (1986). See also: R. W. Godby, M. Schlüter and L. J. Sham, Phys. Rev. Lett. **56**, 2415 (1986); Phys. Rev. B **37**, 10159 (1988).

[3] L. Hedin and S. Lunqvist, in *Solid State Physics: Advances in Research and Applications*, edited by F. Seitz, D. Turnbull and H. Ehrenreich (Academic, New York, 1969),Vol. 23; L. Hedin, Phys. Rev. **139**, A796 (1965).

[4] L. Kleinman and D. M. Bylander, Phys. Rev. Lett. **48**, 1425 (1982).

[5] K. Laasonen, R. Car, C. Lee and D. Vanderbilt, Phys. Rev. B **43**, 6796 (1991) and references therein.

[6] R. Natarajan and D. Vanderbilt, J. of Comp. Phys. **82**, 218 (1989).

[7] Pour une revue, voir: M. C. Payne, M.P. Teter and D. C. Allan, T. A. Arias and J. D. Joannopoulos, Rev. Mod. Phys. **61**, 689; G. Galli and A. Pasquarello, *New perspectives on Computer Simulations in Chemical Physics* (Kluwer, Dordrecht, in press).

[8] W. Yang, Phys. Rev. Lett. **66**, 1438 (1991).

[9] X.-P. Li, W. Nunes and D. Vanderbilt (unpublished).

[10] G. Galli and M. Parinello, Phys. Rev. Lett **69**, 3547 (1992); F. Mauri, G. Galli and R. Car, Phys. Reb B **47**, 9973 (1993).

[11] P. Ordejon, D. A. Drabold, M. P. Grumbach and R. M. Martin, Phys. Rev. B **48**, 14646 (1993).

[12] A. Y. Liu and M. L. Cohen, *Science* **245**, 841 (1989); M. L. Cohen, *Science* **261**, 301 (1993); M. L. Cohen, Solid State Commun. **92**, 45 (1994).

[13] X. Blase, L. X. Benedict, E. L. Shirley and S. G. Louie, Phys. Rev. Lett. **72**, 1878 (1994).

[14] X. Blase, A. Rubio, S. G. Louie and M. L. Cohen, Europhys. Lett. **5**, 335 (1994).

[15] D. Pines, *The Many-Body Problem: A Lecture Note and reprint Volume*, The Benjamin/Cummings Publishing Company, 1962 (provides in particular an english translation of J. P. Landau's pionnering JETP articles); P. Nozières, *Theory of Interacting Fermi Systems*, Benjamin, New York and Amsterdam (1964); D. Pines, *Elementary excitations in solids: lectures on phonons, electrons, and plasmons*, New York, W. A. Benjamin (1964).

[16] R. W. Godby, M. Schlüter and L. J. Sham, Phys. Rev. Lett. **56**, 2415 (1986); Phys. Rev. B **36**, 6497 (1987); **37**, 10159 (1988).

[17] X. Zhu and S. G. Louie, Phys, Rev. B **43**, 14142 (1991).

[18] M. S. Hybertsen and S. G. Louie, Phys. Rev. B **38**, 4033 (1988).

[19] R. S. Becker, B. S. Swartzentruber, J. S.Vickers, M. S. Hybertsen and S. G. Louie, Phys. Rev. Lett. **60**, 116 (1988).

[20] J. E. Northrup, M. S. Hybertsen and S. G. Louie, Phys. Rev. Lett. **66**, 500 (1991).

[21] X. Zhu and S. G. Louie, Phys, Rev. B **43**, 12146 (1991).

[22] S. B. Zhang, D. Tománek, S. G. Louie, M. L. Cohen, and M. S. Hybertsen, Solid State Commun. **66**, 585 (1988).

[23] M. S. Hybertsen and M. Schlüter, Phys. Rev. B **36**, 9683 (1987); S. B. Zhang, M. S. Hybertsen, M. L. Cohen, S. G. Louie and D. Tómanek, Phys. Rev. Lett. **63**, 1495 (1989).

[24] E. Shirley and S. G. Louie, Phys. Rev. Lett. **71**, 133 (1993).

[25] X. Blase, X. Zhu and S. G. Louie, Phys. Rev. B **49**, 4973 (1994).

[26] X. Blase, A. Rubio, S.G. Louie and M. L. Cohen, to appear in Phys. Rev. B.

[27] X. Blase, A. J. R. da Silva, X. Zhu and S. G. Louie, Phys. Rev. B. **50**, 8102 (1994).

[28] R. P. Chin, X. Blase, Y. R. Shen and S. G. Louie, submitted to Phys. Rev. Lett.

[29] S. Iijima, *Nature* **354**, 56 (1991).

[30] S. Iijima and T. Ichihashi, *Nature* **363**, 603 (1993).

[31] D.S. Bethune *et al*, *Nature* **363**, 605 (1993).

[32] P. M. Ajayan and S. Iijima, *Nature* **361**, 333 (1993); P. M. Ajayan *et al*, *Nature* **362**, 522 (1993).

[33] E. J. M. Hamilton, S. E. Dolan, C. M. Mann, H. O. Colijn, C. A. McDonald and S. G. Shore, Science **260**, 659 (1993).

[34] Synthesis of $B_xC_yN_z$ nanotubes have been recently reported. In these structures, electron energy loss spectroscopy measurements show that the nitrogen K-edge differs significantly from the usual sp^2 hybridization shape. See: K. Cherrey *et al*, submitted for publication.

[35] Y. Miyamoto, A. Rubio, M. L. Cohen and S. G. Louie, to be published in Phys. Rev. B.

[36] Y. Miyamoto, A. Rubio, M. L. Cohen and S. G. Louie, Phys. Rev. B. **50**, 4976 (1994).

[37] N. Hamada, S. Sawada and A. Oshiyama, Phys. Rev. Lett. **68**, 1579 (1992).

[38] R. Saito, M. Fujita, G. Dresselhaus, M. S. Dresselhaus, Appl. Phys. Lett. **60**, 2204 (1992).

[39] J. W. Mintmire, B. I. Dunlap and C. T. White, Phys. Rev. Lett. **68**, 631 (1992).

[40] J. C. Slater and G. F. Koster, Phys. Rev. **94**, 1498 (1954).

[41] N. Troullier and J. L. Martins, Solid State Commun. **74**, 613 (1990).

[42] N. Troullier and J. L. Martins, Phys. Rev B **46**, 1754 (1992).

[43] D. Tománek and S. G. Louie, Phys. Rev. B **37**, 8327 (1988).

[44] C. H. Xu, C. Z. Wang, C. T. Chan, and K. M. Ho, J. Phys: Condens. Matter **4**, 6047 (1992).

[45] A. A. Lucas, P. H. Lambin, and R. E. Smalley, J. Phys. Chem. Solids **54**, 587 (1993).

[46] S. Sawada and N. Hamada, Solid State Commun. **83**, 917 (1992).

[47] A. Rubio, J. L. Corkill and M. L. Cohen, Phys. Rev. B **49**, 5081 (1994).

[48] D. J. Chadi, private communication.

[49] F. Jensen and H. Toflund, Chem. Phys. Lett. **201** 89 (1993)

[50] N. A. W. Holzwarth, S. G. Louie and S. Rabii, Phys. Rev. B **26**, 5382 (1982).

[51] A. Zunger, A. Katzir, and A. Halperin, Phys. Rev. B **13**, 5560 (1974).

[52] We note that of all the tubes studied containing C, B and N in various proportions, BN nanotubes are the only one to exhibit such a constant gap. This should facilitate greatly the experimental characterization of pure BN nanotubes.

[53] A. Y. Liu, R. M. Wentzcovitch and M. L. Cohen, Phys. Rev. B **39**, 1760 (1989).

[54] P. M. Ajayan and S. Iijima, *Nature* **361**, 333 (1993); P. M. Ajayan *et al*, *Nature* **362**, 522 (1994).

[55] M. R. Pederson and J. Q. Broughton, Phys. Rev. Lett. **69**, 2689 (1992).

[56] Y. Yosida, Appl. Phys. Lett. **64**, 3048 (1994).

[57] E. Dujardin, T. W. Ebbessen, H. Hiura and K. Tanigaki, *Science* **265**, 1850 (1994).

[58] S. Aronson, F. J. Salzano and D. Bellafiore, J. of Chem. Phys. **49**, 434 (1968).

[59] Values for the binding energy of K and Pb are taken from: C. Kittel, in *Introduction to solid state physics*, edited by John Wiley & Sons, Inc, New York/London/Sydney/Toronto, 5th edition (1971).

[60] R. Seshadri, H. N. Aiyer, A. Govindaraj and C. N. R. Rao, Solid State Commun. **91**, 195 (1994).

[61] Yoshi Miyamoto, private communication.

[62] A. P. Ramirez, R. C. Haddon, O. Zhou, R. M. Fleming and D. W. Murphy, to be published.

[63] G. S. Higashi et al., Appl. Phys. Lett. **56**, 656 (1990); and Appl. Phys. Lett. **58**, 1656 (1991).

[64] P. Guyot-Sionnest, P. Dumas, Y. J. Chabal and G. S. Higashi, Phys. Rev. Lett. **64**, 2156 (1990); P. Dumas, Y, J. Chabal and G. S. Higashi, Phys. Rev. Lett. **65**, 1124 (1990); P. Guyot-Sionnest, Phys. Rev. Lett. **66**, 1489 (1991).

[65] S. Bouzidi *et al*, Phys. Rev. B **45**, 1187 (1992).

[66] P. Jakob *et al*, Appl. Phys. Lett. **59**, 2968 (1991); and Chem. Phys. Lett. **187**, 325 (1991).

[67] K. Hricovini *et al*, Phys. Rev. Lett. **70**, 1992 (1993).

[68] Laboratoire pout l'Utilisation du Rayonnement Electromagnetique, Centre Universitaire Paris-Sud-Bat.209D-F91405 Orsay Cedex (France).

[69] C. J. Karlsson et al., Phys. Rev. B **41**, 1521 (1990).

[70] E. Landemark, C. J. Karlsson, and R. I. G. Uhrberg, Phys. Rev. B **44**, 1950 (1991).

[71] M. B. Nardelli *et al*, Surf. Sci. **269/270**, 879 (1992).

[72] J. A. Appelbaum and D. R. Hamann, Phys. Rev. Lett. **34**, 806 (1975).

[73] K. C. Pandey, T. Sakurai, and H. D. Hagstrum, Phys. Rev. Lett. **35**, 1728 (1975).

[74] K. M. Ho, M. L. Cohen and M. Schlüter, Phys. Rev. B **15**, 3888 (1977).

[75] D. R. Hamann, M. Schlüter and C. Chiang, Phys. Rev. Lett. **43**, 1494 (1979).

[76] G. P. Kerker, J. Phys. C **13**, L189 (1980); K. M. Ho, C. Elsässer, C. T. Chan, M. Fähnle, J. Phys.: Condens. Matter **4**, 5189 (1992).

[77] D. M. Ceperley and B. J. Alder, Phys. Rev. Lett. **45**, 566 (1980).

[78] H. J. Monkhast and J. D. Pack, Phys. Rev. B **13**, 5188 (1976).

[79] M. S. Hybertsen and S. G. Louie, Phys. Rev B **35**, 5585 (1987); Phys. Rev B **35**, 5602 (1987).

[80] S. L. Adler, Phys. Rev **126**, 413 (1962).

[81] N. Wiser, Phys. Rev. **129**, 62 (1963).

[82] X. P. Li and D. Vanderbilt, Phys. Rev. Lett. **69**, 2543 (1992).

[83] X. Zhu and S. G. Louie, Phys. Rev. B **45**, 3940 (1992).

[84] This is illustrated in S. G. Louie, *Electronic Structure, Dynamic and Quantum Structural Properties of Condensed Matter*, edited by J. Devreese and P. van Camp (Plenum, New York, 1985), p.335.

[85] R. O. Jones and O. Gunnarsson, Rev. Mod. Phys. **61**, 689 (1989); and references therein.

[86] C. Kittel, *Introduction to Solid State Physics, Sixth Edition* (John Wiley & Sons Inc., New York), Table 5, p. 59.

[87] S. Bashkin and J. O. Stoner, *Atomic Energy levels and Grotian Diagrams*, Vol.1, (North Holland, New York, 1975). We estimate the experimental Si 3s eigenvalue by adding the experimental first ionization energy to the promotion energy $s^2p(^2P) \rightarrow sp^2(^4P)$. We neglect therefore relaxation effets which are for these levels not larger than some few tenths of eV.

[88] Y. Miyamoto and A. Oshiyama, Phys. Rev. B **44**, 5931 (1991).

[89] E. Pehlke and M. Scheffler, Phys. Rev. Lett. **71**, 2338 (1993).

[90] L. Pedocchi, N. Russo and D. R. Salahub, Phys. Rev. B **47**, 12992 (1993) and references therein.

[91] A. Taleb-Ibrahimi, R. Gunther, P. Dumas, Y. J. Chabal, G. Indlekhofer and Y. Petroff, to be published.

[92] The synchrotron beam hits the surface either at normal incidence or glazing incidence, depending of the orientation of the sample. The analyser is fixed and positioned at 45 degrees of the direction of the incoming photons. By rotating the sample from the normal to the grazing angles relative to the incident photons, s-polarization can be obtained for both bulk and surface sensitive spectra.

[93] The kinetic energy of the detected photoelectrons was around 30 eV. This very large kinetic energy in general means that the final state is well described by a planewave. We note that level intensities are usually measured within 10% accuracy.

[94] This kind of polarization effect has been seen experimentally by subtracting two spectra taken respectively with a polarisation parallel and perpendicular to the surface plane [91].

[95] K. Kobayashi, T. Sano and Y. J. I'Haya, Chem. Phys. Lett. **219**, 53 (1994).

[96] C. A. Brookes, R. M. Hooper and W. A. Lambert, Philos. Mag. A **47**, L9 (1983).

[97] BN can be found in the zinc-blende, wurtzite or hexagonal structure. The hexagonal (graphite-like) structure is the most common form of BN. Cubic

BN has been studied within the same quasiparticle approach. See: M. P. Surh, S. G. Louie and M. L. Cohen, Phys. Rev. B **43**, 9126 (1991).

[98] R. M. Wentzcovitch, K. J. Chang and M. L. Cohen, Phys. Rev. B **34**, 1071 (1986). In this study, the LDA minimum band gap was found to be 4.2 eV.

[99] Angel Rubio, J. L. Corkill, Marvin L. Cohen, Eric L. Shirley and Steven G. Louie, Phys. Rev. B **48**, 11810 (1993).

[100] The LUMO state at Γ is located 1.14 eV below the vacuum level.

[101] An equivalent state has been shown to exhist in the graphene sheet using the same supercell method. See: Y. Miyamoto, private communication.

[102] In the case of bulk hexagonal BC_3, the gap closes only because of the band-structure dispersion along the c-axis.

[103] We note that the STO-nG basis consists of expansions of Slater-type atomic orbitals in terms of n gaussian functions. Therefore both basis are equivalent and, in particular, have the same spatial extent. For a review, see: W. J. Wehre, L. Radom, P. v. R. Schleyer and J. A. Pople, *Ab Initio Molecular Orbital Theory*, (John Wiley & Sons, Inc.: New York, 1986).

[104] A. M. Rappe, J. D. Joannopoulos and P. A. Bash, Jo. Am. Phys. Soc. **114**, 6466 (1992).

[105] A method to circumvent these problems, and keep working in the framework of a planewave formalism, has been adressed in: F. Gygy, Phys. Rev. B **48**, 11692 (1993).

[106] In other words, we use a real-space "delta-function" basis sets. By construction, such basis are orthonormal, do not depend explicitely on the

ionic positions and share with plane-wave basis (via Fourier transform) the same convergency properties.

[107] F. Aryasetiawan and O. Gunnarsson, Phys. Rev. B **49**, 16214 (1994).

[108] F. Aryasetiawan, Phys. Rev. B **46**, 13051 (1992).

[109] This method is currently under study and will be refered to in this chapter as a "direct" real-space method. See: H. N. Rojas, R. W. Godby and R. J. Needs, private communication.

[110] Such an Hamiltonian is often chosen to be the DFT-LDA Kohn-Sham Hamiltonian.

[111] In metals, such a decay scales as $\cos(k_F\mathrm{r})/\mathrm{r}^3$ and is therefore much slower than the exponential decay in semiconductors.

[112] B. R. A. Nijboer and F. W. de Wette, Physica **23**, 309 (1957); D. Ceperley, Phys. Rev. B **18**, 3126 (1978).

[113] R. M. Pick, M. H. Cohen and R. M. Martin, Phys. Rev. B **1**, 910 (1970).

[114] A. Zangwill and P. Soven, Phys. Rev. A **21**, 1561 (1980).

[115] W. Eckart, Phys. Rev. Lett. **52**, 1925 (1984).

[116] A. Rubio and L. Serra, Phys. rev. B **48**, 18222 (1993).

[117] A. A. Quong and A. G. Eguiluz, Phys. Rev. Lett. **70**, 3955 (1993). In this work, the plasmon widths were around 5 eV (depending on the wave-vector $\mathbf{q}$) and $\Delta = 0.075$ Ry was chosen. Since plasmon energies were located at 15-20 eV, the calculation of $\chi^0(\mathbf{q}|\omega)$, from the static regime to above the plasmon energies, was certainly repeated 15 to 20 times.

[118] S. Saito, S. B. Zhang, S. G. Louie and M. L. Cohen, Phys. Rev. B **40**, 3643 (1989).

[119] R. Daling, W. van Haeringen and B. Farid, Phys. Rev B **44**, 2952 (1991); B. Farid, G. E. Engel, R. daling and W. van Haeringen, Phys. Rev B **44**, 13349 (1994).

[120] D. P. Joubert, J. Phys: Condens. Matter **5**, 2033 (1993).

[121] S. Baroni, P. Giannozzi and A. Testa, Phys. Rev. B **58**, 1861 (1987).

[122] S. Grabowski, M. E. Garcia and K. H. Bennemann, Phys. Rev. Lett. **72**, 3969 (1994).

[123] C. Brechignac *et al*, Phys. Rev. Lett. **67**, 1222 (1994).

[124] M. F. Lin and K. W.-K. Shung, Phys. Rev. B **47**, 6617 (1993).

[125] A. Rubio, L.C. Balbás y J.A. Alonso, Physical Review B **46** 4891-4898 (1992).

[126] G. F. Neumark, R. M. Park and J. M. DePuydt, Physics Today June 1994 and references therein; A. V. Nurmikko and R. L. Gunshor, Solid State Commun. **92**, 113 (1994).

[127] S.-H. Wei and A. Zunger, Phys. Rev. B **37**, 8958 (1988).

[128] J. L. Martins and N. Troullier, Phys. Rev. B **43**, 2213 (1991).

[129] Z. H. Levine and S. G. Louie, Phys. Rev. B **25**, 6310 (1982); M. S. Hybertsen and S. G. Louie, Phys. Rev. B **37**, 2733 (1994).

[130] The difference between the HF and LDA electronic operator is further "pseudize" and made shorter range to reduce its extent beyond the spatial range of the 3d orbitals (the difference between the HF and LDA electronic potential behaves as 1/r at large distance). We note however that such a scheme, as in standard modern *ab initio* pseudopotential generation scheme, is a parameter free procedure.

[131] O. Shakarov, A. Rubio, X. Blase, M. L. Cohen and S. G. Louie, Phys. Rev. B **50**, 10780 (1994).

[132] R. S. Krishnan, Proc. Indian Acad. Sci. **24**, 25 (1946).

[133] M. H. Cohen and J. Ruvalds, Phys. Rev. Lett. **23**, 1378 (1969).

[134] D. Vanderbilt, S. G. Louie and M. L. Cohen, Phys. Rev. Lett. **53**, 1477 (1984).

[135] P. Guyot-Sionnest, Phys. Rev. Lett. **67**, 2323 (1991).

[136] Xuejun Zhu and Steven G. Louie, Phys. Rev. B **45**, 3940 (1992).

[137] X. Blase, Xuejun Zhu and Steven G. Louie, Phys. Rev. B **49**, 4973 (1994).

[138] X.-P. Li and David Vanderbilt, Phys. Rev Lett. **69**, 2543 (1992).

[139] J. C. Kimball, C. Y. Fong and Y. R. Shen, Phys. Rev. B **23**, 4946 (1981).

[140] L. N. Cooper, Phys. Rev. **104**, 1189 (1956).

[141] The probe is in the infrared so that we calculate the binding energy E_b at $\overline{\Gamma}$ in order to compare with the experimental result. We note also that the question of the origin of the energies chosen to refer E_b is, in the present case, irrelevant due to the very small value of t.